MONITORING AND CONTROL FOR LASER POWDER BED FUSION ADDITIVE MANUFACTURING

Monitoring and Control for Laser Powder Bed Fusion Additive Manufacturing

By

HOSSEIN REZAEIFAR, BSc., MSc.

A Thesis

Submitted to the School of Graduate Studies in Partial Fulfillment of the Requirements

for the Degree Doctor of Philosophy

McMaster University

DOCTOR OF PHILOSOPHY (2021) McMaster University

(Mechanical Engineering) Hamilton, Ontario

TITLE: Monitoring and Control for Laser Powder Bed Fusion Additive Manufacturing

AUTHOR: Hossein Rezaeifar

B.Sc. in Mechanical Engineering (Babol Noshirvani University of Technology, Babol, Iran)

M.Sc. in Mechanical Engineering (University of Tehran, Tehran, Iran)

SUPERVISORS: Dr. M. A. Elbestawi

NUMBER OF PAGES: xix, 161

Abstract

Laser powder bed fusion (L-PBF) refers to an additive manufacturing (AM) process in which a high-intensity laser source melts powders in a layer-by-layer manner to fabricate parts based on a computer-aided design (CAD) model without almost any geometrical limitations. The development of the L-PBF process has provided an outstanding opportunity to manufacture unique parts which are practically impossible to be produced by conventional manufacturing methods. The L-PBF process also does not require intricate build tools and assembly processes. However, quality issues such as non-uniform microstructure or mechanical properties, porosities, and surface roughness deteriorate the quality of the parts fabricated by the L-PBF process. Therefore, the reliability and the repeatability of the process are required to be addressed.

This study deals with improving the quality of the part fabricated by the L-PBF process and making the process more reliable and repeatable. The control approach was employed to elevate the quality of the final part from three different aspects. First, making the microstructure and microhardness of the part uniform through a control approach was investigated. Three controllers, namely, proportional (P), adaptive P, and quasi sliding mode, were developed to control the melt pool temperature for the Inconel 625 superalloy. An analytical-experimental model was presented to evaluate the performance of controllers via simulation. A monitoring system consisting of a two-color pyrometer was utilized off-axially to monitor the melt pool temperature for use by the controllers as a feedback signal. The results indicated that the control approach led to microhardness and microstructure

uniformity, resulting from the reduced variation in the primary dendrite arm spacing compared to the case with constant process parameters. Second, the control approach was utilized to produce optimum parts instead of using the energy density criterion. Temperature domains corresponding to the most common porosities, namely, lack of fusion (LOF), lack of penetration (LOP), and keyhole, were determined in a range of process parameters using a thermal imaging system. A safe zone was introduced by defining a lower and an upper limit based on the critical temperatures causing transitions from LOP to defect-free and from defect-free to keyhole zones, respectively. A proportional-integral-derivative (PID) controller was used to maintain the melt pool temperature within the safe zone during the L-PBF process for Inconel 625 and avoid the formation of porosities, regardless of the initial condition selected and the scanning speed employed. In all cases, a short settling time in the order of the printing time for a few layers was required to reach the steady-state condition at which defect-free parts could be obtained. Finally, minimizing the top surface roughness of the parts manufactured by the L-PBF process by deploying a Feedforward plus Feedback control system was targeted in this study. The most common factors affecting the surface quality, namely, balling, lack of inter-track overlap, overlapping curvature of laser scan tracks, and spatters, were investigated through a monitoring system consisting of a high-speed camera, a zooming lens, and a short pass filter. The desired melt pool width and the critical value for the level of spatters were determined using the imaging system and subsequent image processing. An experimental model was developed, and the control system was designed accordingly. Both simulations and experimental results showed excellent transient performance of the control system to reach the desired melt pool width only after printing a few layers. Also, the control system was evaluated at different scanning speeds and with different

geometries. The results obtained from this study indicated that controlling the geometry of the melt pool can mitigate significant defects occurring during the process and minimize the top surface roughness.

Preface

This Ph.D. thesis is an integrated article thesis, also known as a sandwich thesis, which has been composed of five main chapters, all focusing on the monitoring and control for laser powder bed fusion additive manufacturing. The chapters represent papers that are either published or under consideration for publication in authentic international journals. The followings list them in the order of the year:

Chapter 1 introduces the background and motivation of the research as well as the thesis objectives. It shows the new path in laser powder bed fusion and explains how this thesis contributes to making the process more reliable and repeatable.

Chapter 2: is focused on the microstructure control of Inconel 625 during the laser powder bed fusion process. This chapter is an extended version of a published research paper: Hossein Rezaeifar and M. A. Elbestawi. "On-line melt pool temperature control in L-PBF additive manufacturing." The International Journal of Advanced Manufacturing Technology 112, no. 9 (2021): 2789-2804.

Chapter 3: deals with quality control of the laser powder bed fusion (L-PBF) process using a temperature measurement approach rather than the commonly used energy density criterion. A version of this chapter was published as a research paper: Hossein Rezaeifar and Mohamed Elbestawi. "Porosity formation mitigation in laser powder bed fusion process using a control approach." Optics & Laser Technology 147 (2022): 107611.

Chapter 4: discusses minimizing the top surface roughness of the part manufactured by the laser powder bed fusion (L-PBF) process by deploying a Feedforward plus Feedback control system. A version of this chapter is submitted to the journal of manufacturing processes: Hossein Rezaeifar and Mohamed Elbestawi. " Minimizing the surface roughness in L-PBF additive manufacturing process using a combined feedforward plus feedback control system."

Chapter 5 summarizes the main conclusions and contribution of the thesis, highlights the strength and limitations, and presents some suggestions for future work. Finally, it defines the contribution of this thesis to the literature.

To my parents,

I owe you everything.

Acknowledgments

First and foremost, I would like to express my very great appreciation to my supervisor Dr. Mohamed Elbestawi for his knowledge, patience, guidance, and encouragement along the way in this four-year journey. None of the work would have been possible without his support.

My sincere thanks must also go to the members of my supervisory committee, Dr. Saeid Habibi and Dr. Eugene Ng, for their valuable and constructive feedback, interesting discussions, and insightful comments. There is no way to express how much it meant to me to have been a member of the AMG group at McMaster University. I want to thank my colleagues for the discussions, presentation rehearsals, and fruitful group meetings. Special thanks to Ali Ghasemi, Dr. Eskandar Fereidouni, and Dr. Morteza Narvan for sharing their knowledge and always being there if I needed help. I also would like specially thank Dr. Nazli Alizadeh Tabrizi who kept me motivated and assisted me during these four years.

I deeply thank my parents and my sister Dr. Fatemeh Rezaeifar for their unconditional trust, support, timely encouragement, and endless patience. I am forever indebted to my parents for giving me the opportunities and experiences to make me who I am. They selflessly encouraged me to explore new directions in life and seek my destiny. This journey would not have been possible if not for them, and I dedicate this milestone to them.

Contents

List of Figures

List of Tables

Introduction

1.1 Background

During the past few decades, there has been a significant effort in controlling the quality of the final products in different manufacturing processes. The reason behind controlling the quality is making the processes more reliable and repeatable. Therefore, controlling the quality of the parts fabricated by a manufacturing process is a potential candidate for research in the manufacturing area.

Additive manufacturing (AM) is a fabrication process that shapes and consolidates the powder feedstock to arbitrary configurations in a layer-wise fashion by taking the information from a CAD file. It is currently one of the rapidly growing advanced manufacturing techniques in the world [1,2]. Additive manufacturing technology, which involves a comprehensive integration of materials science, mechanical engineering, and laser technology, is an important revolution in the manufacturing industry [3].

Several AM techniques are currently commercially available for processing different materials, including metals, ceramics, and polymers. The laser powder bed fusion (L-PBF) process is a well-established additive manufacturing (AM) technology in which metal powders are fused layer-by-layer to fabricate near-net-shape parts in two main stages. First, the powder is uniformly deposited on a substrate. Then, a high-power laser selectively melts powder particles based on a computer-aided design (CAD) model. This process continues until the final component is built (Figure 1-1) [4–9]. The advantages of this system include its ability to produce high-resolution features and internal features. The

emergence of L-PBF as a novel processing method has opened a new window to fabricate parts with unique microstructural and mechanical properties different from those produced by conventional manufacturing methods. Although AM has several advantages over the conventional manufacturing processes, the process conditions in this technology have an important influence on the quality of the products, so the physics of the process is required to be investigated precisely.

Several factors can affect the quality of the part fabricated by the L-PBF process. Based on [10–12], the microstructure of the parts correlates with their mechanical properties. Consequently, using a fixed set of process parameters may lead to components with non-uniform microstructure and consequently varying mechanical properties. Therefore, keeping the microstructure of the fabricated parts or manipulating it during the L-PBF process helps to achieve the desired mechanical properties of the products.

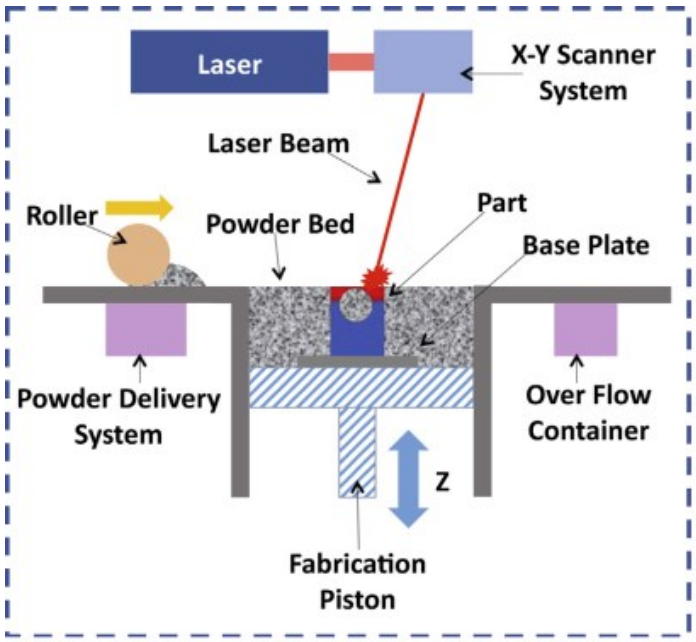

Figure 1-1 Schematic of the L-PBF process.

Although the microstructure control has been investigated in some types of additive manufacturing, especially the direct energy deposition (DED) process [13], no attempts have been made to control the microstructure of the part during the L-PBF process. Microstructural properties depend on the solidification process. The solidification structure has two main characteristics: (1) Solidification mode or morphology and (2) the size of solidification structure. Solidification modes are divided into four groups: (1) planar, (2) cellular, (3) columnar dendritic, and (4) equiaxed dendritic. The formation of each solidification mode and the size of the solidification structure are determined by the thermal dynamics of the process[14] (Figure 1-2). Therefore, manipulation of microstructure is possible by controlling the thermal dynamics of the melt pool.

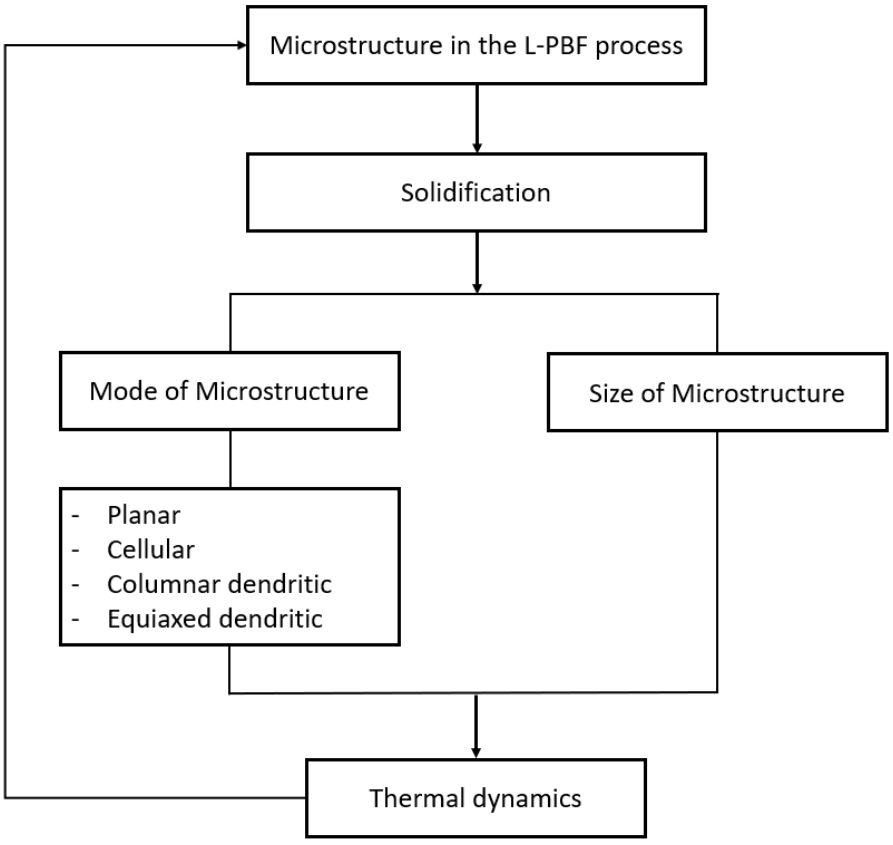

Figure 1-2. Formation of SLM microstructure and its relation with thermal dynamics.

Apart from the microstructure of the final part, the quality of the final product can be deteriorated by a prevalent defect, which is called porosity. Porosity is defined by the voids that are located inside the bulk of the printed part. Porosities can be divided into four different groups [15,16], namely the lack of fusion (LOF) [4,17–19], lack of penetration (LOP), gas porosities [4,19], and keyhole porosities [4,20–22]. In the lack of fusion situation, the voids have irregular shapes and contain unmelted/partially (UM/PM) melted powders. This kind of porosity occurs at low temperatures of the melt pool (Figure 1-3(a)). The LOP is defined as inadequate penetration of the melt pool of a currently depositing track into the previously consolidated layer or the adjacent track. The porosities formed by this mechanism have been presented in Figure 1-3(b), in which two adjacent tracks were not completely bonded together. This type of porosity originates from the rapid solidification rate and high viscosity of the molten material at a lower temperature [23–25]. Powder particles may have some internal holes filled by gas due to the powder production process. The gas can be released and trapped inside the part during the L-PBF process, leading to the formation of tiny spherical porosities (Figure 1-3(c)), called gas porosities. The entrapment of shielding gas and vaporized elements of the alloy can also produce gas porosity [20,26,27]. Figure 1-3(d) illustrates the schematic of the keyhole mode and compares it with the mode that the energy density is not high (conduction mode). In the keyhole mode, gas can be trapped into the layers during the solidification process.

There are some studies for predicting the lack of fusion porosities [15,28,29]. For instance, Lough et al. [29] developed a porosity probability mapping approach based on short wavelength infrared imaging thermal features and micro CT data to predict LOF porosities. However, In all studies mentioned above, the target was detecting a specific type of porosity, and there was no attempt to avoid such defects.

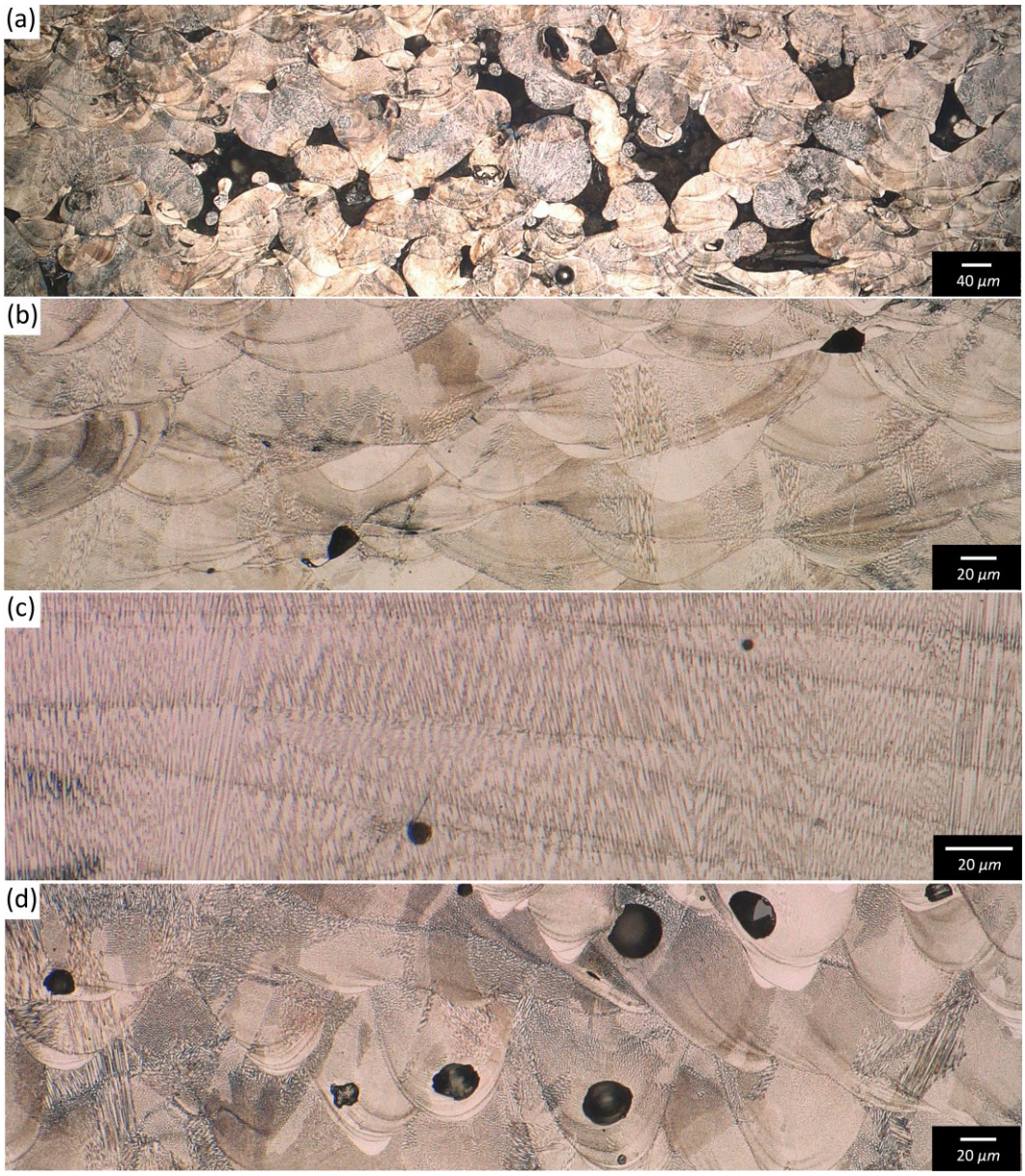

Figure 1-3 Types of porosities formed during the L-PBF processing of Inconel 625: (a) LOF porosity, with UM/PM particles, (b) LOP, with irregular porosities free from UM/PM particles, (c) gas porosity, and (d) keyhole porosity.

Forien et al. [30] showed that keyhole porosities could be predicted by signals received by a pyrometer, representing the temperature of the melt pool. Additionally, according to [31], the intensity of the melt pool radiation is proportional to the melt pool dimensions; thus,

LOF and LOP porosities which form when the size of the melt pool is relatively small to provide sufficient inter-track overlap can be correlated to the temperature signals. As a result, the likelihood of porosity formation can be monitored by a thermal sensor. Accordingly, temperature ranges corresponding to these defects can be discovered via temperature measurements, and consequently, a safe range of thermal signals can be determined to produce defect-free parts. The porosity level can be mitigated by keeping the temperature in the safe range using a control approach.

Surface roughness is another factor that should be considered in the quality of the products. The high surface roughness adversely impacts the mechanical properties of the final product, especially the fatigue performance, since surface asperities can act as preferential crack nucleation sites during cyclic loading [32,33]. The surface quality of the L-PBF fabricated parts can be categorized into two groups of side-surface and top surface quality. The surface roughness corresponding to the side surface originates mainly from the "stair-stepping effect"[4,34,35] and adhered powder particles. The former correlates to the layer thickness and part orientation, and the latter finds its route in powder attribute [36] (e.g., particle size and size distribution), meaning that both cannot be adjusted during the process. On the other hand, the top surface quality is related to defects (i.e., lack of inter-track overlap and balling), spatters, and the overlapping curvature of laser scan tracks [37–40].

At extremely high scanning speeds and relatively low laser powers, the elongated melt pools break up into smaller entities of spherical/semi-spherical shape to reduce the significant difference in the surface tension. This effect is known as the balling phenomenon (Figure 1-4(a)) [41–43].

Lack of inter-track overlap is referred to a situation in which the amount of energy delivered to the powder bed during the L-PBF process is not sufficient for the complete melting of the powder particles. (Figure 1-4(b)) [44–46]. At extremely low absorbed energy, the gap existing between adjacent tracks contains UM/PM powder particles. These openings in each layer make the layer thickness at some local regions larger for the subsequent layer, resulting in surface roughness deterioration or even process failure.

Spatters are caused by the Marangoni convection combined with the recoil pressure, which acts to eject the molten material from the melt pool to the surrounding [47,48]. Despite the low recoil pressure, which facilitates the melt pool flattening during the L-PBF process, the high recoil pressure caused by the extremely high absorbed energy leads to the material evaporation, melt explosion, and creation of metallic jets [49,50]. When crushed by the metallic vapor, the ejected material is broken into micro-sized molten droplets. The dispersed droplets are called spatters [51–53]. Figure 1-4(c) shows the spatters on the final layer, which can directly affect the surface roughness.

In cases where there is no gap between the adjacent laser scan tracks, the curvature of the tracks still results in the formation of peaks and valleys on the consolidated surface, leading to top surface roughness. The influence of this factor on the surface roughness alleviates by increasing the level of inter-track overlap [40].

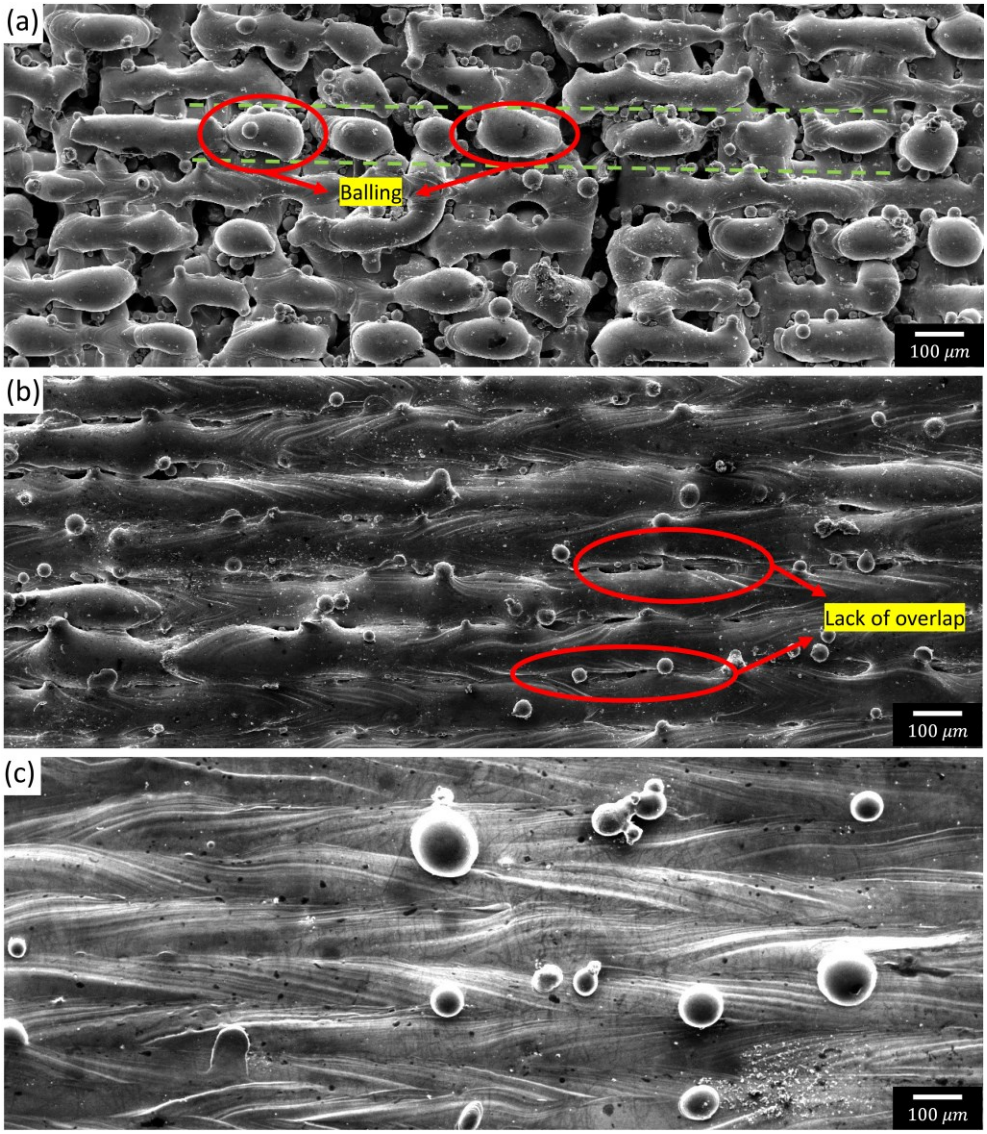

Figure 1-4 Factors that impact the surface quality: (a) Balling effect, (b) Lack of inter-track overlap, and (c) Spatters solidified on the top surface of the sample.

Two of the factors affecting the surface roughness, namely, lack of inter-track overlap and overlapping curvature of scan tracks, are correlated to the width of the melt pool [40,44]. According to [4], balling also can be correlated to the dimensions of the melt pool. In fact, the melt pool turns into the unstable mode when the ratio of the length to width of the melt pool transcends a certain value resulting in ball-shaped beads. Therefore, the melt pool

dimensions play a crucial role in forming the defects mentioned above. The dimensions of the melt pool depend on several factors, such as process variables, as well as the height and geometry of the part. For example, variations of scanning surface in building direction result in different melt pool temperatures and consequently melt pool dimensions in complex geometries [54]. In addition, the level of spatters also changes because of the mentioned factors. For instance, Gunenthiram et al. [55] showed that spatters increase by increasing the laser power. Therefore, a control approach that can control the dimensions of the melt pool and keep the level of spatters lower than a critical value solves the defects and consequently improves the surface quality of the part fabricated by the L-PBF process.

In order to control the quality of the product online, an appropriate monitoring system is essential. Specifically, a thermal monitoring system is required to control the microstructure that is related to the thermal dynamics of the process. The most common systems in additive manufacturing for measuring the melt pool temperature, heating rate, and cooling rate are pyrometers and thermal cameras. The sensors can be mounted on the L-PBF process chamber in an off-axial or a co-axial direction. For instance, an infrared camera has been used by Krauss et al. [56] (Figure 1-5) to investigate the limits for detecting pores and other irregularities during the L-PBF process. The camera was mounted outside the process chamber off-axially, and a germanium shielding glass was utilized to protect the camera from optical damage during laser processing. Pavlov et al. [57] used a two-color pyrometer in the configuration shown in Figure 1-6 co-axially to investigate the effects of the hatch distance, the layer thickness, and manufacturing strategy on the quality of the final product.

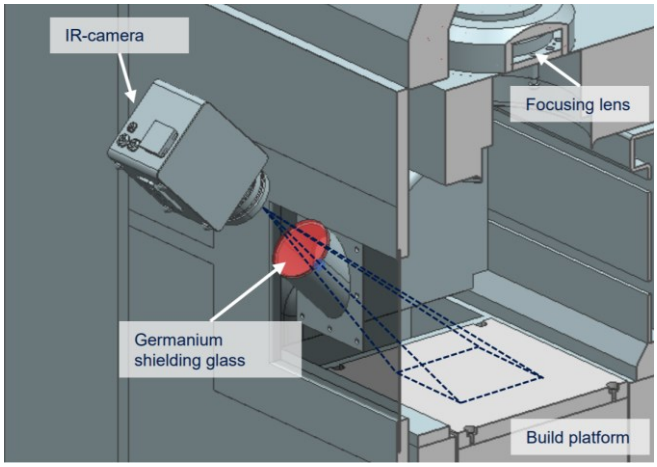

Figure 1-5 IR camera at 50 Hz sampling rate, 50 mm camera objective, Germanium shielding glass [56].

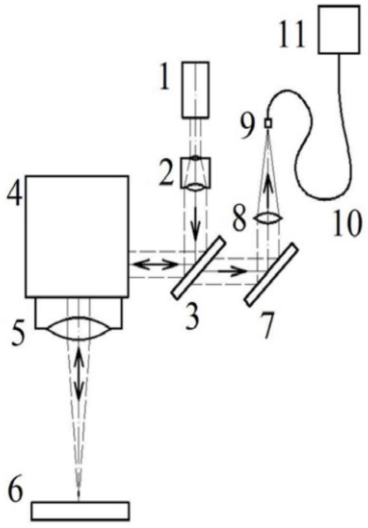

Figure 1-6 Schematic of the optical system applied [57].

Since there is a correlation between the surface roughness and the dimensions of the melt pool, monitoring the melt pool geometry is crucial. For this purpose, CCD or CMOS cameras are usually utilized. For instance, Fox et al. [58] utilized a high-speed CMOS camera in a co-axial arrangement to monitor the melt pool width and height during the L-PBF process.

Conventional methods for controlling the quality of the AM products are not automated and generalized for different process parameters. Furthermore, Additive manufacturing processes such as L-PBF and direct energy deposition (DED) are susceptible processes with concentrated heat sources and very high cooling rates. Thus, they are capable of producing very sensitive products with locally tailored microstructures. Besides, based on the discussion in this section, there is a correlation between the geometry of the melt pool and the surface roughness, which makes the AM process capable of improving the surface roughness. In addition, some automated approaches can reduce porosities correlated to the thermal dynamics of the melt pool. Overall, the AM process is capable of controlling the quality of the part indirectly, which is discussed in this report.

1.2 Motivation

Recently, additive manufacturing has caught the attention of the world [59]. According to IDTechEx, metal-based AM is the fastest-growing section in AM, and the upward trajectory will continue through 2020 [60]. More than 800 3D metal printers were sold in 2015- a growth of 46.9% over 2014. The main factor driving this growth in the market is the increasing use of metal printing processes in areas such as aerospace, defence, medical, and automotive. Well-known companies such as Siemens, NASA, Airbus, BMW, and Stryker are investing in this technology to produce a huge number of components such as fuel nozzles, blades for a gas turbine, rocket injectors, impeller wheels, and orthopedic implants. Therefore, they need to make sure about the quality of the final part and the repeatability of the AM process.

As mentioned, although the L-PBF process as an additive manufacturing technology is capable of processing a broad range of materials and has advantages over conventional methods, the parts fabricated by this process can have many issues that degrade their

quality, such as porosities or cracks, deformation resulting in dimensional errors, poor surface finish, as well as non-uniform properties which are more difficult to detect such as mechanical properties and microstructure characteristics. The part quality is mainly affected by process parameters and stochastic chamber environment, which can change the physics of the process. The process parameters are mostly kept constant in the literature, and the optimum process parameters are determined by the trial-and-error approach, which is time-consuming, costly, local, and machine/material-specific. In addition, as mentioned, the alteration of the L-PBF process with fixed process parameters decreases the reliability and repeatability of the process.

Today, in-process monitoring of the L-PBF process is a core of attraction to find the relation between the melt pool signature and the issues that happen during the process. The next big step for the L-PBF technology is to become fully automated in the sense that all desired material and geometry properties of products are locally tailored to the desired applications. Real-time control of the L-PBF process combined with an appropriate monitoring system will make the L-PBF process more reliable and repeatable.

Additionally, manipulation of the properties of the parts in building direction, which results in functionally graded parts required in different industries, will be achievable using the real-time control approaches.

1.3 Research objectives

The core aim of the current research is to improve the quality and increase the consistency of the Inconel 625 parts fabricated by the L-PBF process via control approaches. For this purpose, the microstructure consistency, porosity formation, and surface roughness of the

final parts were targeted in this thesis. The objective of this work could be refined into the followings:

1) Process modeling to find a correlation between laser power and features of the melt pool. The developed model can be used both for a better understanding of the process and for designing the model-based controllers.
2) Set up a monitoring system consisting of a pyrometer, a thermal camera, and a high-speed camera to monitor the L-PBF process and extract the features of the melt pool such as the melt pool thermal dynamics and melt pool shape, as well as some process signatures (spatters) during the process.
3) Design a control system for controlling the temperature of the melt pool and consequently making the microstructure of the final part more uniform.
4) Determine an optimum range of temperature for printing parts with high density instead of using the energy density criterion.
5) Design a PID controller to keep the temperature inside the safe range of temperature to mitigate the porosity formation.
6) Investigate factors that can affect the top surface quality.
7) Design a feedforward plus feedback control system to control the width of the melt pool and keep the level of spatters low, and consequently, improve the top surface quality of the part manufactured by the L-PBF process.

1.4 Thesis outline

Overall, the main results of this thesis have been prepared into three journal papers, in which two journal papers have already been published. One of the three journal papers is still under review. The thesis comprises of the following chapters:

Chapter 1 introduces the background and motivation of the research as well as the thesis objectives. It shows the new path in laser powder bed fusion and explains how this thesis contributes to making the process more reliable and repeatable.

Chapter 2 is the first published journal article. This chapter targets the microstructure properties of the Inconel 625 parts fabricated by the L-PBF process. The calibration of the pyrometer is discussed in this chapter. It also explains the variations of the microstructure in building direction. Moreover, the chapter presents the effect of three different controllers on the microstructure of the part. The effect of controllers on the microhardness of the part is also discussed in this chapter.

Chapter 3 is the second published journal article; it covers objectives 4 and 5. This chapter describes different types of porosities and how they form. The correlation between the temperature of the melt pool and each type of porosities is explained. The method of detecting the safe zone of temperature for printing parts using the L-PBF process is described in this chapter. The applicability of the energy density in predicting the densification level and defect type of the L-PBF fabricated parts is called into question. Finally, the performance of the PID controller in porosity formation mitigation at different scanning speeds and initial conditions is investigated in this chapter.

Chapter 4 is under-review research that deals with minimizing the top surface roughness of the parts manufactured by the L-PBF process by deploying a Feedforward plus Feedback control system. The factors affecting the top surface quality of the part, such as Balling, lack of inter-track overlap, overlapping curvature of laser scan tracks, and spatters, are described in this chapter. It also explains the in-process monitoring of melt pool width and spatters. An experimental model is developed, and a Feedforward plus

Feedback control system is designed accordingly. The performance of the controller is discussed at different scanning speeds in printing different geometries.

Chapter 5 summarizes the main conclusions and contribution of the thesis, highlights the strength and limitations, and presents some suggestions for future work. Finally, it defines the contribution of this thesis to the literature.

1.5 References

[1] S.A.M. Tofail, E.P. Koumoulos, A. Bandyopadhyay, S. Bose, L. O'Donoghue, C. Charitidis, Additive manufacturing: scientific and technological challenges, market uptake and opportunities, Mater. Today. 21 (2018) 22–37.

[2] W. Gao, Y. Zhang, D. Ramanujan, K. Ramani, Y. Chen, C.B. Williams, C.C.L. Wang, Y.C. Shin, S. Zhang, P.D. Zavattieri, The status, challenges, and future of additive manufacturing in engineering, Comput. Des. 69 (2015) 65–89.

[3] D.D. Gu, W. Meiners, K. Wissenbach, R. Poprawe, Laser additive manufacturing of metallic components: materials, processes and mechanisms, Int. Mater. Rev. 57 (2012) 133–164.

[4] T. DebRoy, H.L. Wei, J.S. Zuback, T. Mukherjee, J.W. Elmer, J.O. Milewski, A.M. Beese, A. Wilson-Heid, A. De, W. Zhang, Additive manufacturing of metallic components – Process, structure and properties, Prog. Mater. Sci. 92 (2018) 112–224. https://doi.org/10.1016/j.pmatsci.2017.10.001.

[5] N. Nadammal, T. Mishurova, T. Fritsch, I. Serrano-Munoz, A. Kromm, C. Haberland, P.D. Portella, G. Bruno, Critical role of scan strategies on the development of microstructure, texture, and residual stresses during laser powder bed fusion additive manufacturing, Addit. Manuf. 38 (2021) 101792. https://doi.org/10.1016/J.ADDMA.2020.101792.

[6] M.H. Ghoncheh, M. Sanjari, A.S. Zoeram, E. Cyr, B.S. Amirkhiz, A. Lloyd, M. Haghshenas, M. Mohammadi, On the microstructure and solidification behavior of new generation additively manufactured Al-Cu-Mg-Ag-Ti-B alloys, Addit. Manuf.

37 (2021) 101724. https://doi.org/10.1016/J.ADDMA.2020.101724.

[7] E. Fereiduni, A. Ghasemi, M. Elbestawi, Selective laser melting of aluminum and titanium matrix composites: Recent progress and potential applications in the aerospace industry, Aerospace. 7 (2020). https://doi.org/10.3390/AEROSPACE7060077.

[8] W.E. King, A.T. Anderson, R.M. Ferencz, N.E. Hodge, C. Kamath, S.A. Khairallah, A.M. Rubenchik, Laser powder bed fusion additive manufacturing of metals; physics, computational, and materials challenges, Appl. Phys. Rev. 2 (2015) 041304. https://doi.org/10.1063/1.4937809.

[9] S. Sanchez, P. Smith, Z. Xu, G. Gaspard, C.J. Hyde, W.W. Wits, I.A. Ashcroft, H. Chen, A.T. Clare, Powder Bed Fusion of nickel-based superalloys: A review, Int. J. Mach. Tools Manuf. 165 (2021) 103729. https://doi.org/10.1016/J.IJMACHTOOLS.2021.103729.

[10] B.L. Silva, I.J.C. Araujo, W.S. Silva, P.R. Goulart, A. Garcia, J.E. Spinelli, Correlation between dendrite arm spacing and microhardness during unsteady-state directional solidification of Al-Ni alloys, Philos. Mag. Lett. (2011). https://doi.org/10.1080/09500839.2011.559911.

[11] C.U. Brown, G. Jacob, A. Possolo, C. Beauchamp, M. Peltz, M. Stoudt, A. Donmez, The Effects of Laser Powder Bed Fusion Process Parameters on Material Hardness and Density for Nickel Alloy 625, NIST Adv. Manuf. Ser. (2018) 100–119. https://doi.org/10.6028/NIST.AMS.100-19.

[12] M.Ş. Turhal, T. Savaşkan, Relationships between secondary dendrite arm spacing

and mechanical properties of Zn-40Ai-Cu alloys, J. Mater. Sci. 38 (2003) 2639–2646. https://doi.org/10.1023/A:1024434602540.

[13] M.H. Farshidianfar, Control of microstructure in laser additive manufacturing, Master's thesis, University of Waterloo (2014).

[14] C. Qiu, H. Chen, Q. Liu, S. Yue, H. Wang, On the solidification behaviour and cracking origin of a nickel-based superalloy during selective laser melting, Mater. Charact. 148 (2019) 330–344. https://doi.org/10.1016/j.matchar.2018.12.032.

[15] M. Tang, P.C. Pistorius, J.L. Beuth, Prediction of lack-of-fusion porosity for powder bed fusion, Addit. Manuf. 14 (2017) 39–48. https://doi.org/10.1016/j.addma.2016.12.001.

[16] K. V. Yang, P. Rometsch, T. Jarvis, J. Rao, S. Cao, C. Davies, X. Wu, Porosity formation mechanisms and fatigue response in Al-Si-Mg alloys made by selective laser melting, Mater. Sci. Eng. A. 712 (2018) 166–174. https://doi.org/10.1016/j.msea.2017.11.078.

[17] M. Aminzadeh, T. Kurfess, In-situ quality inspection of laser powder-bed fusion using high-resolution visual camera images, Solid Free. Fabr. 2016 Proc. 27th Annu. Int. Solid Free. Fabr. Symp. - An Addit. Manuf. Conf. SFF 2016. (2016) 1412–1427.

[18] M. Aminzadeh, T.R. Kurfess, Online quality inspection using Bayesian classification in powder-bed additive manufacturing from high-resolution visual camera images, J. Intell. Manuf. 30 (2019) 2505–2523. https://doi.org/10.1007/s10845-018-1412-0.

[19] J.P. Oliveira, A.D. LaLonde, J. Ma, Processing parameters in laser powder bed fusion metal additive manufacturing, Mater. Des. 193 (2020) 1–12. https://doi.org/10.1016/j.matdes.2020.108762.

[20] A. du Plessis, Effects of process parameters on porosity in laser powder bed fusion revealed by X-ray tomography, Addit. Manuf. 30 (2019) 100871. https://doi.org/10.1016/j.addma.2019.100871.

[21] N.H. Paulson, B. Gould, S.J. Wolff, M. Stan, A.C. Greco, Correlations between thermal history and keyhole porosity in laser powder bed fusion, Addit. Manuf. 34 (2020). https://doi.org/10.1016/j.addma.2020.101213.

[22] M. Bayat, A. Thanki, S. Mohanty, A. Witvrouw, S. Yang, J. Thorborg, N.S. Tiedje, J.H. Hattel, Keyhole-induced porosities in Laser-based Powder Bed Fusion (L-PBF) of Ti6Al4V: High-fidelity modelling and experimental validation, Addit. Manuf. 30 (2019) 100835. https://doi.org/10.1016/j.addma.2019.100835.

[23] A. Simchi, H. Pohl, Effects of laser sintering processing parameters on the microstructure and densification of iron powder, Mater. Sci. Eng. A. 359 (2003) 119–128. https://doi.org/10.1016/S0921-5093(03)00341-1.

[24] Y. Li, D. Gu, Parametric analysis of thermal behavior during selective laser melting additive manufacturing of aluminum alloy powder, Mater. Des. 63 (2014) 856–867. https://doi.org/10.1016/j.matdes.2014.07.006.

[25] S.M. Yusuf, Y. Chen, R. Boardman, S. Yang, N. Gao, metals Investigation on Porosity and Microhardness of 316L Stainless Steel Fabricated by Selective Laser Melting, (2017). https://doi.org/10.3390/met7020064.

[26] G. Vastola, Q.X. Pei, Y.W. Zhang, Predictive model for porosity in powder-bed fusion additive manufacturing at high beam energy regime, Addit. Manuf. 22 (2018) 817–822. https://doi.org/10.1016/j.addma.2018.05.042.

[27] H. Choo, K.L. Sham, J. Bohling, A. Ngo, X. Xiao, Y. Ren, P.J. Depond, M.J. Matthews, E. Garlea, Effect of laser power on defect, texture, and microstructure of a laser powder bed fusion processed 316L stainless steel, Mater. Des. 164 (2019) 107534. https://doi.org/10.1016/j.matdes.2018.12.006.

[28] R. Liu, S. Liu, X. Zhang, A physics-informed machine learning model for porosity analysis in laser powder bed fusion additive manufacturing, Int. J. Adv. Manuf. Technol. 113 (2021) 1943–1958.

[29] C.S. Lough, T. Liu, X. Wang, B. Brown, R.G. Landers, D.A. Bristow, J.A. Drallmeier, E.C. Kinzel, Local Prediction of Laser Powder Bed Fusion Porosity by Short-Wave Infrared Imaging Thermal Feature Porosity Probability Maps, J. Mater. Process. Technol. (2021) 117473.

[30] J.-B. Forien, N.P. Calta, P.J. DePond, G.M. Guss, T.T. Roehling, M.J. Matthews, Detecting keyhole pore defects and monitoring process signatures during laser powder bed fusion: a correlation between in situ pyrometry and ex situ X-ray radiography, Addit. Manuf. (2020) 101336. https://doi.org/10.1016/j.addma.2020.101336.

[31] P. Mercelis, J.P. Kruth, J. Van Vaerenbergh, Feedback control of selective laser melting, Proc. 15th Int. Symp. Electromachining, ISEM 2007. (2007) 421–426.

[32] F. Froes, R. Boyer, Additive manufacturing for the aerospace industry, 2019.

https://books.google.com/books?hl=en&lr=&id=IlSIDwAAQBAJ&oi=fnd&pg=PP1&dq=Additive+manufacturing+for+the+aerospace+industry&ots=BBCf9CDqXn&sig=0t8xb-yvqN1Z1NHWXcRyfNCsLxU (accessed October 14, 2021).

[33] A. Uriondo, M. Esperon-Miguez, S. Perinpanayagam, The present and future of additive manufacturing in the aerospace sector: A review of important aspects:, Http://Dx.Doi.Org/10.1177/0954410014568797. 229 (2015) 2132–2147. https://doi.org/10.1177/0954410014568797.

[34] L. Dowling, J. Kennedy, S. O'Shaughnessy, D. Trimble, A review of critical repeatability and reproducibility issues in powder bed fusion, Mater. Des. 186 (2020) 108346. https://doi.org/10.1016/J.MATDES.2019.108346.

[35] I. Echeta, X. Feng, B. Dutton, R. Leach, S. Piano, Review of defects in lattice structures manufactured by powder bed fusion, Int. J. Adv. Manuf. Technol. 2019 1065. 106 (2019) 2649–2668. https://doi.org/10.1007/S00170-019-04753-4.

[36] M.A. Balbaa, A. Ghasemi, E. Fereiduni, M.A. Elbestawi, S.D. Jadhav, J.-P. Kruth, Role of powder particle size on laser powder bed fusion processability of AlSi10mg alloy, Addit. Manuf. 37 (2021) 101630.

[37] M. Khorasani, A. Ghasemi, U.S. Awan, E. Hadavi, M. Leary, M. Brandt, G. Littlefair, W. O'Neil, I. Gibson, A study on surface morphology and tension in laser powder bed fusion of Ti-6Al-4V, Int. J. Adv. Manuf. Technol. 2020 1119. 111 (2020) 2891–2909. https://doi.org/10.1007/S00170-020-06221-W.

[38] J. Snyder, K.T.-J. of Manufacturing, undefined 2020, Understanding laser powder bed fusion surface roughness, J. Manuf. Sci. Eng. 142 (2020) 071003.

https://asmedigitalcollection.asme.org/manufacturingscience/article-abstract/142/7/071003/1074958?casa_token=uW8Zv5PtNy4AAAAA:gW4LJ5YFU671VJryAnm2RAFbuSumFjHwIyKzkGBOTY-FbkuaydXAJk7Fi9w5bsUXlr8WSw (accessed October 27, 2021).

[39] R. Esmaeilizadeh, U. Ali, A. Keshavarzkermani, Y. Mahmoodkhani, E. Marzbanrad, E. Toyserkani, On the effect of spatter particles distribution on the quality of Hastelloy X parts made by laser powder-bed fusion additive manufacturing, J. Manuf. Process. 37 (2019) 11–20. https://doi.org/10.1016/J.JMAPRO.2018.11.012.

[40] D. Tanigawa, N. Abe, M. Tsukamoto, Y. Hayashi, H. Yamazaki, Y. Tatsumi, M. Yoneyama, Effect of laser path overlap on surface roughness and hardness of layer in laser cladding, Sci. Technol. Weld. Join. 20 (2015) 601–606.

[41] M. Grasso, B.M. Colosimo, Process defects and in situ monitoring methods in metal powder bed fusion: a review, Meas. Sci. Technol. 28 (2017) 044005. https://doi.org/10.1088/1361-6501/AA5C4F.

[42] D. Bourell, J.P. Kruth, M. Leu, G. Levy, D. Rosen, A.M. Beese, A. Clare, Materials for additive manufacturing, CIRP Ann. 66 (2017) 659–681. https://doi.org/10.1016/J.CIRP.2017.05.009.

[43] L. Li, J.Q. Li, T.H. Fan, Phase-field modeling of wetting and balling dynamics in powder bed fusion process, Phys. Fluids. 33 (2021) 042116. https://doi.org/10.1063/5.0046771.

[44] A. Sola, A. Nouri, Microstructural porosity in additive manufacturing: The

formation and detection of pores in metal parts fabricated by powder bed fusion, J. Adv. Manuf. Process. 1 (2019). https://doi.org/10.1002/AMP2.10021.

[45] R. Snell, S. Tammas-Williams, L. Chechik, A. Lyle, E. Hernández-Nava, C. Boig, G. Panoutsos, I. Todd, Methods for Rapid Pore Classification in Metal Additive Manufacturing, Jom. 72 (2020) 101–109. https://doi.org/10.1007/s11837-019-03761-9.

[46] M. Abdelrahman, E.W. Reutzel, A.R. Nassar, T.L. Starr, Flaw detection in powder bed fusion using optical imaging, Addit. Manuf. 15 (2017) 1–11. https://doi.org/10.1016/j.addma.2017.02.001.

[47] R. Fabbro, M. Hamadou, F. Coste, Metallic vapor ejection effect on melt pool dynamics in deep penetration laser welding, J. Laser Appl. 16 (2004) 16–19.

[48] H. Nakamura, Y. Kawahito, K. Nishimoto, S. Katayama, Elucidation of melt flows and spatter formation mechanisms during high power laser welding of pure titanium, J. Laser Appl. 27 (2015) 32012.

[49] A. Matsunawa, J.-D. Kim, N. Seto, M. Mizutani, S. Katayama, Dynamics of keyhole and molten pool in laser welding, J. Laser Appl. 10 (1998) 247–254.

[50] R. Fabbro, S. Slimani, I. Doudet, F. Coste, F. Briand, Experimental study of the dynamical coupling between the induced vapour plume and the melt pool for Nd–Yag CW laser welding, J. Phys. D. Appl. Phys. 39 (2006) 394.

[51] H. Zheng, H. Li, L. Lang, S. Gong, Y. Ge, Effects of scan speed on vapor plume behavior and spatter generation in laser powder bed fusion additive manufacturing, J. Manuf. Process. 36 (2018) 60–67.

https://doi.org/10.1016/J.JMAPRO.2018.09.011.

[52] X. Zhang, B. Cheng, C. Tuffile, Simulation study of the spatter removal process and optimization design of gas flow system in laser powder bed fusion, Addit. Manuf. 32 (2020) 101049. https://doi.org/10.1016/J.ADDMA.2020.101049.

[53] L.E. Criales, Y.M. Arısoy, B. Lane, S. Moylan, A. Donmez, T. Özel, Laser powder bed fusion of nickel alloy 625: Experimental investigations of effects of process parameters on melt pool size and shape with spatter analysis, Int. J. Mach. Tools Manuf. 121 (2017) 22–36. https://doi.org/10.1016/J.IJMACHTOOLS.2017.03.004.

[54] R. Yavari, A. Riensche, E. Tekerek, L. Jacquemetton, H. Halliday, M. Vandever, A. Tenequer, V. Perumal, A. Kontsos, Z. Smoqi, K. Cole, P. Rao, Digitally twinned additive manufacturing: Detecting flaws in laser powder bed fusion by combining thermal simulations with in-situ meltpool sensor data, Mater. Des. 211 (2021) 110167. https://doi.org/10.1016/J.MATDES.2021.110167.

[55] V. Gunenthiram, P. Peyre, M. Schneider, M. Dal, F. Coste, I. Koutiri, R. Fabbro, Experimental analysis of spatter generation and melt-pool behavior during the powder bed laser beam melting process, J. Mater. Process. Technol. 251 (2018) 376–386. https://doi.org/10.1016/J.JMATPROTEC.2017.08.012.

[56] H. Krauss, C. Eschey, M.F. Zaeh, Thermography for Monitoring the Selective Laser Melting Process, n.d. https://pdfs.semanticscholar.org/a5bc/9f471e3600ef0478db089394f582226ee5b3.pdf (accessed June 10, 2020).

[57] M. Pavlov, M. Doubenskaia, I. Smurov, Pyrometric analysis of thermal processes in SLM technology, Phys. Procedia. 5 (2010) 523–531. https://doi.org/10.1016/j.phpro.2010.08.080.

[58] J.C. Fox, B.M. Lane, H. Yeung, Measurement of process dynamics through coaxially aligned high speed near-infrared imaging in laser powder bed fusion additive manufacturing, in: Thermosense Therm. Infrared Appl. XXXIX, International Society for Optics and Photonics, 2017: p. 1021407.

[59] C.K. Chua, M. Vadakke Matham, Y.-J. Kim, Lasers in 3D printing and manufacturing, World Scientific, 2017.

[60] 3D Printing of Metals 2019-2029: IDTechEx, (n.d.). https://www.idtechex.com/en/research-report/3d-printing-of-metals-2019-2029/667 (accessed December 31, 2021).

Chapter 2

On-line melt pool temperature control in L-PBF additive manufacturing

Complete Citation:

Rezaeifar, Hossein, and M. A. Elbestawi. "On-line melt pool temperature control in L-PBF additive manufacturing." *The International Journal of Advanced Manufacturing Technology* 112, no. 9 (2021): 2789-2804. https://doi.org/10.1007/s00170-020-06441-0

Abstract:

Laser powder bed fusion is a promising additive manufacturing technology which has enabled the fabrication of complex-shape, custom-designed, and cost-effective parts with no need for expensive tools and dies. Despite the numerous advantages of this technology, inconsistency in the microstructure and, consequently, the mechanical properties of the fabricated components in the building direction makes it quite challenging to obtain uniform parts in the as-built state. This issue originates from the layer-by-layer melt pool temperature variation caused by the layer-wise nature of this process when a fixed set of process parameters are applied. Accordingly, a layer-wise melt pool temperature control system is beneficial in manipulating the process parameters and therefore adjusting the melt pool temperature. In this study, three different controllers, namely, simple proportional (P), adaptive P, and quasi sliding mode, were designed to control the melt pool temperature in the building direction for Inconel 625 superalloy. An analytical-experimental model was introduced to evaluate the performance of controllers through simulation. A monitoring system having a two-color pyrometer was used to online monitor the temperature for use by the controllers as a feedback signal. The microstructure and microhardness of the final products were evaluated prior to and after employing the melt pool temperature controllers. Compared to the scenario with constant process parameters, the implementation of these controllers led to improved microhardness and microstructure uniformity, resulting from the reduced variation in the primary dendrite arm spacing. The lessons learned from this study can assist in the fabrication of functionally graded materials with engineered microstructures.

Keywords:

Laser powder bed fusion, Control, Melt pool temperature, Microstructure, Microhardness

Abbreviations

AM	Additive Manufacturing
CAD	Computer-Aided Design
CMOS	Complementary Metal Oxide Semiconductor
FGM	Functionally Graded Material
LI	Length of Interval
L-PBF	Laser Powder Bed Fusion
PID	Proportional-Integral-Derivative
PI	Proportional-Integral
SEM	Scanning Electron Microscope
Q-SMC	Quasi Sliding Mode Control

2.1 Introduction

Laser powder bed fusion (L-PBF) is a promising additive manufacturing (AM) technique, which has drawn a great deal of attention in recent years for fabricating complex shapes with intricate features in a layer-by-layer manner (Figure 2-1) directly from a Computer-Aided Design (CAD) model without the necessity of designing complicated build tools [1–5]. The emergence of L-PBF as a novel processing method has opened a new window to fabricate parts with unique microstructural and mechanical properties different from those produced by conventional manufacturing methods. In general, several experiments or time-consuming simulations are needed to determine the optimal process parameters alleviating the formation of defects [6]. Nevertheless, since the average temperature of the build increases gradually during the L-PBF process due to the heat accumulation phenomenon [7], a fixed set of process parameters (i.e., laser power, scanning speed, hatch spacing, and powder layer thickness) may lead to components with non-uniform microstructure and consequently varying mechanical properties.

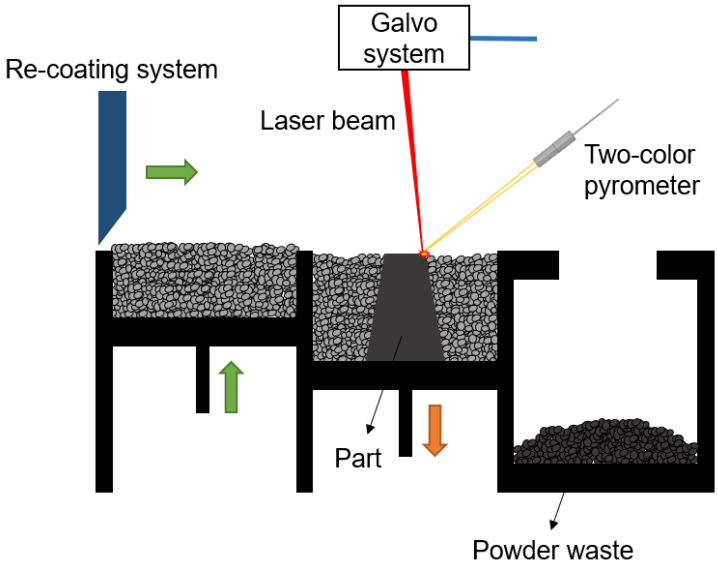

Figure 2-1 Schematic illustration of a laser powder bed fusion (L-PBF) system.

To address the abovementioned issue in a reasonable time, a dynamically adjustable system is essential to manipulate the process parameters to end up with a nearly constant temperature along the build. In other words, microstructure characteristics depend on the solidification process, which is directly related to the thermal dynamics of the melt pool. Therefore, it is necessary to control the thermal dynamics of the molten material to achieve desired attributes (e.g., uniform microstructure and functionally graded materials) in a cost-effective approach. Moreover, because the mechanical properties of the final parts are governed by the microstructural features, melt pool temperature control not only reduces the microstructural discrepancy but also results in consistent mechanical properties (e.g., microhardness) throughout the part [8,9].

A few attempts have been made recently to control the L-PBF process. A study in NIST (National Institute of Standards and Technology) discussed the control requirements and its essential equipment, such as monitoring systems, laser systems, and computational resources [10]. They also explained the concept of a control system suitable for the L-PBF process. In another study, a coaxial monitoring system consisting of a photodiode and a complementary metal oxide semiconductor (CMOS) camera was employed to control the melt pool area [11]. By applying a first-order transient behavior for the transfer function between the melt pool area and laser power, the fabrication of overhang structures was improved when a proportional-integral-derivative (PID) controller was utilized. According to a latter work conducted by the same authors [12], a photodiode was used to transmit melt pool area information, and a proportional-integral (PI) controller was utilized to enhance the dimensional accuracy in two different cases, namely, slow scanning speed and downfacing surface condition. However, both studies shared the same drawback of using a PID controller with fixed parameters, which lacks to guarantee a robust control for

different conditions in the nonlinear AM processes. Besides, by considering the proportional relation between the photodiodes signals and the melt pool area [11], the output voltage from the photodiodes are quite small in comparison to the real values of the melt pool area. Therefore, a small error in the results leads to a considerable error in the melt pool area measurements, making the melt pool unstable. The EU founded project MEGaFiT established a study on controlling the AM process by means of a thermal camera, a color sensor, and a topography sensor. After introducing the concept of their control design [13], three proportional (P) controllers with different gains were designed to control the melt pool temperature by a pyrometer [14]. However, output values were reported in voltage, the same as [11], and the controller had a fixed gain. Besides, a comparison among a P controller, a model-based feedforward controller, and the combination of these two controllers was implemented to evaluate the improvement in the quality of the bridge structure [15]. In all the studies mentioned above, the quality of the parts was examined in a macro-scale, while micro-scale features dictating the mechanical properties were ignored. Therefore, microscopic features should be scrutinized from the control point of view.

This research study, for the first time, proposes an adaptive P controller and a quasi sliding mode controller (Q-SMC) to control the melt pool temperature of Inconel 625 superalloy in the L-PBF process by manipulating the laser power. The conventional simple P controller was also implemented as a reference to evaluate the performance of the newly proposed control systems in terms of the rise time and robustness against disturbances. For this purpose, a model that simulates the L-PBF process is first suggested and validated by experimental measurements using a two-color pyrometer calibrated in advance. Then, the responses of the proposed controllers are simulated. Finally, the controllers are

experimentally implemented in the L-PBF machine. Using the proposed controllers and setting two different reference temperatures, the influence of the controller type and the temperature on the microstructure and microhardness of the fabricated parts is investigated and compared with the uncontrolled scenario. The knowledge gained from the microstructural characterization and microhardness measurements reinforce the idea that the application of an appropriate control system can not only reduce the microstructural and microhardness variations in the building direction but also provides the opportunity to fabricate functionally graded materials (FGMs).

2.2 Modeling and control strategies

2.2.1 Simulation modeling

Different modeling methods are utilized to check the controller response before running an experiment. Among those, analytical modeling and system identification approaches are used for control purposes since the numerical method is extremely time-consuming, while a fast response is required for a control system.

An analytical model has been proposed by Ning et al. [16] using a moving point heat source solution, which was originally propounded by Carslaw and Jaeger [17] to find the temperature distribution profile inside and around the melt pool. Although the radiation and convection heat transfers are ignored in this equation, the laser absorption coefficient, latent heat of fusion, and powder packing density have been taken into consideration:

$$\theta(x,y,z,t) = \frac{P\eta}{2Rk\pi^{\frac{3}{2}}} \exp\left(\frac{Vx}{2\kappa}\right) \int_{\frac{R}{2\sqrt{\pi t}}}^{\infty} \exp\left[-\xi^2 - \left(\frac{V^2R^2}{16\kappa^2\xi^2}\right)\right] d\xi \tag{2-1}$$

where $P, \eta, V, k, t,$and κ denote the laser power, laser absorption coefficient, laser scanning velocity, thermal conductivity coefficient, current time, and thermal diffusivity,

respectively. ξ is an integral variable. The terms "θ" and "R" in Eq. (2-1) are temperature change and distance, respectively defined as:

$$\theta = T - T_0 \tag{2-2}$$

$$R^2 = x^2 + y^2 + z^2 \tag{2-3}$$

in which T_0 and T signify the initial temperature and the current temperature of the desired location and time, respectively. x,y, and z specify each point uniquely in the Cartesian coordinate system. Given the fact that the temperature of a certain location on each layer at a known time is required in this study, and the scanning speed is constant during the control process (V_e), t can be substituted by $\frac{x}{V_e}$. In addition, since the temperature of a single point in each layer is measured by the pyrometer, it is not essential to have the temperature distribution profile ($y = 0$ and $z = z_s$). Therefore, Eq. (2-1) can be rewritten as presented in Eq. (2-4).

$$\theta\left(x, 0, z_s, \frac{x}{V_e}\right) = \frac{P\eta}{2Rk\pi^{\frac{3}{2}}} \exp\left(\frac{V_e x}{2\kappa}\right) \int_{\frac{R}{2\sqrt{\pi\frac{x}{V_e}}}}^{\infty} \exp\left[-\xi^2 - \left(\frac{{V_e}^2 R^2}{16\kappa^2\xi^2}\right)\right] d\xi \tag{2-4}$$

In Eq. (2-4), z_s is the height of the measuring point. According to the model in Eq. (2-1), the temperature of the molten material for Inconel 625 was reported to be 4000 ℃, which is unrealistic because evaporation would happen at this high temperature. In addition, the model suffers from a singularity problem. In this study, the model is constructed based on Eq. (2-4), while experimental data are also used to correct the abovementioned issues. By defining a variable $B_c = f(P, V)$ to solve this, the final equation will be as follows:

$$\theta\left(x,0,z_s,\frac{x}{V_e}\right)=\frac{P\eta B_c}{2\pi^{\frac{3}{2}}}\exp\left(\frac{V_e x}{2\kappa}\right)\int_{\frac{R}{2\sqrt{\pi\frac{x}{V_e}}}}^{\infty}\exp\left[-\xi^2-\left(\frac{{V_e}^2(x^2+z_s^2)}{16\kappa^2\xi^2}\right)\right]d\xi \tag{2-5}$$

The thermophysical material properties of the Inconel 625 are listed in Table 2-1. The function f has been obtained by implementing several experiments, including 12 random laser powers from 150 W to 400 W and 10 random scanning speeds from 200 mm/s to 600 mm/s (120 experiments) with fixed hatch spacing and layer thickness. By polynomial fifth-order approximation, the following equation can be drawn:

$$B_c=\sum_{n=0}^{5}\sum_{m=0}^{5}p_{nm}\,P^n V^m \tag{2-6}$$

where p represents the coefficient of the polynomial function while n and m are integers from 0 to 5.

The modeling results are depicted in Figure 2-2. For validating the results, a pyrometer has been employed to measure the melt pool temperature (Figure 2-1). Based on Figure 2-2, it is self-evident that the model outputs are in good agreement with the experimental results achieved by two measurement approaches for the mentioned range of laser power and scanning speed. The temperature shows an ascending trend by increasing the laser power and a descending trend by increasing the scanning speed as expected. It should be born in mind that by increasing the laser power or decreasing the scanning speed, the melt pool size is enhanced, and the level of evaporation is increased as well. Therefore, the melt pool resists against a huge change in temperature. The response of the control systems using this model is discussed in section 2.2.2.4.

2.2.2 Controller design

The models of the AM processes have a number of time-varying parameters and coefficients, such as laser power absorption, conductivity, and diffusivity of the material. Additionally, there is a dynamic environment inside the chamber that can alter the process and measurements. For instance, vapor and dust change the ratio of radiation energy, which is the basis of the temperature measurement. According to [18–20], PID controllers with fixed gains are sensitive to the abovementioned processes and adaptive gains, and nonlinear controllers provide better results in such conditions.

Table 2-1 Material properties of Inconel 625 used for the simulation [16].

Laser Absorption $\boldsymbol{\eta}$ (%)	Thermal Conductivity $\boldsymbol{k}$ ($\boldsymbol{W/m-}$ °C)	Thermal Diffusivity $\boldsymbol{\kappa}$ ($\boldsymbol{mm^2/s}$)
40	9.8	2.71

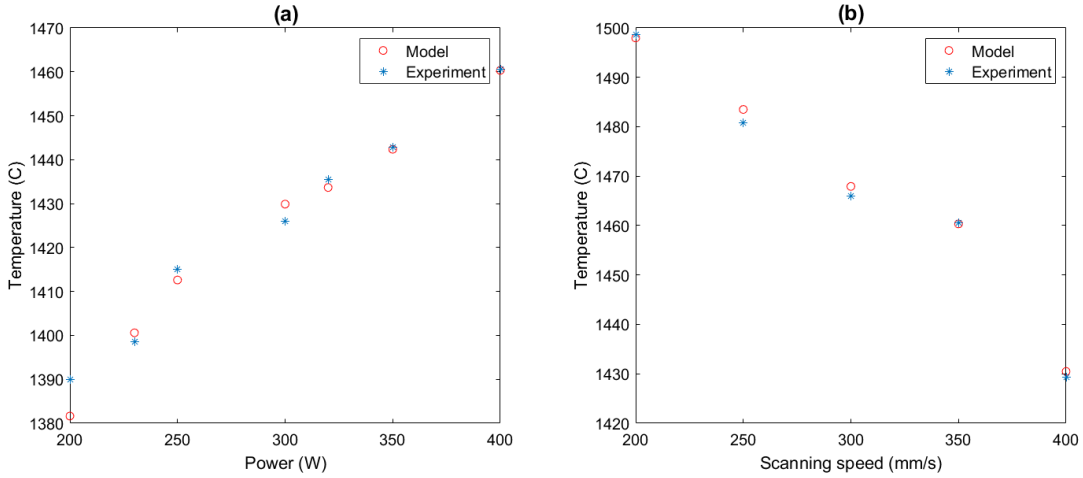

Figure 2-2 (a) Variations of the melt pool temperature as a function of the laser power in the fixed scanning speed of 350 mm/s, and (b) effect of the scanning speed on the melt pool temperature under the fixed laser power of 400 W.

In this study, a feedback control system using signals achieved by the pyrometer was implemented. Three different types of controllers, including conventional P, adaptive P, and Q-SMC, were investigated, and results were compared.

2.2.2.1 P controller

According to Figure 2-3, the error in the loop can be obtained by subtracting the reference temperature from the signal captured by the pyrometer as:

$$e = T_r - T_s \tag{2-7}$$

where T_r is the reference temperature, and T_s is the temperature sensed by the pyrometer. The P-controller with the proportional gain k_p calculates the laser power output, u_i, at the layer i as:

$$u_i = u_{(i-1)} + k_p.e \tag{2-8}$$

Based on Eq. (2-8), the controller output is obtained by adding the proportional section to the previous laser power. The controller output was limited between 170 W and 400 W since the laser system of the machine cannot work over 400 W, and the system identification has been applied in this range.

2.2.2.2 Adaptive P controller

By considering the first layer and Eq. (2-5) in the modeling section, the temperature of the scanned point captured by the pyrometer has a direct relation with the initial laser power $u(0)$ and the initial temperature of the powder layer $T_0(1)$, which is considered to be equal to the environment temperature.

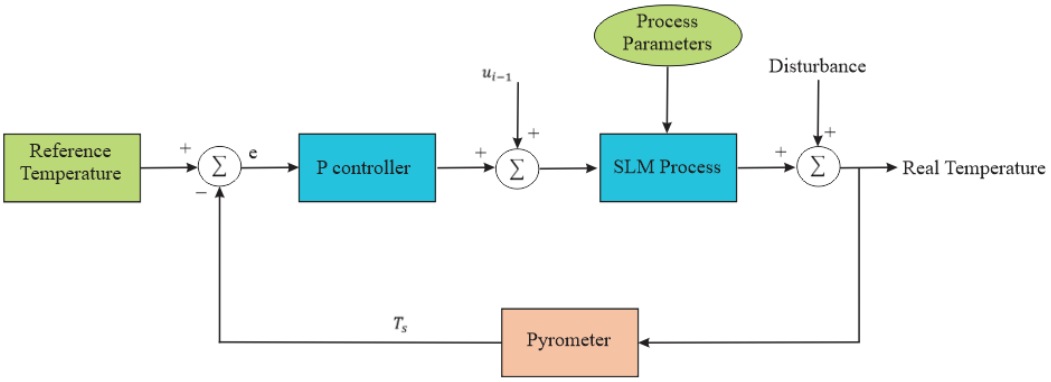

Figure 2-3 Block diagram of the employed P controller.

$$T_1(x_L, y_L, 0, t_L) = \frac{P\eta B_c}{2k\pi^{\frac{3}{2}}} exp\left(\frac{V_e x_L}{2\kappa}\right) \int_{\frac{R}{2\sqrt{\pi t_L}}}^{\infty} exp\left[-\xi^2 - \left(\frac{{V_e}^2 R^2}{16\kappa^2 \xi^2}\right)\right] d\xi + T_0(1) \quad (2\text{-}9)$$

$$\Rightarrow T_1 \rightarrow u(0), T_0(1)$$

After the laser beam scanned the first layer, the exposed material cools down through convection, radiation, and conduction heat transfer mechanisms in a certain amount of time. All these heat transfer mechanisms have a direct relationship with the measured temperature of the first layer (T_1), so that the initial temperature for the second layer is related to the captured temperature of the first layer. Therefore, the temperature of the second layer is affected by $u(1)$ and T_1 as follows:

$$T_2(x_L, y_L, 0, t_L) = \frac{P\eta B_c}{2k\pi^{\frac{3}{2}}} \exp\left(\frac{V_e x_L}{2\kappa}\right) \int_{\frac{R}{2\sqrt{\pi t_L}}}^{\infty} \exp\left[-\xi^2 - \left(\frac{{V_e}^2 R^2}{16\kappa^2 \xi^2}\right)\right] d\xi + T_0(2) \quad (2\text{-}10)$$

$$\Rightarrow T_2 \rightarrow u(1), T_0(2) \text{ or } u(1), T_1$$

Hence, the discrete model of the process can be explained as:

$$T(k) = a(k)T(k-1) + b(k)u(k-1) \quad (2\text{-}11)$$

Eq. (2-11) is used as a process model in designing the adaptive controller. The aim of using this controller is to make the temperature error equal to zero. Using Eqs. (2-7), (2-8), and (2-11), the error can be derived as Eq. (2-12).

$$T(i-1) = a(i-1)T(i-2) + b(i-1)u(i-2) \tag{2-12a}$$

$$e(i-1) = T_r(i-1) - T(i-1) \tag{2-12b}$$

$$= T_r(i-1) - [a(i-1)T(i-2) + b(i-1)u(i-2)\,]$$

$$u(i-1) = u(i-2) + k_p\big[T_r(i-1) - [a(i-1)T(i-2) + b(i-1)u(i-2)\,]\big] \tag{2-12c}$$

$$e(i) = T_r(i) - T(i) = T_r(i) - [a(i)u(i-1) + b(i)u(i-1)\,] = \tag{2-12d}$$

$$T_r(i) - \Big[b(i)\Big[u(i-2) + k_p\big[T_r(i-1) - [a(i-1)T(i-2) + b(i-1)u(i-2)\,]\big]\Big] + a(i)T(i-1)\Big]$$

In order to have $e(i) = 0$, the proportional gain will be:

$$k_p = \frac{T_r(i-1) - a(i)T(i-1) - b(i)u(i-2)}{b(i)[T_r(i-1) - a(i-1)T(i-2) - b(i-1)u(i-2)]} \tag{2-13}$$

Using recursive least square (RLS) estimation, the terms a and b can be determined [21]. The model presented in Eq. (2-11) can be rewritten as:

$$y(k) = \emptyset^T(k)\hat{\theta}(k) \tag{2-14a}$$

$$\emptyset(k) = [-T(k-1)\;\; u(k-1)]^T \tag{2-14b}$$

$$\hat{\theta}(i) = \big[\hat{a}(i), \hat{b}(i)\big]^T \tag{2-14c}$$

where $\emptyset(k)$ is data vector, and $\hat{\theta}$ is the parameter vector. The cost function is:

$$J(\hat{\theta},k)=\frac{1}{2}\sum_{i=1}^{k}\lambda^{k-1}\left[y(i)-\emptyset^{T}(i)\hat{\theta}(i)\right]^{2} \tag{2-15}$$

The recursive solution for minimizing the cost function is:

$$\hat{\theta}(k)=\hat{\theta}(k-1)+ \tag{2-16a}$$

$$L(k)\left(y(k)-\emptyset^{T}(k)\hat{\theta}(k-1)\right)$$

$$L(k)=\frac{P(k-1)\emptyset(k)}{\lambda I+\emptyset^{T}(k)P(k-1)\emptyset(k)} \tag{2-16b}$$

$$P(k)=\left(I-L(k)\emptyset^{T}(k)\right)\frac{P(k-1)}{\lambda} \tag{2-16c}$$

in which λ is the exponential forgetting factor, L represents the gain vector, and P is the error covariance matrix. $\lambda=0.99$, since the process has disturbance and slow changes. Figure 2-4 shows the block diagram of the adaptive P controller.

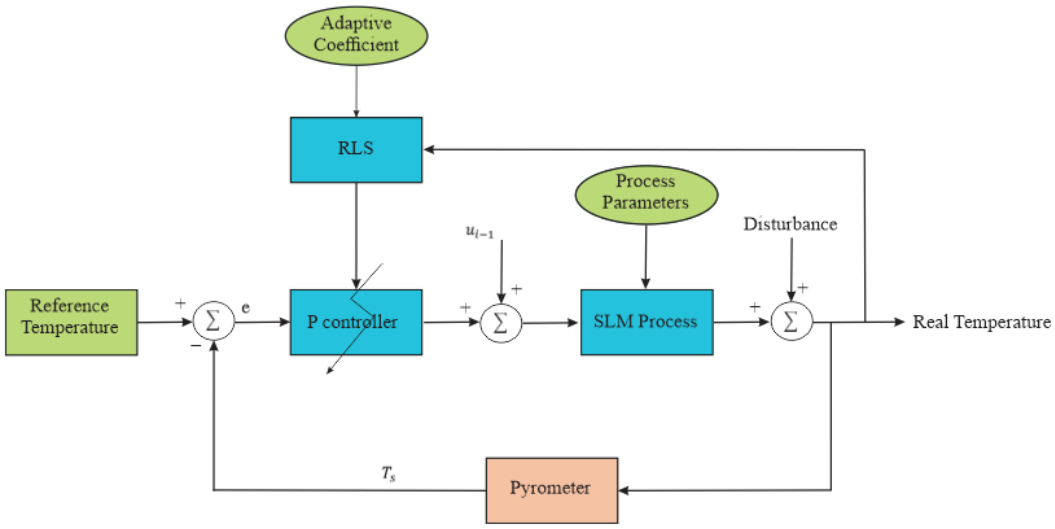

Figure 2-4 The block diagram of the adaptive P controller. The coefficient of the controller is updated after printing each layer.

2.2.2.3 Quasi sliding mode controller

For the Q-SMC, the discrete controller presented in [22] is used to control the temperature, the only difference being that not only the coefficient corresponding to the states but also other parameters are considered to be time-variant in the model. The sliding surface is:

$$S(k) = C\big(T(k) - T_r(k)\big) \tag{17}$$

where $C = 1$ based on the model presented in Eq. (2-11). The sliding dynamics is defined as $S(k) \equiv 0$ which is asymptotically stable. In this case, the controller output will be:

$$u(k) = u(k-1) + \tag{18}$$

$$[Cb(k)]^{-1}\big[(\gamma - 1)S(k) - C[a(k)T(k) - a(k-1)T(k-1)]\big]$$

in which $u(k)$ is the laser power calculated for the layer $(k+1)$, and γ is an arbitrary number such that $S(k+1) = \gamma S(k)$ is asymptotically stable ($|\gamma| < 1$). The schematic of the Q-SMC controller is presented in Figure 2-5.

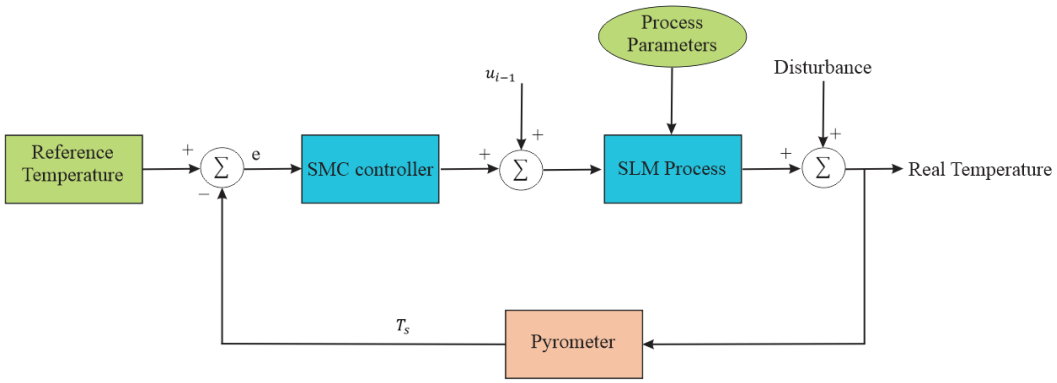

Figure 2-5 Quasi sliding mode control block diagram.

2.2.2.4 Simulation results

For comparing the performance of controllers, the sum of the squared error is used, as defined in Eq. (19):

$$J = \sum_{i=1}^{N} \left(T_r(i) - T(i)\right)^2 \tag{2-19}$$

An identical noise that simulates the noise and errors of the sensor was applied to all systems with different controllers. Figure 2-6(a) represents the results of the three control systems. As it is evident, the applied noise is significant in the process. The true temperature, which is calculated by the model in Eq. (2-5), is shown in Figure 2-6(b). All the controllers were successful in keeping the temperature around the desired value. The following points can be extracted from Figure 2-6:

1. The response time of the adaptive P controller is shorter than the other ones.
2. The sum of the squared error in the Q-SMC controller is the minimum among the others (Table 2-2).
3. Compared to the others, the Q-SMC controller is more robust against the applied noise.

Table 2-2 Performance analysis of controllers in two different scenarios.

	P controller	Adaptive P controller	Q-SMC controller
J in Scenario 1	5632.9	4715.5	3137.9
J in Scenario 2	13448	8138.2	16175

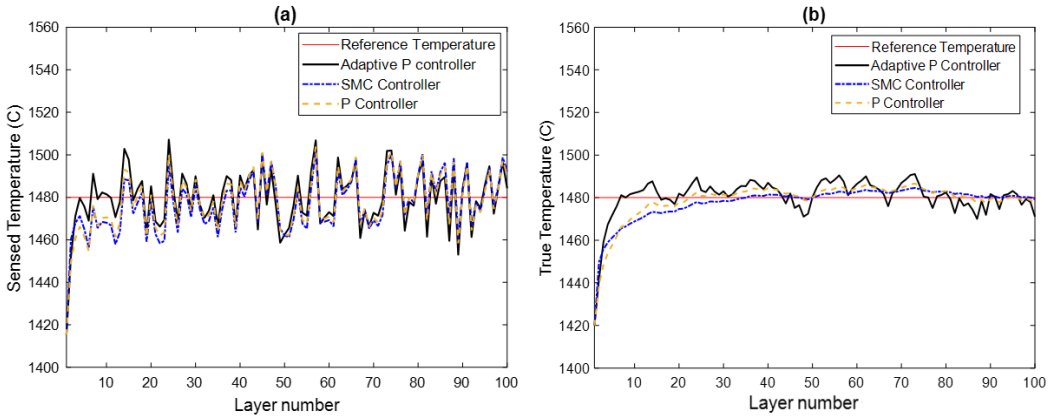

Figure 2-6 (a) The temperature sensed by the virtual sensor with an identical noise and error for all controllers, and (b) the true temperature calculated by the model based on the controllers' command. The adaptive controller responded faster while the quasi sliding mode controller was more robust against noises and errors.

The reason for the slow response of the Q-SMC controller can be explained by the gain setting used in the control law in [22], which was too small. A faster response would be possible with another gain setting (Figure 2-7). However, the slow response of this controller will be helpful to understand the change in the microstructure during the transition time of the controller.

Figure 2-8 shows the input laser power for each layer using different controllers. It emphasizes that the adaptive P controller increases the laser power drastically at the start of the process, making the melt pool temperature closer to the desired temperature faster than the two other controllers.

To investigate the controllers more precisely, another scenario with two different temperatures was designed. Figure 2-9 shows the results of three controllers in the second scenario. The main findings from Figure 2-9 are as follows:

1. The Q-SMC used in this study is too slow to reach the second desired temperature.

2. The adaptive P controller performed better than other controllers in this case (Table 2-2).
3. The response time of the adaptive P controller is considerably shorter than the others (Figure 2-9 and 2-10)

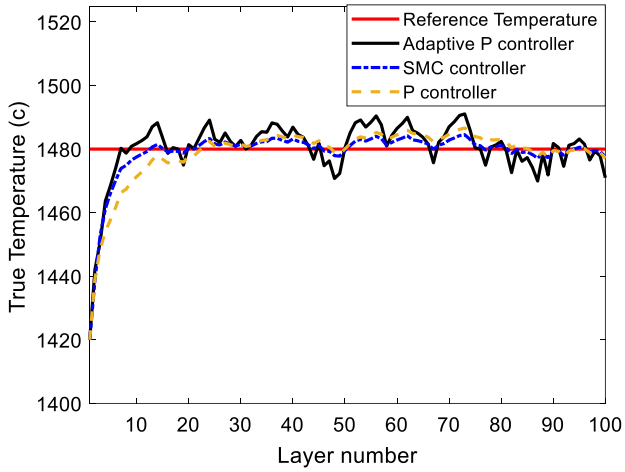

Figure 2-7 The true temperature calculated by the model based on the controllers' command with modified gain setting in the Q-SMC controller.

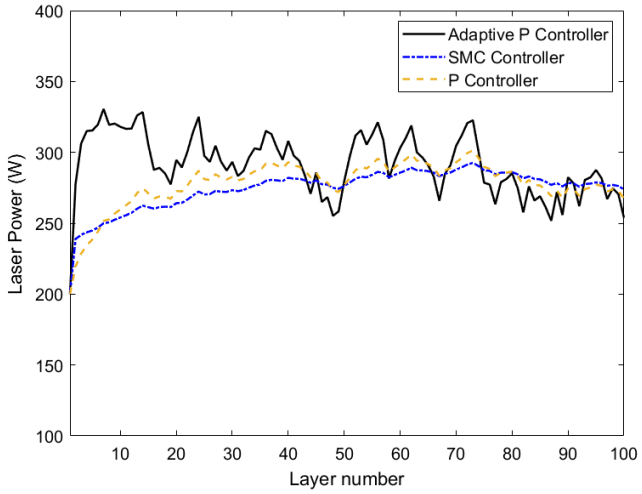

Figure 2-8 The laser power in each layer for different controllers when a fixed desired temperature is set (first scenario).

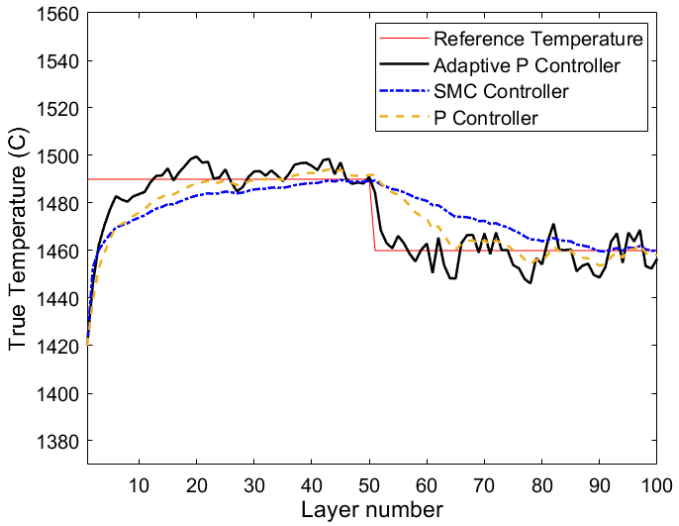

Figure 2-9 The true temperature when two different reference temperatures were set (second scenario). The Q-SMC is noticeably slow to switch between two desired temperatures.

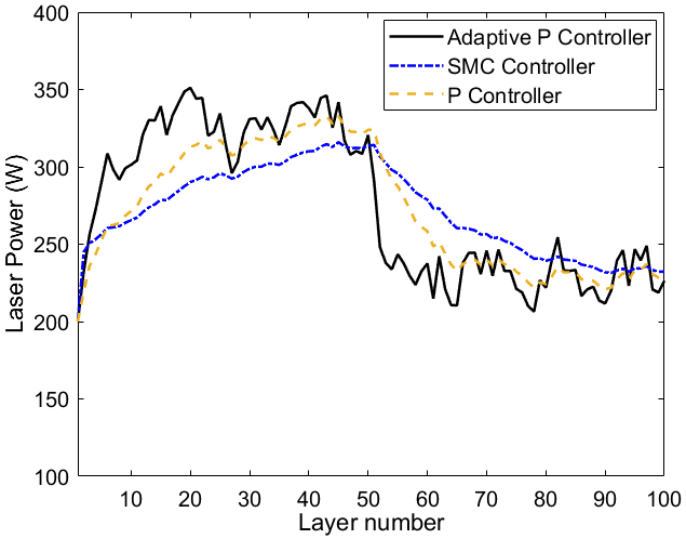

Figure 2-10 The laser power when two different reference temperatures were set (second scenario).

In summary, the adaptive P controller performed better than two others in the simulation study, although, in some layers, it had a higher error. In section 2.4, these controllers are compared from the part microstructure point of view.

2.3 Experimental setup

The L-PBF machine deployed in this study was OmniSint-160 having a 400 W Yb-fiber laser with a spot size of 100 μm. The printing process was performed under the protection of a high-purity argon gas atmosphere. Laser power, which is a critical process parameter in the AM process, can be changed between layers in this machine, enabling the control of the process.

The material used in the study was Inconel 625 in the form of powder with the chemical composition provided in Table 2-3.

The monitoring system consists of a two-color pyrometer, capable of measuring the highest temperature in its spot area. The detectable temperature range of this pyrometer lies between 1000 ℃ to 3200 ℃, with a sample rate of 1 kHz. The spot size of the pyrometer is 800 μm. Before using a contactless temperature measurement system such as a pyrometer, it is essential to know some properties of the material under investigation, specifically, the emissivity of the material. In the case of a two-color pyrometer, it is necessary to adjust the emissivity slope of the device (the ratio of emissivity at two wavelengths). The most effective way to determine and adjust the slope is to take the temperature of the material using a probe sensor such as a thermocouple or other suitable devices. Once the sensor determines the actual temperature, the slope setting should be adjusted until the pyrometer reads the same temperature as the actual one. To perform this procedure for Inconel 625, a vacuum induction furnace with an argon gas atmosphere was used to heat the sample. It is a very suitable environment, resembling that of the L-PBF machine in which the sensor is used. The setup is shown in Figure 2-11. A B-type

thermocouple was used as a probe sensor to measure the actual temperature. The Inconel 625 powder was melted in a crucible and was spotted with the pyrometer (Figure 2-12).

Table 2-3 The nominal chemical composition of the Inconel 625 used in this study.

Element	Al	C	Co	Cr	Cu	Fe	Mo	Mn	Nb+Ta	Ni	P	S	Si	Ti
Min (wt%)	-	-	-	20.0	-	-	8.0	-	3.15	Bal	-	-	-	-
Max (wt%)	0.4	0.1	1.0	23.0	0.5	5.0	10.0	0.5	4.15	Bal	0.015	0.015	0.5	0.4
Result	0.11	0.02	0.02	22.0	<0.1	0.3	9.0	<0.01	3.80	Bal	<0.001	0.001	0.07	0.11

Figure 2-11 A general view of the setup used to calibrate the pyrometer.

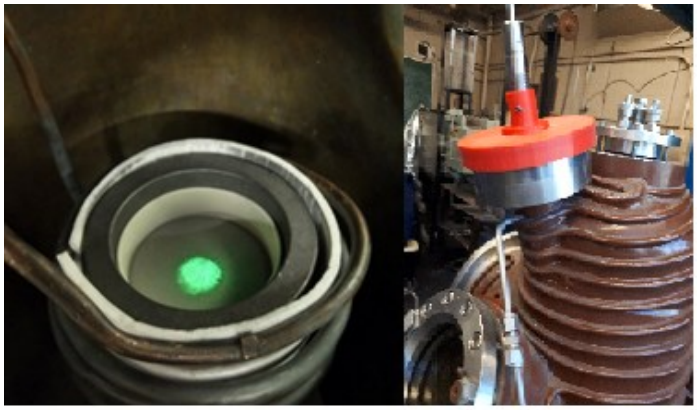

Figure 2-12 (a) Overview of the crucible with the pyrometer spotted area, and (b) pyrometer configuration on the vacuum induction furnace.

The final result of the calibration is shown in Figure 2-13. The noise at the beginning of the thermocouple curve is due to the Eddy currents induced by the induction coil on the thin thermocouple leads.

As soon as the current is reduced to zero, the signal becomes noise-free. In Figure 2-13, there is a strong agreement between the pyrometer and thermocouple temperature readings.

The investigation procedure and control process were carried out on a thin wall with dimensions of $1.5\,mm \times 35\,mm \times 8\,mm$, printed on a small disk (Figure 2-14). The scanning speed, hatch spacing, and layer thickness were $200\,{}^{mm}/_{s}$, $80\,\mu m$, and $40\,\mu m$, respectively, throughout the experiment. Also, the initial laser power was $200\,W$, which was manipulated by the controllers in the subsequent layers. Based on the scanning speed, spot size, and sampling rate of the pyrometer, the melt pool fell into the spot area of the pyrometer. The scanning pattern and the shielding gas flow direction are shown in Figure 2-15. The argon gas was being fed from the top of the process chamber toward the build plate during the L-PBF process. A sequential scanning pattern with no rotation between

the subsequent layers was utilized for all of the samples. It should be mentioned that control systems were performed using LabVIEW on the Omnisit-160 L-PBF machine.

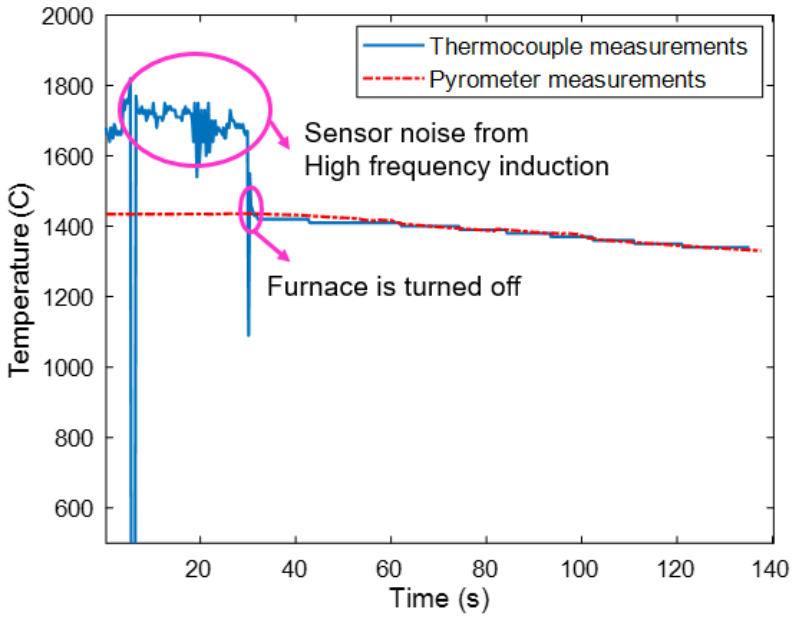

Figure 2-13 Diagrams showing temperature versus time for the measurements performed by the thermocouple and pyrometer. The results were in agreement when the slope coefficient was 0.96.

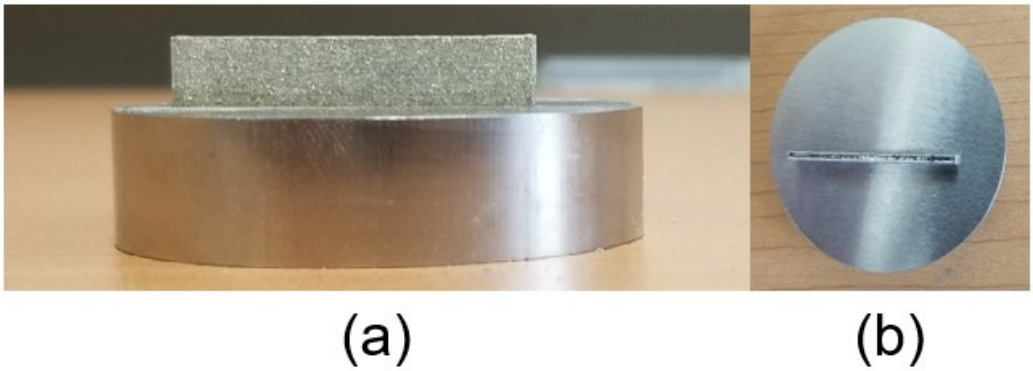

Figure 2-14 The: (a) side view, and (b) top view of the thin wall printed on the disk.

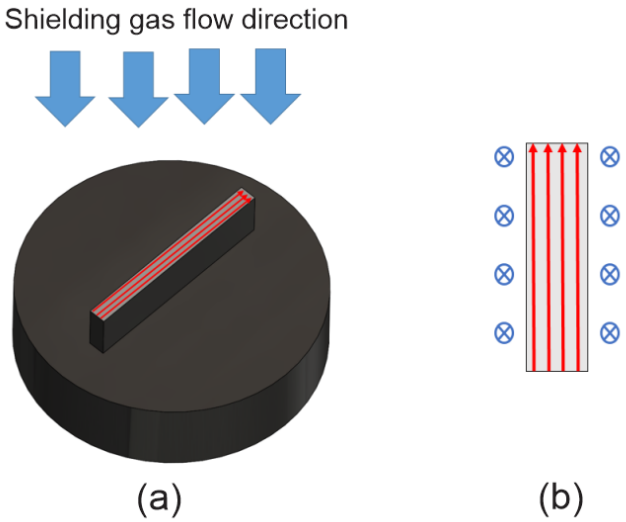

Figure 2-15 (a) A 3D view of the scanning pattern and the shielding gas flow direction, and (b) 2D view of scanning pattern with shielding gas flow direction flowing from the top of the chamber toward the build plate (blue cross).

It is of note that no geometrical defects (in macro-scale) were observed even in the part manufactured by the fixed laser power since the process parameters were selected to be close to those leading to the defect-free Inconel 625 parts.

The fabricated thin walls were sectioned along the building direction, and microstructural investigations were performed on the cross-sections. The standard metallographic technique was used to prepare samples. For microstructural examinations, mixed acid etchant with the following composition was used: HCl-75 ml and HNO_3-25 ml. Detailed imaging of the microstructure was conducted by a TESCAN VEGA scanning electron microscopy (SEM) working at 20 kV accelerating voltage. The image-J Software was utilized to calculate the intercellular spacing known as the primary dendrite arm spacing (PDAS) based on the SEM images.

The microhardness test was conducted on different locations of the cross-section with an applied load and dwell time of 200 g and 10 s, respectively.

2.4 Results and Discussions

2.4.1 Control performance

The performance of the controllers was investigated by two sets of experiments with different reference temperatures. For this purpose, a thin wall with 200 layers was fabricated using an initial laser power of 200 W and reference temperatures of 1490 ℃ (1st set) and 1450 ℃ (2nd set). The reference temperatures were chosen based on the range of the melt pool temperatures in the nearly defect-free zone acquired by pre-experiment. 140℃ (first set of the experiment) and 100℃ (second set of the experiment) degree of overheating with respect to the liquidus temperature did not result in any macro-scale defects such as warpage and delamination (Figure 2-14).

As mentioned, the temperature was measured in each layer at a fixed location. Figure 2-16 represents the temperature measurements using three controllers for the 1st set. Besides, the laser power in each layer, which was decided by the controllers for the first set, is shown in Figure 2-17. The adaptive P controller, Q-SMC, and simple P controller reached the desired temperature after 10, 18, and 37 layers, respectively. Therefore, the rise time of the adaptive P controller is significantly shorter than that of the other controllers. This feature can be useful when the purpose of control is jumping to a specific temperature at a specific height of the part. For example, when FGM is the aim of the fabrication, the adaptive P controller reacts faster to any deviation from the reference temperature in comparison to the other controllers. In addition, as mentioned in section 2.2.2.4, the Q-SMC is more robust against external disturbances.

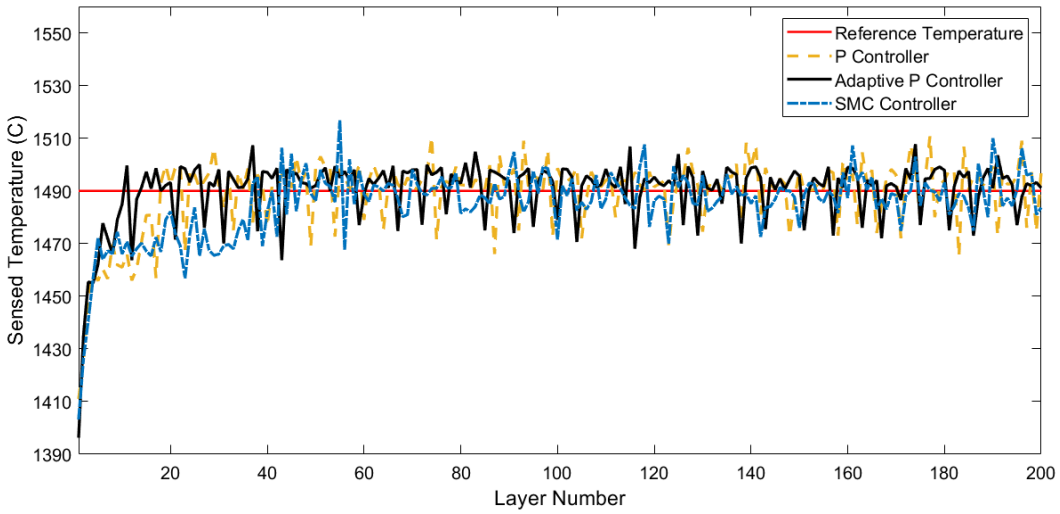

Figure 2-16 The temperature sensed by the pyrometer for all controllers (1st set). The adaptive P controller responded faster compared to the other controllers.

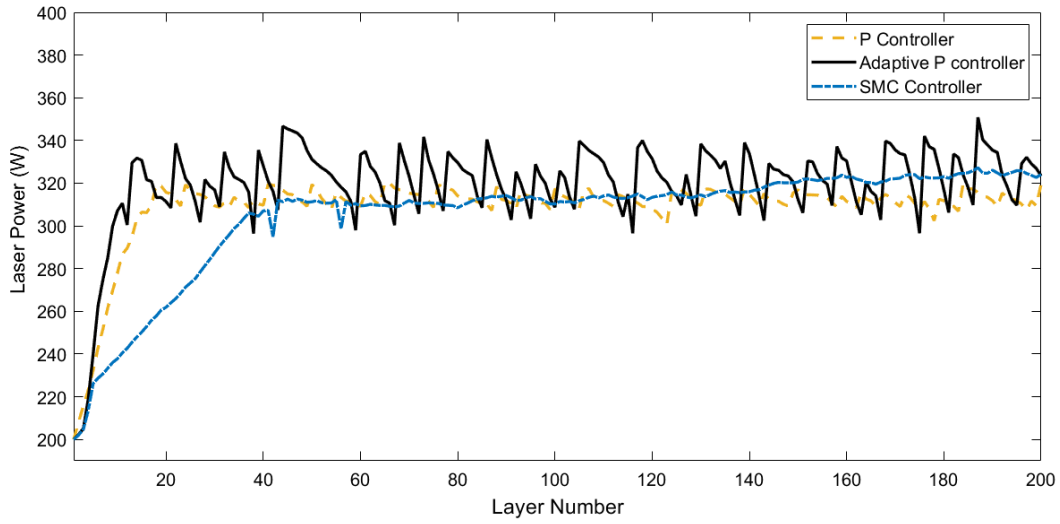

Figure 2-17 The laser power versus the layer number for different controllers (1st set).

In contrast, the adaptive P controller behaves more aggressively compared to other controllers. Referring to Table 2-4, it is reasonable to conclude that the adaptive P controller works more efficiently when the application requires fast response, owing to the fact that the mean temperature in this scenario is closer to the reference temperature. Moreover, the standard deviation of the data captured by the pyrometer for the adaptive P

controller is smaller than those of the other controllers. However, if the abovementioned terms are investigated after a specific layer number above which all controllers have reached the desired temperature (e.g., layer 40), the Q-SMC has the lowest standard deviation. Thus, if the initial layers are of lower importance (parts with support structures), the Q-SMC can be a competitor to the adaptive P controller for controlling the melt pool temperature of the top layers.

Figure 2-18 shows the temperature measurements for the 2nd set of experiments, in which the difference between the initial temperature and the desired temperature is smaller than the 1st set. In this set, the temperature with all controllers reached the desired temperature significantly sooner, and their rise times were closer compared to the 1st set. After 8, 10, 15 layers, the desired temperature was achieved by the adaptive P controller, simple P controller, and the Q-SMC, respectively. Therefore, knowledge about the initial error can be valuable in the control process. It is worth mentioning that different gains were tested in simulation for the simple P controller to reach the best gain that works for both desired

Table 2-4 The evaluation of the controller performance in the 1st set of experiments.

Controller	Mean temperature (Layer 1 to 200)	Standard deviation (Layer 1 to 200)	Mean temperature (Layer 40 to 200)	Standard deviation (Layer 40 to 200)
Simple P	1489.2	13.95	1492.09	9.29
Adaptive P	1490.3	12.42	1491.95	8.2
Q-SMC	1485.08	13.02	1489.35	7.64

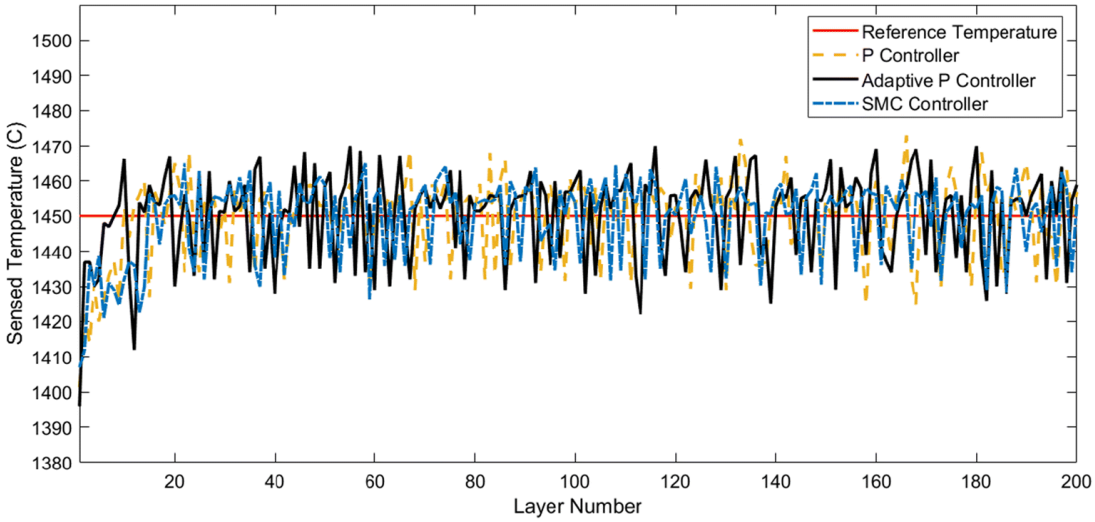

Figure 2-18 The temperature sensed by the pyrometer for all controllers (2nd set).

temperatures. Otherwise, for each specific temperature, a particular gain should be set using several experiments [14]. Table 2-5 shows the mean temperature and the standard deviation of the data for the 2nd set of experiments and confirms the points discussed based on Table 2-4.

2.4.2 Microstructure results

To investigate the effect of the temperature control on the microstructure of the final products, a thin wall was also fabricated with a fixed laser power of 250 W as the reference sample. All parts were cut from the pyrometer spot location in the vertical direction. Then, they were divided into three distinct regions (bottom, middle, and top), as shown in Figure 2-19. The microstructural features of each region were scrutinized based on SEM micrographs.

According to [23], the microstructure of the Inconel 625 part fabricated by the L-PBF process is in the cellular dendritic form. The primary dendrite arm spacing (PDAS) (Figure 2-20) was used as a metric for microstructural characterization purposes. After gathering

Table 2-5 The evaluation of the controller performance in the 2nd set of experiments.

Controller	Mean temperature (Layer 1 to 200)	Standard deviation (Layer 1 to 200)	Mean temperature (Layer 40 to 200)	Standard deviation (Layer 40 to 200)
Simple P	1449.6	11.78	1450.92	10.38
Adaptive P	1450.26	12.83	1450.9	12.04
Q-SMC	1449.43	11.26	1450.35	9.67

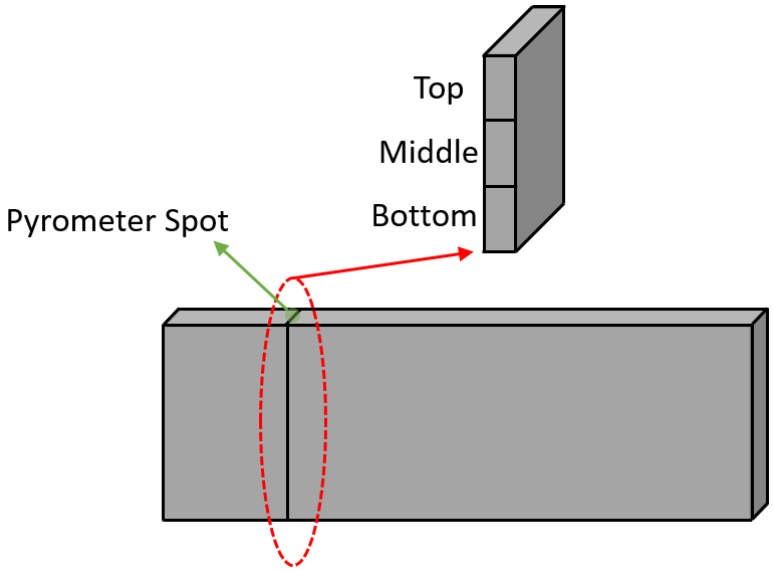

Figure 2-19 The cutting location of the final parts along with the regions in which the microstructural characterization was performed.

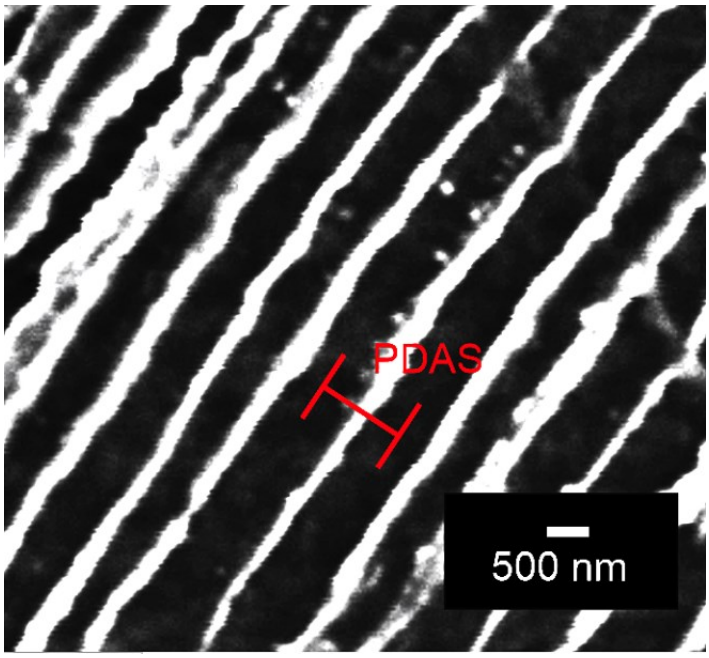

Figure 2-20 SEM micrograph showing the primary dendrite arm spacing (PDAS).

the images, the PDASs of different sections were measured. The Image-J Software was utilized to measure the PDAS of controlled and uncontrolled parts. The field of view for the measurement of the PDAS was 30 μm × 30 μm.The reported values for each case are the average of at least twenty distinct measurements on different images.

Figure 2-21 represents the measurements of the PDAS in different cases of the 1st set of experiments in different regions. It indicates that regardless of the regions, the length of interval (LI) of the PDAS became shorter when a controller was employed during the process. Figure 2-22 shows the variation in the temperature during the building for the uncontrolled case. The large variations of the PDAS can be traced back to the change in temperature as opposed to the controlled scenario. For instance, LI of the PDASs throughout the part was calculated to be 0.557 μm and 0.165 μm in uncontrolled and adaptive P controller cases, respectively. The two other controllers also made the LI of the PDAS shorter in comparison to the fixed laser power case. Then it can be concluded that

when controllers come into action, more uniform microstructures are achievable. The second point that can be inferred from Figure 2-21 is that the LI in the bottom region, where the controllers still struggle to reach the desired temperature, is larger than the middle and top regions. Nevertheless, the LI in the bottom region of the part fabricated by the adaptive P controller is shorter than those of the Q-SMC and simple P controller due to the faster response of the adaptive P controller. The middle and top regions of all controlled samples have virtually the same range of the PDAS, meaning that the process has reached a near-uniform state prior to the middle region. Moreover, the mean value of the PDAS in the uncontrolled case with fixed laser power of 250 W was lower compared to the controlled scenarios in the middle and top regions (Figure 2-21). According to Figure 2-17, the laser powers during the controlled processes were higher than 300 W in those regions. Given the fact that the higher laser power in controlled cases results in larger melt pools and, consequently, lower cooling rates, the lower mean values of the PDAS in the uncontrolled case is justifiable [24].

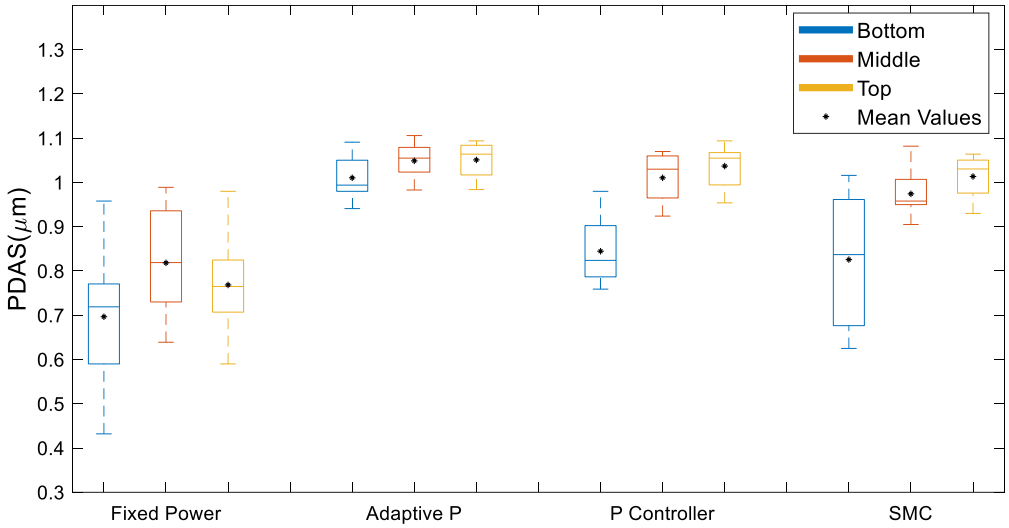

Figure 2-21 PDAS variations in different regions while using fixed laser power and controllers for the desired temperature of 1490 ℃ (1st set).

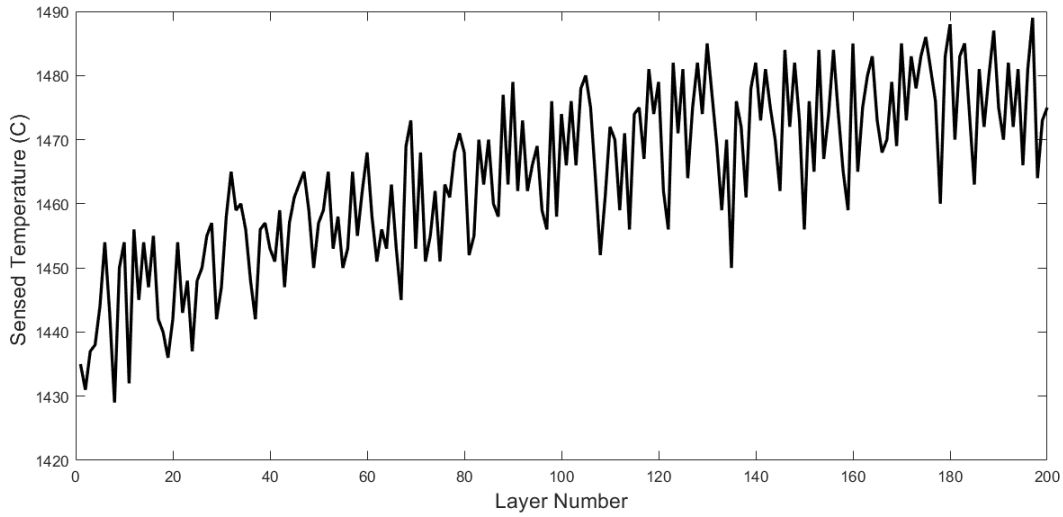

Figure 2-22 The temperature sensed by the pyrometer for the fixed laser power of 250 W. The temperature sensed by the pyrometer for the fixed laser power of 250 W. The sensed temperature was increased during the build.

The PDAS measurements of the 2nd set of experiments are illustrated in Figure 2-23. The same discussion parallel to that of the 1st set of experiments is valid for this case, which is

confirmed by the SEM micrographs provided in Figure 2-24. According to Figure 2-24, a more uniform microstructure is achieved when the adaptive P controller is implemented. It is worth noting that the mean values of the PDAS in the 2nd set of experiments are lower than the 1st set. For example, the mean value of PDAS with the adaptive controller is 1.051 μm at the top of the part when the desired temperature is 1490 ℃ while it is 0.8225 μm in the 2nd set of experiments. This is originated from the faster cooling rates associated with, the smaller melt pools, which were created at lower temperature and laser power in 2nd set. The high magnification micrographs of the parts (in the middle region) fabricated under adaptive P controllers at desired temperatures of 1450 ℃ and 1490 ℃ are shown in Figure 2-25, confirming the above discussion. In addition, the LI of the Q-SMC controller changed from 0.391 μm in the 1st set to 0.286 μm in the 2nd set since the desired melt pool temperature was achieved sooner in the latter case.

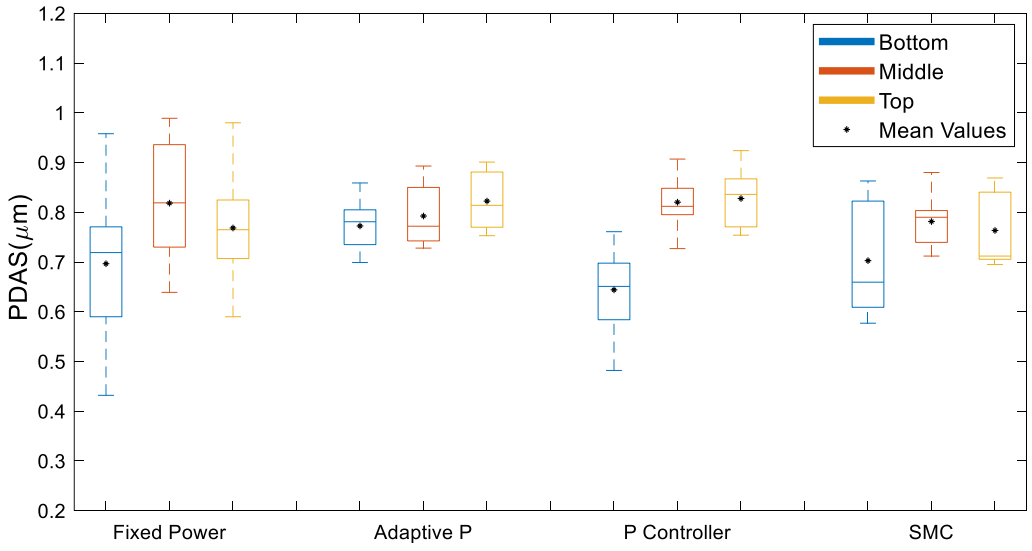

Figure 2-23 PDAS variations in different sections while using fixed laser power and controllers for the desired temperature of 1450 ℃.

2.4.3 Microhardness results

To study the mechanical properties of the printed parts under controlled and uncontrolled conditions, the microhardness was measured in the building direction, starting from the height of 3 mm. The microhardness measurement results are summarized in Table 2-6. The following outcomes can be outlined from the microhardness results:

1. The microhardness increased by increasing the desired temperature in a statistically significant manner. The same trend has been observed for Inconel 625 elsewhere in which the increase of the laser power led to higher microhardness values [25].
2. When a controller was deployed, the microhardness range became smaller than the case in which a fixed laser power was utilized. This is attributed to the shorter LI of the PDAS and, therefore, more uniform microstructures achieved by employing the controllers (Figure 2-21 and Figure 2-23).

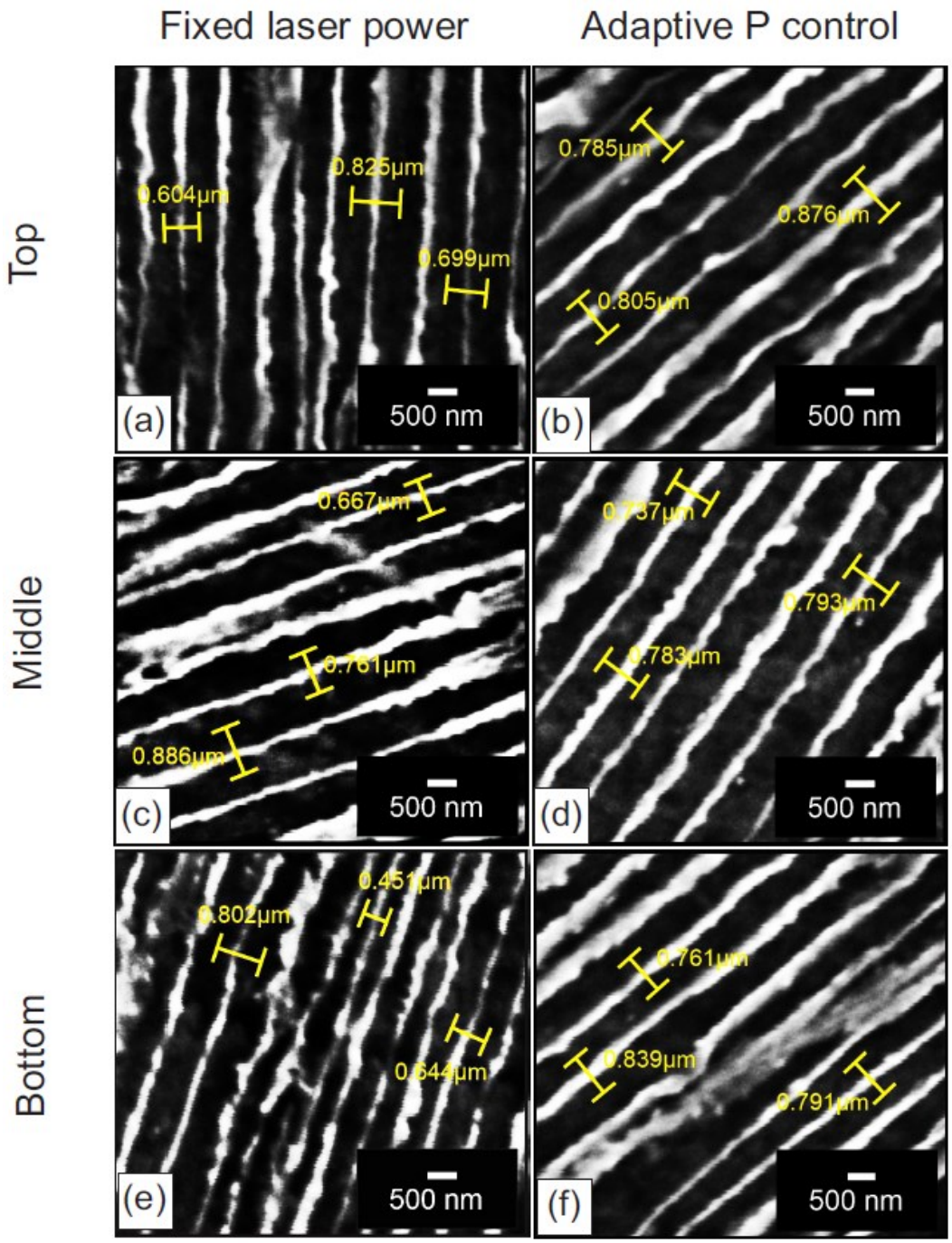

Figure 2-24 SEM micrographs of parts with the: (a), (c), (e) fixed set of process parameters, and (b), (d), (f) adaptive P controller (2nd set). The sample measurements are provided in each micrograph.

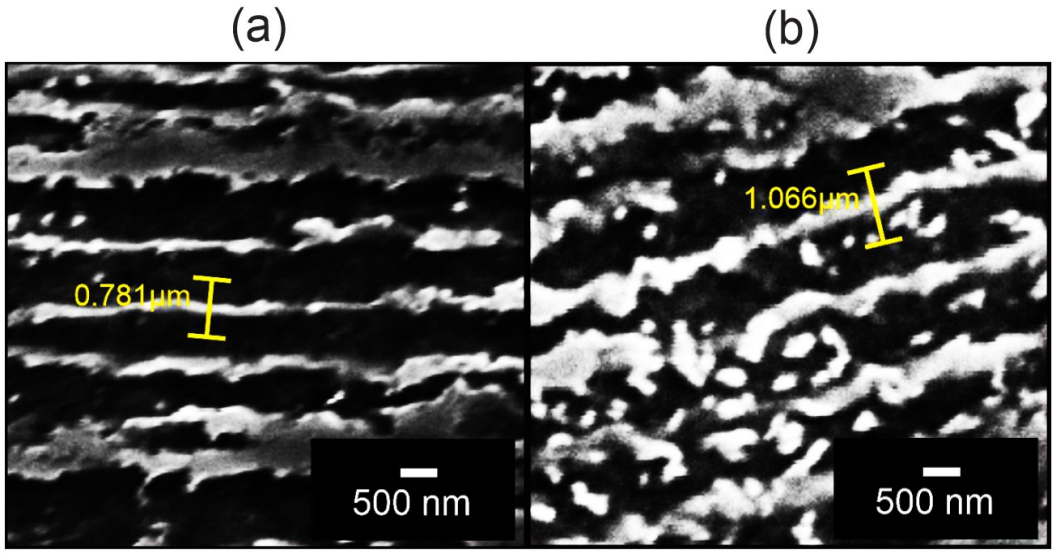

Figure 2-25 SEM micrographs of the middle region of parts fabricated by the adaptive P controller with the desired temperature of: (a) 1450 ℃ (2nd set) and (b) 1490 ℃ (1st set).

Table 2-6 The microhardness features of the samples.

Feature	Fixed laser power	Adaptive P (1490 ℃)	Adaptive P (1450 ℃)	Simple P (1490 ℃)	Simple P (1450 ℃)	Q-SMC (1490 ℃)	Q-SMC (1450 ℃)
Min microhardness (HV)	276	320	308	314	300	314	298
Max microhardness (HV)	326	344	332	345	330	350	329
Variations (HV)	50	24	24	31	30	36	31
Mean value (HV)	302.4	334	321.8	330.5	318.8	333.2	315

2.5 Conclusions

In this study, an analytical-experimental model was developed, and three different types of controllers (adaptive P, Q-SMC, and simple P) were designed to control the temperature of the melt pool by manipulating the laser power. The performance of the controllers was examined with the existing model, and it was revealed that the adaptive P controller performed better than the other controllers. Also, a monitoring system consists of a two-color pyrometer, which was calibrated previously, was utilized to establish different types of experiments on the L-PBF machine and to investigate the performance of the controllers.

To find out the correlation between the control process and uniformity of the final products, the printed samples were investigated from the microstructure and microhardness points of view. The results revealed that the thermal dynamics of the melt pool, specifically the temperature, has a great impact on the microstructural and mechanical properties uniformity of the final products. In summary, the following conclusions are derived:

1. Among the proposed controllers, the adaptive P has the fastest response to any deviations from the reference temperature, making it a suitable choice when a time-variable temperature is preferable.
2. A smaller initial error of the temperature can reduce the rise time of all controllers. Therefore, the knowledge about the initial temperature can be helpful in controlling the melt pool temperature.
3. Higher melt pool temperatures result in larger primary dendrite arm spacing (PDAS) which can be attributed to the melt pool enlargement and the reduced cooling rate.
4. The length of interval (LI) of the PDAS is shorter in the controlled cases in comparison to the case subjected to a fixed set of process parameters, especially in the middle and top regions of the samples. This results in a more uniform microstructure throughout the part. It is worthwhile to mention that when using an adaptive P controller, the bottom region of the part shows a narrow LI of the PDAS, which is close to those of the middle and top regions.
5. Implementation of a controller can narrow down the variations of the microhardness along the building direction, leading to more uniform mechanical properties.

Authors contributions:

Hossein Rezaeifar: Investigation, Methodology, Conceptualization, Writing-original draft.

Mohamed Elbestawi: Review and editing, Supervision.

2.6 References

[1] Y. L. Lo, B. Y. Liu, and H. C. Tran, "Optimized hatch space selection in double-scanning track selective laser melting process," *Int. J. Adv. Manuf. Technol.*, vol. 105, no. 7–8, pp. 2989–3006, Dec. 2019, doi: 10.1007/s00170-019-04456-w.

[2] S. K. Everton, M. Hirsch, P. I. Stavroulakis, R. K. Leach, and A. T. Clare, "Review of in-situ process monitoring and in-situ metrology for metal additive manufacturing," *Mater. Des.*, vol. 95, pp. 431–445, 2016, doi: 10.1016/j.matdes.2016.01.099.

[3] B. K. Foster, E. W. Reutzel, A. R. Nassar, C. J. Dickman, and B. T. Hall, "A brief survey of sensing for metal-based powder bed fusion additive manufacturing," *Dimens. Opt. Metrol. Insp. Pract. Appl. IV*, vol. 9489, p. 94890B, 2015, doi: 10.1117/12.2180654.

[4] Z. Y. Chua, I. H. Ahn, and S. K. Moon, "Process monitoring and inspection systems in metal additive manufacturing: Status and applications," *Int. J. Precis. Eng. Manuf. - Green Technol.*, vol. 4, no. 2, pp. 235–245, 2017, doi: 10.1007/s40684-017-0029-7.

[5] E. Fereiduni, A. Ghasemi, and M. Elbestawi, "Selective laser melting of aluminum and titanium matrix composites: Recent progress and potential applications in the aerospace industry," *Aerospace*, vol. 7, no. 6, 2020, doi: 10.3390/AEROSPACE7060077.

[6] M. Zeinali and A. Khajepour, "Height control in laser cladding using adaptive sliding mode technique: Theory and experiment," *J. Manuf. Sci. Eng. Trans. ASME*,

vol. 132, no. 4, pp. 1–10, 2010, doi: 10.1115/1.4002023.

[7] G. Mohr, S. J. Altenburg, and K. Hilgenberg, "Effects of inter layer time and build height on resulting properties of 316L stainless steel processed by laser powder bed fusion," *Addit. Manuf.*, vol. 32, no. July 2019, p. 101080, 2020, doi: 10.1016/j.addma.2020.101080.

[8] B. L. Silva, I. J. C. Araujo, W. S. Silva, P. R. Goulart, A. Garcia, and J. E. Spinelli, "Correlation between dendrite arm spacing and microhardness during unsteady-state directional solidification of Al-Ni alloys," *Philos. Mag. Lett.*, 2011, doi: 10.1080/09500839.2011.559911.

[9] M. Ş. Turhal and T. Savaşkan, "Relationships between secondary dendrite arm spacing and mechanical properties of Zn-40Ai-Cu alloys," *J. Mater. Sci.*, 2003, doi: 10.1023/A:1024434602540.

[10] J. Fox, F. Lopez, B. Lane, H. Yeung, and S. Grantham, "On the requirements for model-based thermal control of melt pool geometry in laser powder bed fusion additive manufacturing," *Mater. Sci. Technol. Conf. Exhib. 2016, MS T 2016*, vol. 1, pp. 133–140, 2016.

[11] P. Mercelis, J. P. Kruth, and J. Van Vaerenbergh, "Feedback control of selective laser melting," In *Proceedings of the 15th International Symposium on Electromachining*, pp. 421-426. UNIV NEBRASKA-LINCOLN, 2007.

[12] T. Craeghs, F. Bechmann, S. Berumen, and J. P. Kruth, "Feedback control of Layerwise Laser Melting using optical sensors," 2010, doi: 10.1016/j.phpro.2010.08.078.

[13] V. Renken, S. Albinger, G. Goch, A. Neef, and C. Emmelmann, "Development of an adaptive, self-learning control concept for an additive manufacturing process," *CIRP J. Manuf. Sci. Technol.*, 2017, doi: 10.1016/j.cirpj.2017.05.002.

[14] V. Renken, L. Lübbert, H. Blom, A. Von Freyberg, and A. Fischer, "Model assisted closed-loop control strategy for selective laser melting," *Procedia CIRP*, vol. 74, pp. 659–663, 2018, doi: 10.1016/j.procir.2018.08.053.

[15] V. Renken, A. von Freyberg, K. Schünemann, F. Pastors, and A. Fischer, "In-process closed-loop control for stabilising the melt pool temperature in selective laser melting," *Prog. Addit. Manuf.*, pp. 411–421, 2019, doi: 10.1007/s40964-019-00083-9.

[16] J. Ning, D. Sievers, H. Garmestani, and S. Liang, "Analytical Modeling of In-Process Temperature in Powder Bed Additive Manufacturing Considering Laser Power Absorption, Latent Heat, Scanning Strategy, and Powder Packing," *Materials (Basel).*, 2019, doi: 10.3390/ma12050808.

[17] J. C. Jaeger and H. S. Carslaw, *Conduction of heat in solids*. Clarendon P, 1959.

[18] T. Hägglund and K. J. Åström, "An Industrial Adaptive PID Controller," *IFAC Proc. Vol.*, vol. 23, no. 1, pp. 251–256, 1990, doi: 10.1016/s1474-6670(17)52729-9.

[19] K. El Rifai, "Nonlinearly parameterized adaptive PID control for parallel and series realizations," 2009, doi: 10.1109/ACC.2009.5159902.

[20] J. S. Augusto, "Fixed and adaptive PID control of the temperature in a laboratory oven," no. January 2010, pp. 9–11, 2010.

[21] K. J. Åström and B. Wittenmark, *Adaptive Control (2nd Edition)*. 2013.

[22] K.-B. Park, "Discrete-Time Sliding Mode Controller for Linear Time-Varying Systems with Disturbances," *Trans. Control. Autom. Syst. Eng.*, vol. 2, no. 4, pp. 244–247, 2000.

[23] G. Marchese, X. Garmendia Colera, F. Calignano, M. Lorusso, S. Biamino, P. Minetola, D. Manfredi, "Characterization and Comparison of Inconel 625 Processed by Selective Laser Melting and Laser Metal Deposition," *Adv. Eng. Mater.*, vol. 19, no. 3, Mar. 2017, doi: 10.1002/adem.201600635.

[24] C. Qiu, H. Chen, Q. Liu, S. Yue, and H. Wang, "On the solidification behaviour and cracking origin of a nickel-based superalloy during selective laser melting," *Mater. Charact.*, vol. 148, no. January, pp. 330–344, 2019, doi: 10.1016/j.matchar.2018.12.032.

[25] C. U. Brown, G. Jacob, A. Possolo, C. Beauchamp, M. Peltz, M. Stoudt, A. Donmez, "The Effects of Laser Powder Bed Fusion Process Parameters on Material Hardness and Density for Nickel Alloy 625," *NIST Adv. Manuf. Ser.*, pp. 100–119, doi: 10.6028/NIST.AMS.100-19.

Chapter 3

Porosity formation mitigation in laser powder bed fusion process using a control approach

Complete Citation:

Rezaeifar, Hossein, and Mohamed Elbestawi. "Porosity formation mitigation in laser powder bed fusion process using a control approach." *Optics & Laser Technology* 147 (2022): 107611. https://doi.org/10.1016/j.optlastec.2021.107611

Abstract

This study deals with quality control of the laser powder bed fusion (L-PBF) process using a temperature measurement approach rather than the commonly used energy density criterion. Temperature domains corresponding to the most common porosities, namely; lack of fusion (LOF), lack of penetration (LOP), and keyhole, were determined in a range of process parameters using a thermal imaging system. A safe zone was introduced by defining a lower and an upper limit based on the critical temperatures causing transitions from LOP to defect-free and from defect-free to keyhole zones, respectively. A proportional-integral-derivative (PID) controller was used to maintain the melt pool temperature within the safe zone during the L-PBF process for Inconel 625 and avoid the formation of porosities, regardless of the initial condition selected and the scanning speed employed. In all cases, a short settling time in the order of the printing time for a few layers was required to reach the steady-state condition at which defect-free parts could be obtained. The knowledge gained from this study can pave the way for the development of new temperature-based criteria considering all process variables contributing a role in the L-PBF process.

Keywords

Laser powder bed fusion, Additive manufacturing, Control of melt pool temperature, Porosity, Quality inspection.

Abbreviations

AM	Additive Manufacturing
CAD	Computer-Aided Design
EDM	Electrical Discharge Machining
FOV	Field of View
HIP	Hot Isostatic Pressing
LOF	Lack of Fusion
LOP	Lack of Penetration
L-PBF	Laser Powder Bed Fusion
LWIR	Long-Wave Infrared Camera
PID	Proportional-Integral-Derivative
PM	Partially-Melted
UM	Un-Melted

3.1 Introduction

Laser powder bed fusion (L-PBF) refers to an additive manufacturing (AM) process in which a high-intensity laser source melts powders in a layer-by-layer manner to fabricate parts based on a computer-aided design (CAD) model without almost any geometrical limitations [1–6]. The development of the L-PBF process has provided an outstanding opportunity to manufacture unique parts which are practically impossible to be produced by conventional manufacturing methods. The L-PBF process also does not require intricate build tools and assembly processes. However, internal defects such as porosities deteriorate the quality of the parts fabricated by the L-PBF process. Porosities can be formed via different mechanisms, as follows:

1. Lack of fusion (LOF): When the energy of the laser is not high enough to fully melt all the powder particles in a selected region, un-melted/partially-melted (UM/PM) particles can be observed in the final product (Figure 3-1(a)). The defects formed due to UM/PM particles are referred to as the LOF porosities. The LOF porosities are characterized by their irregular shape and large size [7–10].
2. Lack of penetration (LOP): The LOP is defined as inadequate penetration of the melt pool of a currently depositing track into the previously consolidated layer or the adjacent track. The porosities formed by this mechanism have been presented in Figure 3-1(b), in which two adjacent tracks were not completely bonded together. This type of porosity originates from the rapid solidification rate and high viscosity of the molten material at a lower temperature [11–13]. As shown in Figure 3-1(b), despite the porosities caused by LOF, the LOP porosities are free from UM/PM powder particles. In addition, according to the literature [14], the consolidation process of powder bed fusion has two stages. First, powder melting,

in which the powder particles fusion occurs and second, melt reshaping, which consists of the flow of the molten material. Unlike LOF, the LOP forms during the melt reshaping step. Therefore, the mechanism of LOP formation differs from LOF formation as well.

3. Gas porosity: Powder particles may have some internal holes filled by gas due to the powder production process. The gas can be released and trapped inside the part during the L-PBF process, leading to the formation of tiny spherical porosities (Figure 3-1(c)), called gas porosities. The entrapment of shielding gas and vaporized elements of the alloy can also produce gas porosity [15–17].
4. Keyhole porosity: Another source for the formation of spherical/semi-spherical porosities in AM of metallic materials is the keyhole effect, taking place at high energy densities. Under this condition, the evaporation of the molten material causes the formation of a slender vapor cavity (known as keyhole), which is filled with high-temperature metallic vapor or plasma. Instability, as well as repeated formation and collapse of these keyholes, results in the generation of gas bubbles in the melt pool, which may lead to the coarse spherical porosities in the final part if captured by the solidification interface (Figure 3-1(d) [15, 17, 18]).

Du Plessis et al. [19] and Liu et al. [20] showed that among the abovementioned defects, LOF, LOP, and keyhole porosities have a higher adverse impact on the mechanical properties of the parts compared to the gas porosities. In addition, these porosities are hard to remove even via post-processing methods such as hot isostatic pressing (HIP), especially if they occur near the surfaces of the part [21].

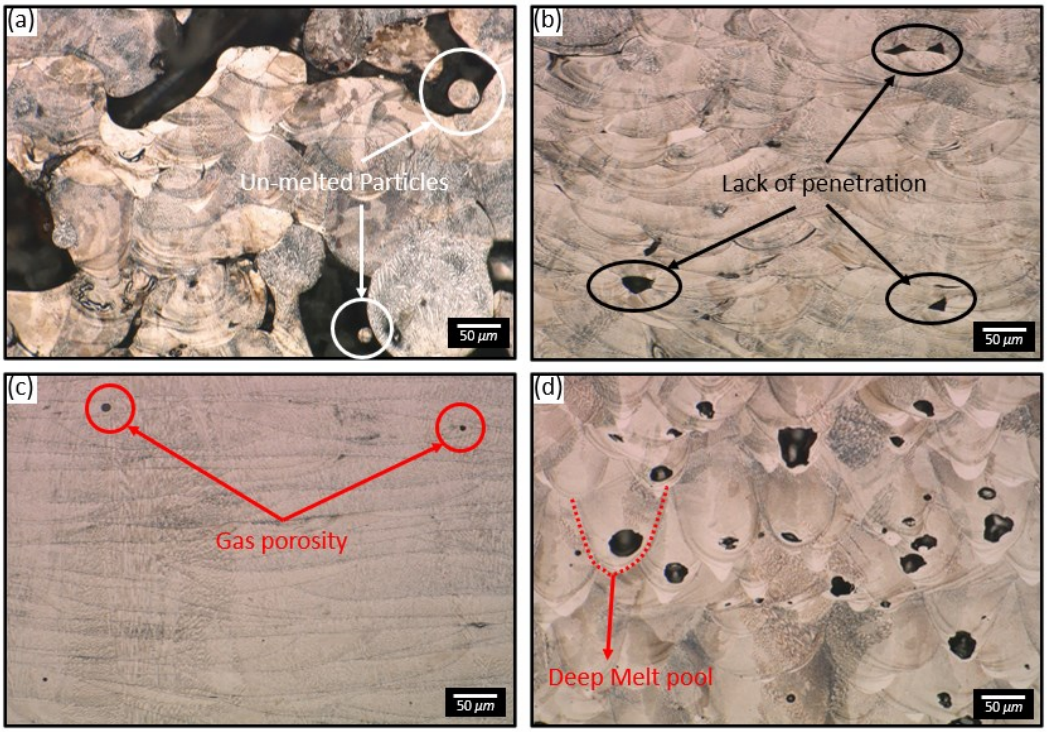

Figure 3-1 Types of porosities formed during the L-PBF processing of Inconel 625: (a) LOF porosity, with UM particles shown inside the circles, (b) LOP, with irregular porosities free from UM/PM particles, (c) gas porosity, and (d) keyhole porosity.

Several studies have been implemented during the past decade to find the correlation between energy density and different porosities [22–24]. For example, Peng and Chen [24] introduced a model to find the correlation between the energy density and the porosity level in a low energy density regime. However, the model is applicable only within a limited range of process conditions. Although the energy density (E_v) equation (Eq. (1) [25]) considers the effect of some of the process parameters such as laser power (P), scanning speed (v), hatch spacing (h), and layer thickness (t), it fails to take the influence of other variables (e.g., beam diameter, gas flow, building direction, and scanning pattern) into account, which also play essential roles in porosity formation [26–29]. For instance, Sow et al. [28] showed that the beam diameter alters the melting mode, while other process

parameters remained constant. Since the consideration of all relevant variables in a single equation is not practical, another approach in which all the process variables are involved needs to be applied to explore the defect formation mechanisms. Accordingly, an on-line investigation of the process is required to gain a better insight into porosity formation.

$$E_v = \frac{P}{v \times h \times t} \tag{3-1}$$

Bartlett et al. [30] mounted a long-wave infrared camera (LWIR) off-axially to detect the LOF and keyhole porosities directly. They utilized a thermal image in each layer to provide a suitable temperature distribution map of the corresponding layer to recognize the LOF. The results, which were compared with SEM images, showed that although the method can detect the LOF with an accuracy of 85%, it is not adequate for detecting keyhole porosity. The requirements of such monitoring approaches are high-resolution and high-speed sensors, which are rather costly. Coeck et al. [31] used a monitoring system consisting of two photodiodes to investigate the LOF porosities. They reported that the system is capable of detecting porosities having a diameter of 160 μm or higher with 90% accuracy. However, it should be noted that the keyhole porosities can also cause critical issues, especially at the edges of the L-PBF fabricated parts, which was not considered in this study. Forien et al. [32] showed that keyhole porosities could be predicted by signals received by a pyrometer, representing the temperature of the melt pool. The outcomes of this study indicated that from a specific threshold, the probability of keyhole porosity formation would increase by increasing the temperature signal values. In all studies mentioned above, the target was detecting a specific type of porosity, and there was no attempt to avoid such defects.

As mentioned before, keyhole porosities can be correlated to the intensity of the melt pool radiation captured by a thermal sensor. Additionally, according to [33], the intensity of the melt pool radiation is proportional to the melt pool dimensions; thus, LOF and LOP porosities which form when the size of the melt pool is relatively small to provide sufficient inter-track overlap, can be correlated to the temperature signals. As a result, the likelihood of porosity formation can be monitored by a thermal sensor. Accordingly, temperature ranges corresponding to these defects can be discovered via temperature measurements, and consequently, a safe range of thermal signals can be determined to produce defect-free parts. The porosity level can be mitigated by keeping the temperature in the safe range. As discussed in [34], control approaches are feasible to keep the temperature of the melt pool close to a specific temperature.

This research study proposes a proportional-integral-derivative (PID) controller to keep the melt pool temperature of Inconel 625 superalloy during the L-PBF process in a safe zone by manipulating the laser power layer by layer. For this purpose, a monitoring system capable of capturing the thermal signals is first designed to send the thermal measurements of each layer to the controller. Then, a set of experiments is utilized to detect the safe zone using the described sensor. Finally, the controller system is experimentally implemented on the L-PBF machine to modify the laser power between two consecutive layers if essential. The performance of the controller is examined for three different scenarios and the porosity level of the fabricated parts is investigated. The information gained from the micrographs reinforces the idea that applying an appropriate control system not only improves the quality of the part at different initial conditions and scanning speeds but also makes the fabrication of defect-free parts more time-and-cost effective.

3.2 Materials and Methods

3.2.1 Fabrication procedure

The L-PBF machine employed in this study is an OmniSint-160 with a 400 W Yb-fiber laser having wavelength of 1090 nm, and a spot size of 100 μm. This machine has the capability of on-line laser power manipulation between two consecutive layers. The process chamber was filled with high-purity Ar gas to protect the melting area. The stripe rotation strategy (67 degrees) was utilized as a scanning pattern to prevent excessive heat accumulation [35], and to produce successive layers overlapping each other [15] (Figure 3-2). The hatch spacing and nominal powder layer thickness (platform displacement) in all parts were 100 and 30 μm, respectively. It should be mentioned that experiments were implemented on a small AISI 304 stainless steel disk with a diameter of 50.8 mm that can be located on top of the original build plate (Figure 3-3). The material used in the study was gas atomized Inconel 625 powder, supplied by Carpenter Additive Inc, with a particle size in the range of 15-45 μm, and the nominal chemical composition listed in Table 3-1.

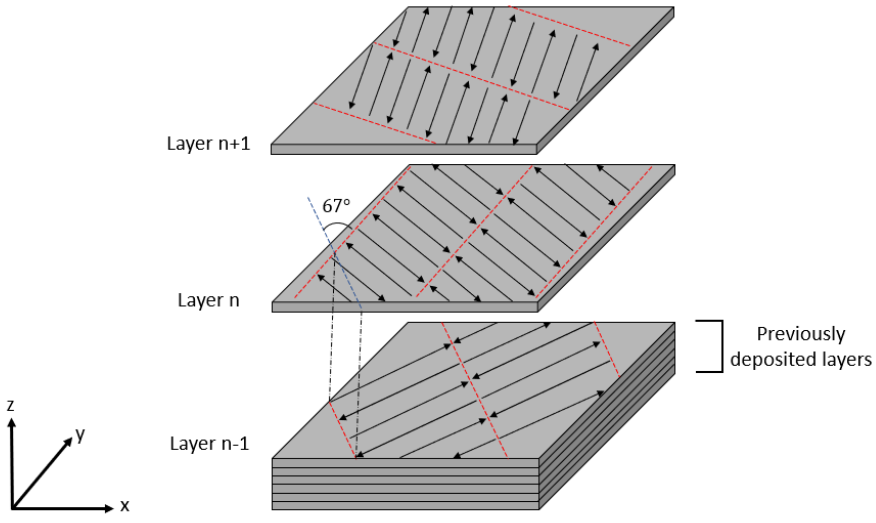

Figure 3-2 Schematic view of the stripe rotation strategy (67 degrees) used in this study.

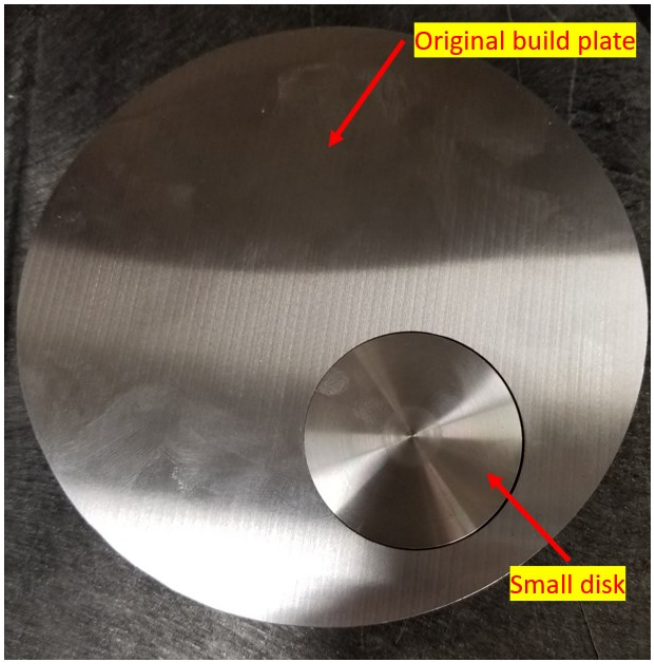

Figure 3-3 The modified build plate in which a small disk is located inside the original build plate. The samples were printed on the small disk.

Table 3-1 The nominal chemical composition of the Inconel 625 used in this study (Result indicates the percentage of weight tested for the used powder).

Element	Al	C	Co	Cr	Cu	Fe	Mo	Mn	Nb+Ta	Ni	P	S	Si	Ti
Min (wt%)	-	-	-	20.0	-	-	8.0	-	3.15	Bal	-	-	-	-
Max (wt%)	0.4	0.1	1.0	23.0	0.5	5.0	10.0	0.5	4.15	Bal	0.015	0.015	0.5	0.4
Result	0.11	0.02	0.02	22.0	<0.1	0.3	9.0	<0.01	3.80	Bal	<0.001	0.001	0.07	0.11

3.2.2 Temperature measurement

Figure 3-4(a) shows the infrared thermal measurement system mounted on the process chamber of the L-PBF machine. An infrared thermal camera (Optris PI 08M) operating at 1 kHz acquisition frequency and a collection wavelength of 800 nm was used to capture thermal signals. The camera was mounted off-axially on the process chamber with a viewing angle of approximately 60º to the powder bed (Figure 3-4(b)) using a polymer 3D printed mounting fixture, and its field of view (FOV) covered the whole build surface (small disk). Using this configuration, the pixel size is 80 μm. A sapphire window transmitting wavelengths in a range of 600-1050 nm was placed in front of the camera to prevent the laser wavelength and allow suitable wavelengths to pass through. The apparent temperature was used in this study instead of the true temperature because of two main reasons: (i) detecting the defect signals requires only relative changes in the output of the thermal sensor that correlate with different process windows [32] and (ii) only constant emissivity can be used on the camera, and this assumption produces huge errors since emissivity depends on the viewing angle, wavelength, and temperature which aggravates the temperature measurement [36, 37]. Therefore, the emissivity was considered equal to 1, making the measurements proportional to the absolute irradiance intensity of the object. It is worthwhile to mention that a specific configuration was set on the camera during the measurement to ensure that the readings correspond to the pixel with the highest temperature value. In this way, the results were not affected by random events such as spatters. All measurements were accomplished through a LabView virtual instrument.

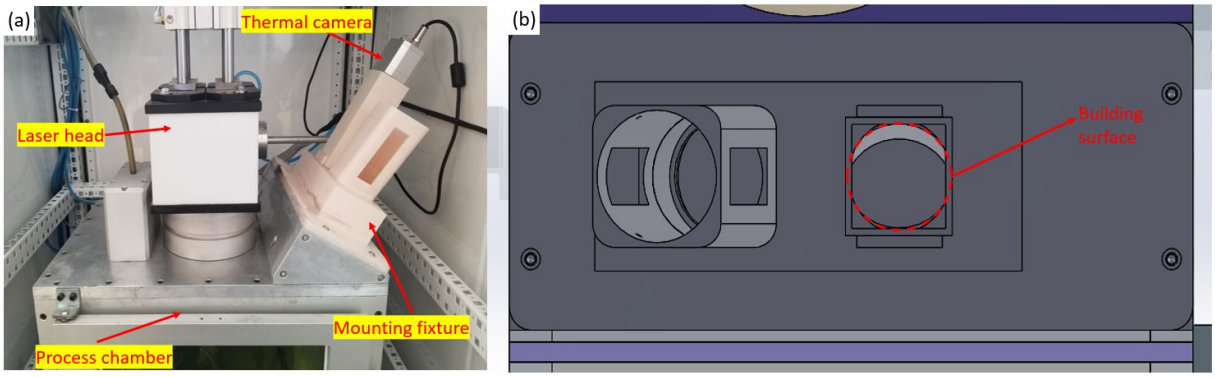

Figure 3-4. Monitoring system: (a) the thermal camera mounted with a viewing angle of approximately 60º to the powder bed, and (b) the FOV of the camera covering the whole building surface.

3.2.3 Influence of the temperature on porosity

As mentioned, among different kinds of porosities, LOF, LOP, and keyhole deteriorate the quality of the part drastically [19, 20, 38]. The LOF porosity occurs when the melt pool area is not large enough to bond adjacent tracks [7–10]; thus, the size of the melt pool plays a critical role in this type of porosity. Mercelis et al. [33] showed that the intensity of the melt pool radiation has a proportional relationship with the melt pool area; thus, the LOF porosity is correlated to the temperature of the melt pool.

The LOP porosity occurs when the viscosity of the molten material is not low enough to make it flow within the gaps quickly [11–13]. The reason behind the high viscosity is the low temperature of the melt pool [39, 40], meaning that the LOP porosity is also related to the temperature of the melt pool.

Finally, deep melt pools are created at extremely high temperatures due to a significant amount of energy transferred from the laser beam to the powder particles. Also, some parts of the material evaporate and trap inside the deep melt pool, forming keyhole porosity [17,

18, 41]. Accordingly, the keyhole porosity also can be correlated to the temperature of the melt pool.

3.2.4 Safe zone Identification

Based on section 3.2.3, LOF, LOP, and keyhole porosities can be correlated to the temperature of the melt pool. Therefore, a safe zone can be defined in which highly dense parts can be obtained by detecting the temperature signals corresponding to each defect. In this study, various process parameters were utilized to print defect-free parts as well as parts with different defect types. Temperature measurements corresponding to each part were also performed during the printing process. Based on the results, deviations from the defect-free condition were identified as abnormalities. From a specific laser power, keyhole porosity appeared in the printed samples. The acquired signals in these samples were considered as signals by which the formation of this type of porosity is probable. Since keyhole porosities can be formed at higher temperatures, these signals were considered as upper band signals, the minimum of which was named the upper limit of the safe zone. In other words, defective samples having keyhole porosities can be obtained if the measured temperature exceeds the upper limit of the safe zone (upper band signal). Besides, the signals corresponding to parts with the LOP porosity were considered lower band signals, and the maximum of the measurements was called the lower limit of the safe zone. Likewise, the lower band was located below the lower limit of the safe zone, where the formation of the defective parts having LOP porosities is probable. It is worth mentioning that the LOF porosity would form at a lower temperature than that of the LOP porosity, so the measurements related to this type of porosity are located at the lower band. Therefore, the temperature signals corresponding to the LOF porosity do not affect the safe zone. Figure 3-5 schematically illustrates these bands and the safe zone. According to the

temperature dependency of the defects, the porosity level is mitigated by keeping the signals inside the safe zone.

3.2.5 Control strategy

Corrective action is necessary when the measured temperature exceeds the upper limit or drops below the lower limit to keep the temperature inside the safe zone. For this purpose, an automatic approach should be deployed since the manual modification of the process parameters needs a user to check the monitoring results during the process. The block diagram of the control system is presented in Figure 3-6. The reference temperature was set to be at the center of the safe zone. The laser power was manipulated between two consecutive layers while the measurements were taken for the whole layer (an array of signals ($\bar{T}_s$) was captured by the thermal camera during each layer). Therefore, these signals were required to be analyzed before the computation of the error. The Feedback Element

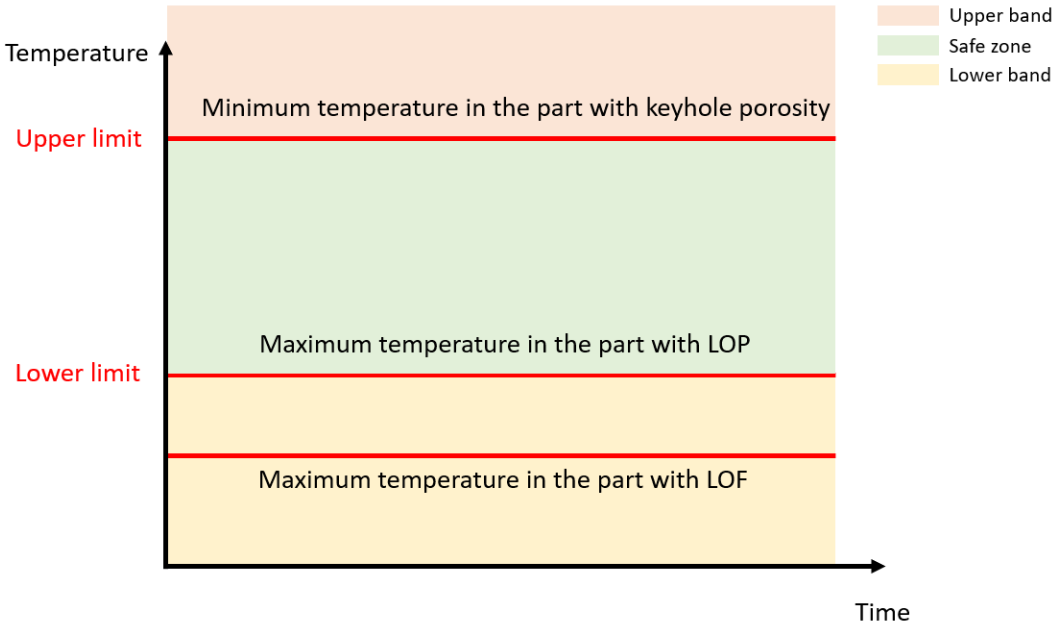

Figure 3-5 Schematic illustration of the upper band, lower band, and safe zone.

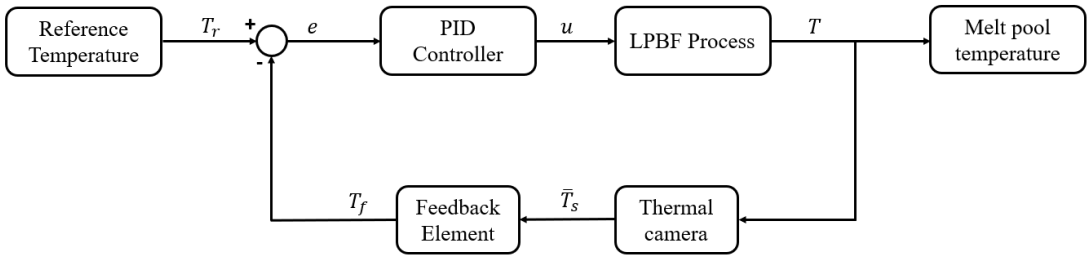

Figure 3-6 Block diagram of the PID control system.

inside the loop was in charge of the signal analysis and contained the following equation:

$$T_f = \begin{cases} T_{max} & T_{max} > upper\ limit, \\ T_{min} & T_{min} < lower\ limit, \\ T_r & otherwise. \end{cases} \quad (3\text{-}2)$$

where T_f, T_r, T_{max}, and T_{min} are the feedback signal, reference temperature, maximum signal in measurements, and minimum signal in measurements, respectively. According to Eq. (3-2), using the Feedback Element block, the signals within the safe zone were considered as suitable signals, and the controller was switched off in this condition. On the other hand, the maximum error was calculated when the signals were out of the safe zone.

Because the criterion of the defective part is the difference between the temperature signals of the molten material and the thresholds of the safe zone, a PID controller was used to compute the needed adjustment in laser power to maintain the temperature inside the defect-free region. The PID control law continuously updated the laser power, based on the proportional, integral, and derivative of the error term e, estimated from the on-line measurement. e is defined as the difference between the desired and the actual measurements. Then, the updated laser power was fed into the L-PBF machine for printing the next layer. In this study, the P, I, and D gains were obtained using the trial and error

approach during some pre-experiments. The P, I and D gains in the designed controller were 0.015, 0.005, and 0.02, respectively. Figure 3-7 presents the architecture of the control approach in this study. First, the machine starts to print a layer by defining the process parameters. After the fabrication of a layer and temperature measurements are accomplished, the controller checks whether or not the printed layer was the last one. For any given layer before the last one based on the abovementioned control system, if the maximum temperature exceeds the upper limit or the minimum temperature drops below the lower limit, the controller changes the laser power for the next layer; otherwise, the process parameters will not change. This loop repeats until the last layer of the part is printed. It is worth mentioning that the control system was implemented in a LabView vi.

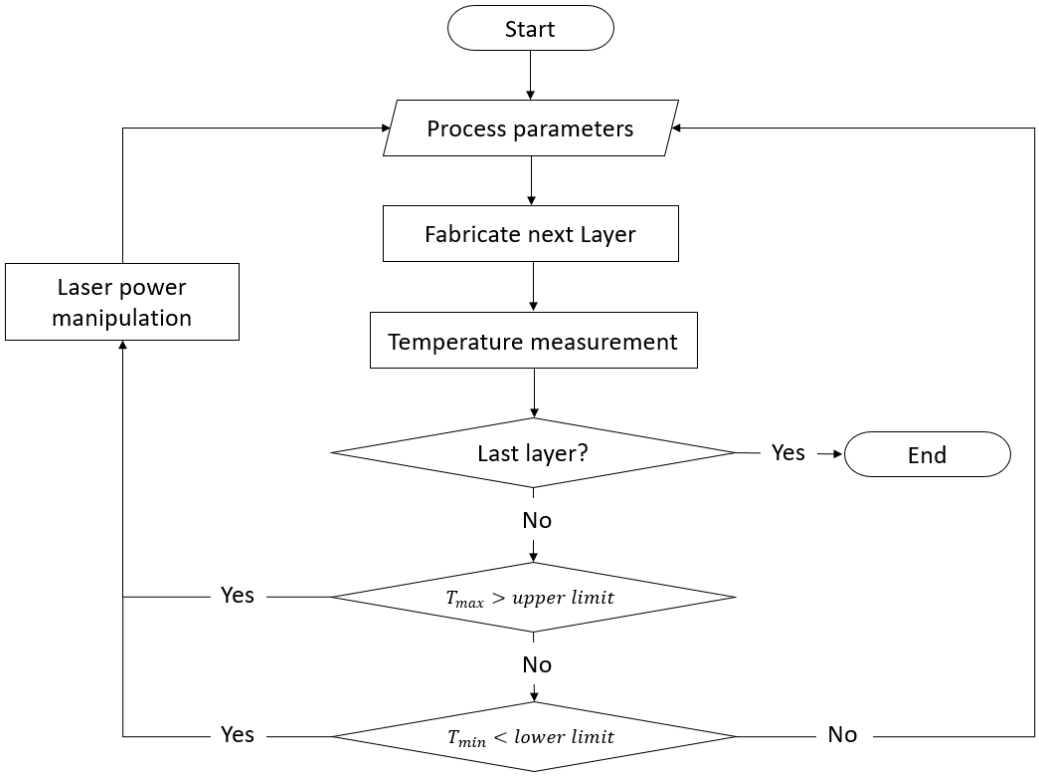

Figure 3-7 The architecture of the process using the control system.

3.2.6 Metallography

The fabricated samples were removed by EDM from the disk and sectioned along the building direction using a precision cutter to investigate the quality of parts. The samples were mounted in phenolic thermosetting resin and then ground with sequentially finer SiC grinding papers. The polishing was performed using 9, 3, and 1 μm diamond suspensions, respectively. For porosity examination, mixed acid etchant with the following chemical composition was used: 75 ml HCl and 25 ml HNO_3. Imaging of the porosity was conducted by a Keyence VHX-5000 digital microscope.

3.3 Results and discussion

In this section, experimental tests are presented in three steps. First, the energy density is evaluated as a metric for defect-free part production. Then, the safe zone detection is performed. Finally, the proposed control approach is examined experimentally.

3.3.1 Relation between energy density and part quality

As discussed, energy density is usually considered as a metric for finding the optimum processing condition. In this section, two sets of experiments were performed. Two cubic parts were printed in each set with the same energy density but different laser powers and scanning speeds. The parts in the first set were labeled as parts (I) and (II) with an energy density of 183.33 J/mm^3. Part (I) was printed with a scanning speed of 150 mm/s and a laser power of 82.5 W. The scanning speed and laser power for part (II) were doubled. The second set contained parts (III) and (IV) with an energy density of 161.11 J/mm^3. Part (III) had a scanning speed and a laser power of 150 mm/s and 72.5 W, respectively. Part (IV) was fabricated with a scanning speed of 300 mm/s and a laser power of 145 W. Figure 3-8 compares the quality of parts (I) and (II), where part (I) was almost fully dense

with a relative density of 99.99%, and part (II) had a relative density of 98.58% with keyhole porosities in the whole part. Accordingly, parts fabricated by the L-PBF process can have different qualities and relative densities even when subjected to the same energy densities but different combinations of laser power and scanning speed. Figure 3-9 presents the discrepancy between the quality of the parts fabricated with the same energy density in the second set. As can be seen, part (III) contains LOP while part (IV) has keyhole porosities. Therefore, two parts with the same energy density can have even different defect types formed by different mechanisms. Based on the abovementioned discussion, we conclude that the energy density value is not a reliable index to determine the quality of the parts. This makes it necessary to implement temperature-related criteria, which would be explained in the following section.

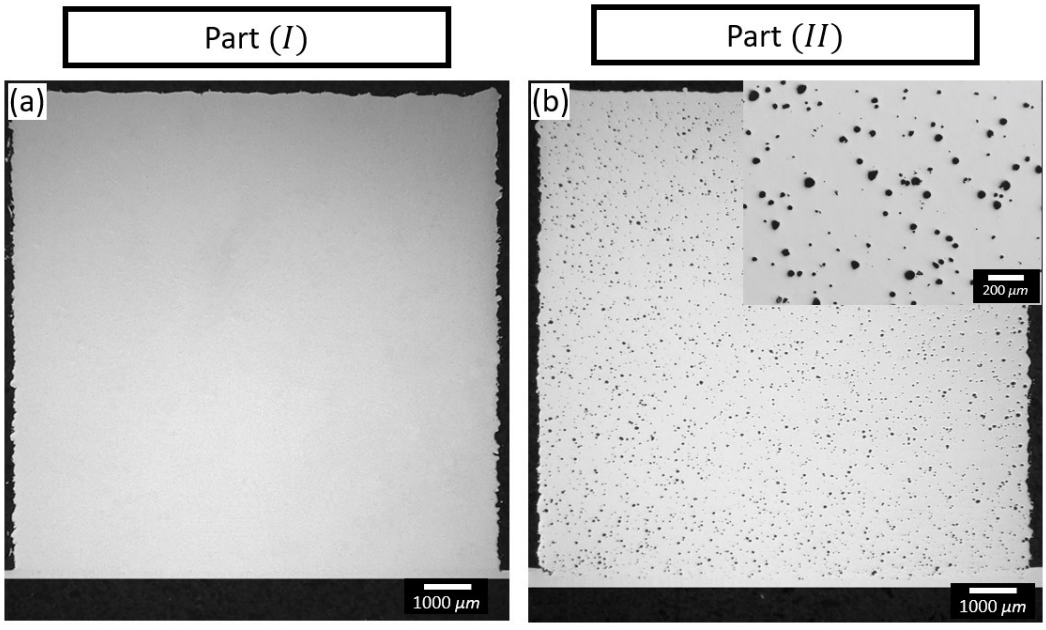

Figure 3-8 (a) Part (I) ($P = 82.5\ W$ and $V = 150\ mm/s$) and part (II) ($P = 165\ W$ and $V = 300\ mm/s$) were printed with the same energy density of $183.33\ J/mm^3$.

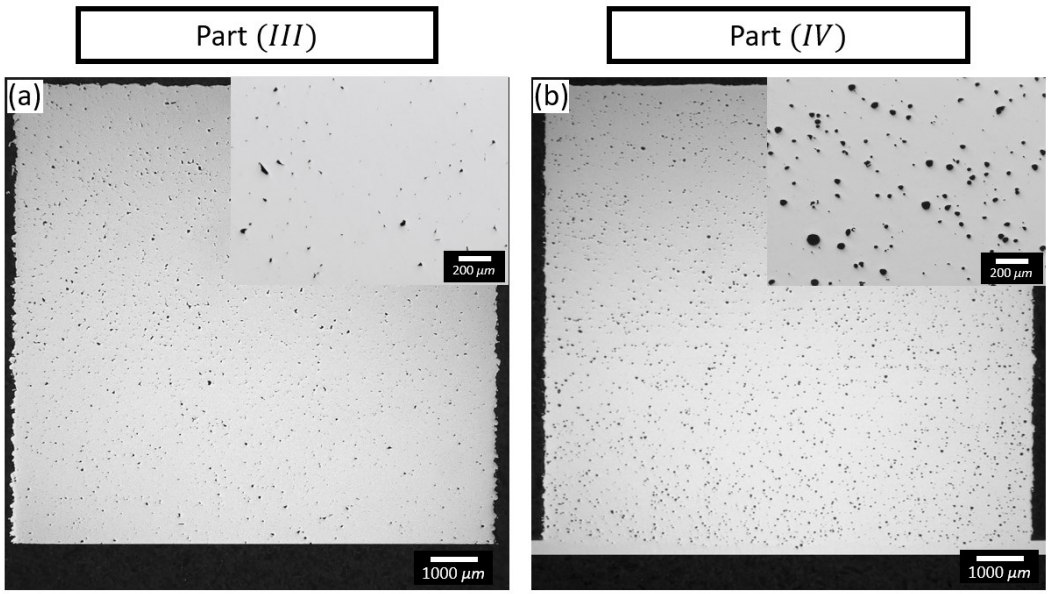

Figure 3-9 Part (III) ($P = 72.5\ W$ and $V = 150\ mm/s$) and part (IV) ($P = 145\ W$ and $V = 300\ mm/s$) were printed with the same energy density of $161.11\ J/mm^3$.

3.3.2 Safe zone detection

As discussed in section 3.2.3, LOF, LOP, and keyhole porosities are related to the melt pool temperature. Also, a safe zone can be defined based on the temperature measurements corresponding to each defect. In this section, fifteen cubic parts with dimensions of $10\ mm \times 10\ mm \times 10\ mm$ were printed with a fixed scanning speed of $150\ mm/s$, while the laser power varied from 60 to 95 W with a step size of 2.5 W to obtain various features. In addition, the melt pool temperature measurements were carried out to investigate the relationship between the measurements and the quality of the parts. Table 3-2 shows the process parameters and the relative density corresponding to each sample. Figure 3-10 displays the quality of samples 4-12. Samples 7-10 are almost defect-free, containing only a low content of tiny gas pores. Some small keyhole porosities emerged in sample 11, which are shown in Figure 3-10(a). The quantity and size of the keyhole porosities increased in sample 12. This observation indicates that samples with laser powers equal or

higher than that of sample 11 contain this type of porosity. On the other hand, samples 5 and 6 had LOP (Figure 3-10(b)), while samples 1-4 contained LOF porosities (Figure 3-10(c)). Since sample 7 was free from any LOP porosities, samples with laser powers equal or lower than that of sample 6 contain LOF/LOP porosities.

Table 3-2 The process parameters and relative densities of the parts fabricated in this study.

Sample number	Laser power (P)	Scanning speed (mm/s)	Layer thickness (μm)	Hatch spacing (μm)	Relative density (%)
1	60	150	30	100	92.58
2	62.5				95.61
3	65				96.82
4	67.5				97.04
5	70				98.08
6	72.5				99.48
7	75				99.96
8	77.5				99.98
9	80				99.99
10	82.5				99.99
11	85				99.77
12	87.5				99.49
13	90				98.71
14	92.5				97.78
15	95				97.26

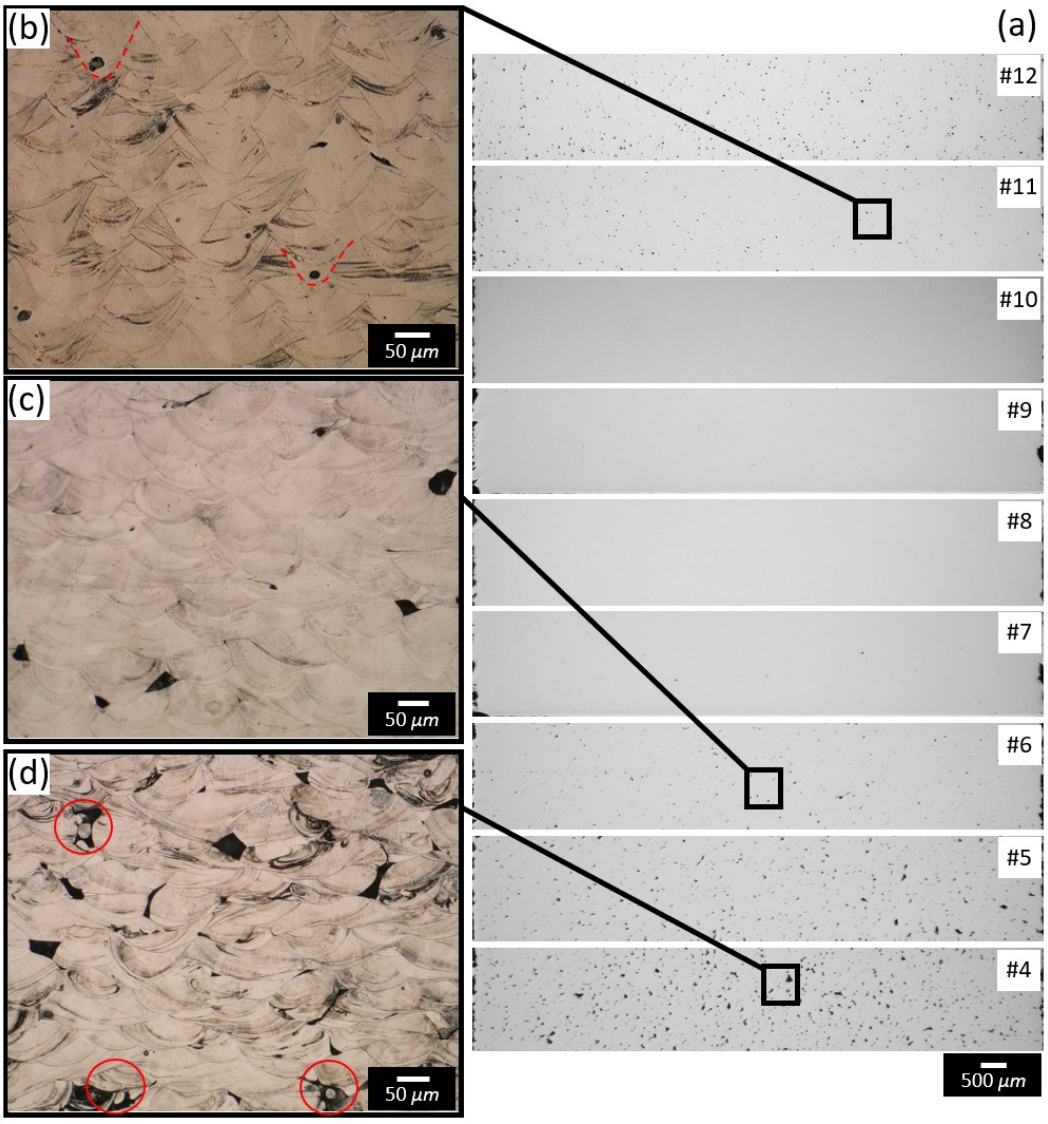

Figure 3-10 (a) Non-etched optical micrographs of samples 4-12. Higher magnification micrographs of etched cross-sections of samples 11, 6, and 4 showing keyhole, LOP, and LOF porosities in (b), (c), and (d), respectively.

Based on the aforementioned discussion, determining the upper and lower limits in Figure 3-5 is feasible by performing the melt pool temperature measurements during the printing of different samples. Figure 3-11 was constructed to determine the safe zone. In this figure, each curve represents the temperature measurement of a single layer with maximum or

minimum apparent temperature corresponding to the sample mentioned in the legend. The measurements of the layer with minimum apparent temperature in sample 11 (red line) and the measurements of the layer with maximum apparent temperature in sample 10 (green line) overlap each other. Also, this behavior can be seen by investigating the curves corresponding to sample 6 and 7. Such observation can be explained by the fact that some areas have no defects in samples 6 and 11. This is in line with the signal overlap observations between the defect-free and defective cases reported in [32].

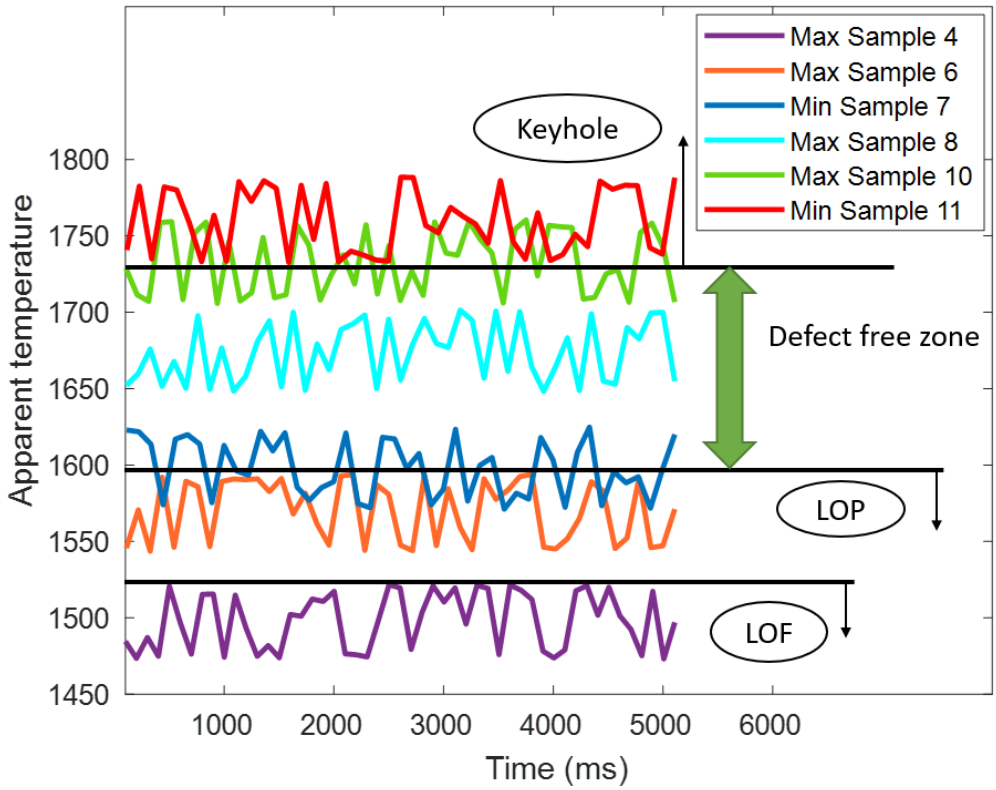

Figure 3-11 Temperature measurements during printing of different samples. The defect-free zone is detected based on the maximum values captured in sample 6 and the minimum measurements in sample 11.

The temperature signals above the minimum measurement in sample 11 can be related to keyhole porosity, meaning that this margin is the upper band of the safe zone. With the same logic, the maximum measurement in sample 6 is the lower band of the safe zone below which LOP porosity formation is probable. The upper limit from the measurements was 1732.623, and the lower limit was 1593.936. This information was used in the control system to keep the temperature in the safe zone, which will be discussed in the next section. The reference temperature for the controller was considered at the center of the safe zone, which was 1663.28. It is worth mentioning that the temperature signal below the maximum measurements in sample 4 (1522.692), the LOF porosity is probable.

3.3.3 Controller performance

As mentioned in section 3.2.5, a PID controller was employed to adjust and keep the temperature of the melt pool within the safe zone during the process. In this section, three sets of experiments were implemented with different scenarios to test the performance of the controller. In the first set, ten initial layers were printed with the laser power of 100 W and the scanning speed of 150 mm/s. Then, the controller was switched on to manipulate the laser power for the following 100 layers. The reason behind printing the initial layers with a fixed laser power was to reveal the speed and the functionality of the controller. Figure 3-12 shows the quality of the part fabricated in the first set. As it is shown, the initial layers are full of keyhole porosities. As the controller came into action, the size of the porosities became smaller, and their concentration became lower until the porosities have completely vanished. Figure 3-13 shows the temperature signals and the controller outputs after the controller was switched on. After 12 layers, the process reached a steady condition. As it is presented inside the green circles, if the temperature exceeds the upper limit, the controller reacts and adjusts the laser power to maintain the quality of the part.

The red rectangle in Figure 3-12 shows the transition zone of the process. The porosity level became lower in the building direction during this period. It is worth noting that defect-free areas started from some layers before the end of the transition zone. This phenomenon is explained by two main reasons: (i) it shows the overlap between the signals, which was discussed in section 3.3.2, and (ii) the laser fused not only the powder layer but also the consolidated layer(s) below at the end of the transition zone.

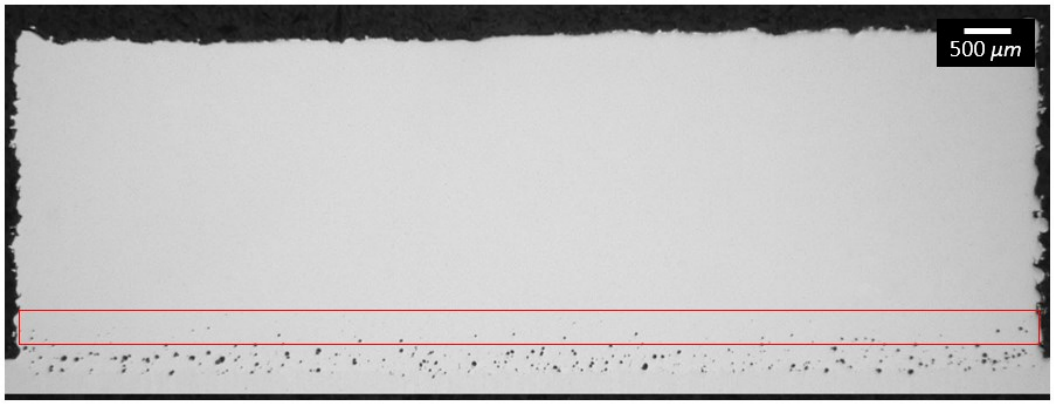

Figure 3-12 The sample fabricated during the first set of experiments. The red rectangle corresponds to the settling time.

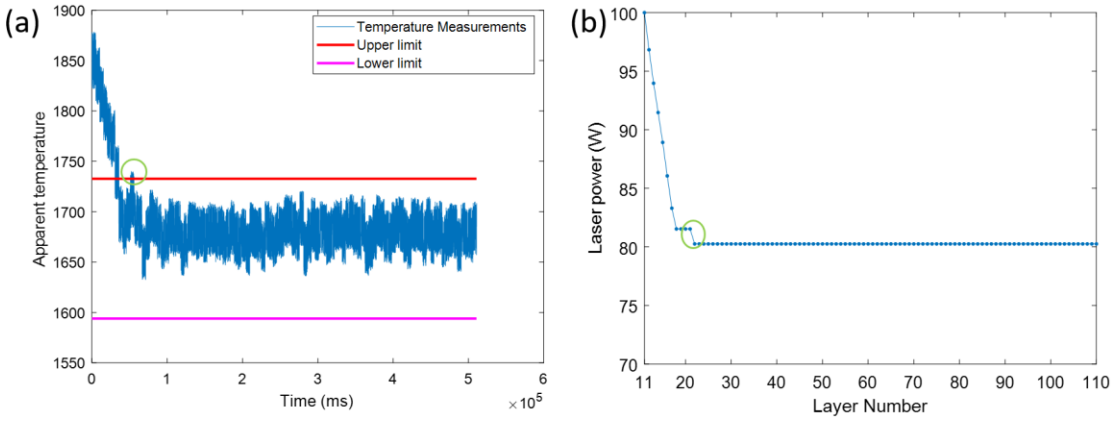

Figure 3-13 (a) Temperature measurements during the control process of the first set of experiments, and (b) the output of the controller. The green circles show that the controller responded to any deviations from the safe zone.

The second set of experiments was carried out with the initial laser power of 68 W and the scanning speed of 150 mm/s, producing a part with the LOP porosities. Similar to the first set, after ten layers, the controller was turned on to show its effect. The resulted part is shown in Figure 3-14, where the LOP porosities at the bottom are reduced in the building direction. The transition zone is smaller compared to the first set of experiments, proving a shorter settling time in this case. As shown in Figure 3-15, the safe zone became perceptible after 9 layers. The described sets of experiments indicate that the controller is capable of improving the part quality at different initial conditions.

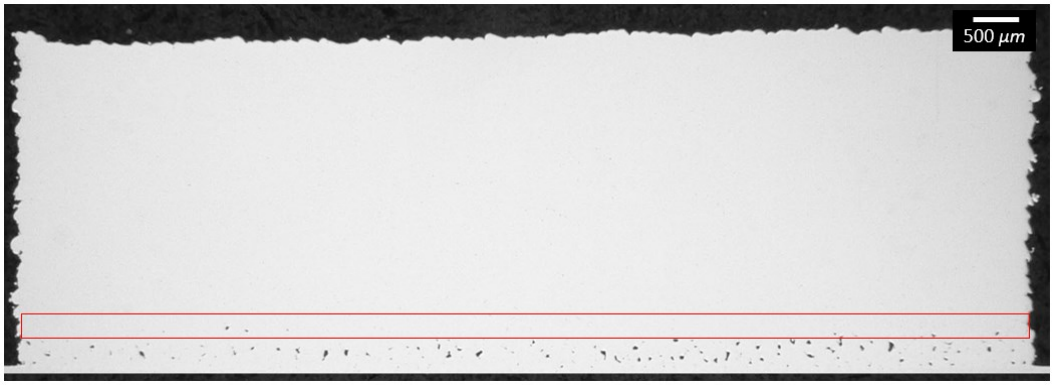

Figure 3-14 The sample fabricated during the second set of experiments. The red rectangle corresponds to the settling time.

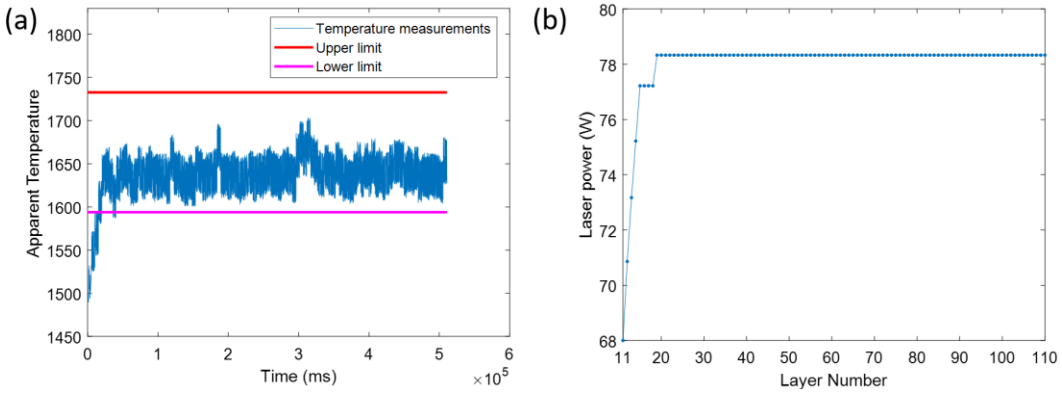

Figure 3-15 (a) Temperature measurements during the control process of the second set of experiments, and (b) the output of the controller.

The third set of experiments was designed to examine the controller performance at different scanning speeds. The initial laser power was set at 145 W, and the scanning speed at 300 mm/s since these process parameters yielded keyhole porosities (Figure 3-9(b)). The fabricated part is shown in Figure 3-16. As observed, the controller can adjust the laser power to eliminate the porosities. Also, Figure 3-17 shows that the temperatures were successfully inside the safe zone, resulting in a defect-free section at the top layers. Therefore, regardless of the scanning speed, the controller performed well and enhanced the L-PBF product quality.

In general, the results showed that controlling the temperature using a PID controller is a cost-and-time effective approach in which all the process parameters which were not included in the energy density equation are considered, making the method superior to the energy density approach. Besides, this technique enhances the quality of the part in a few layers regardless of the initially employed process parameters, which makes it applicable to different conditions. It should be emphasized that although this approach may not heal the current defects, it mitigates the porosity formation and prevents the part from failure.

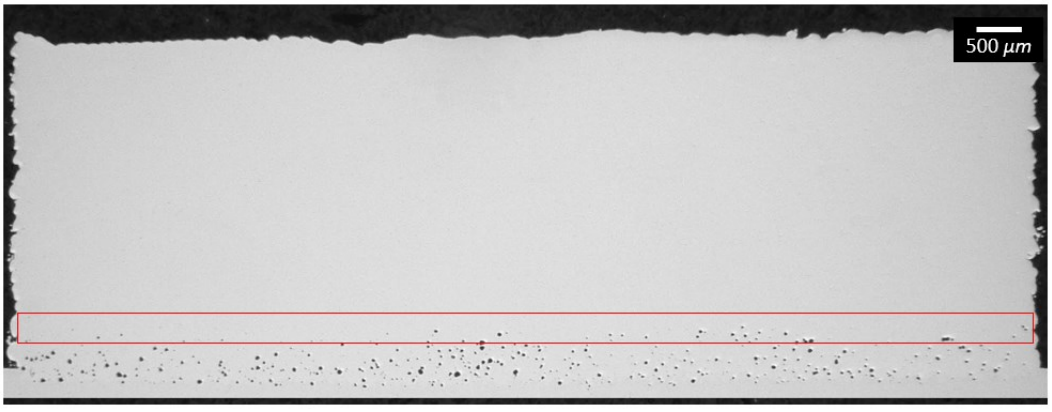

Figure 3-16 The sample fabricated during the third set of experiments. The red rectangle is corresponding to the settling time.

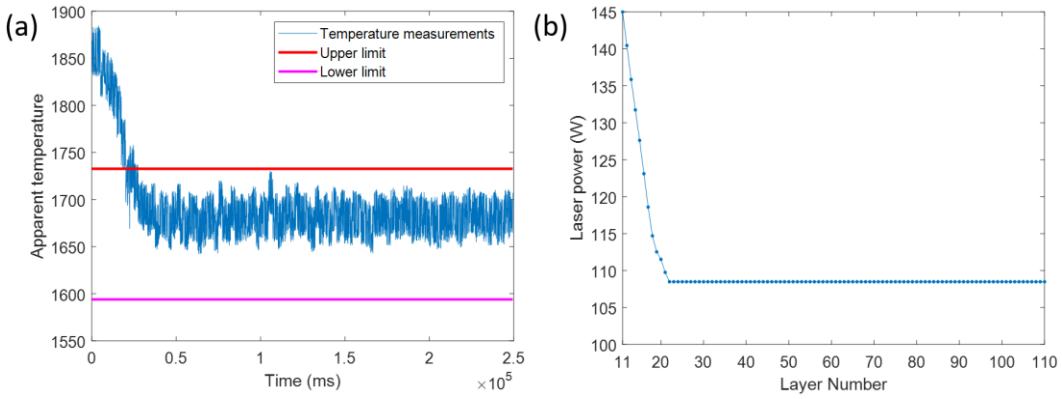

Figure 3-17 (a) Temperature measurements during the control process of the third set of experiments, and (b) the output of the controller.

To correct the occurred porosity and the process parameters for the following layers simultaneously, the combination of the control approach with suitable on-line corrective actions (such as remelting for a specific case) is worth further investigation.

Apart from the point mentioned above, it is expected that the approach presented in this study can also be applied to complex geometries and high parts since 1) the porosities discussed are all correlated to the temperature, therefore even with the complex geometries, these defects form with the same thermal situation and 2) it is shown that the controller designed in this study reacts efficiently to keep the temperature inside the safe zone. However, it should also be investigated in the future.

3.4 Conclusion

In this study, the effect of the energy density on the quality of parts fabricated by the L-PBF process was examined. Three types of porosities (lack of fusion, lack of penetration, and keyhole) were investigated. A monitoring system consisting of a thermal camera and an IR-transmissive window was utilized to find the correlation between each type of porosity and thermal measurements. Based on the measurement results, a safe zone was

introduced, and a PID controller was used to keep the thermal signals within the safe zone during the process. The performance of the controller was evaluated in three different scenarios. The results indicate that melt pool temperature control has a significant impact on part quality. In summary, the following conclusions can be drawn:

1. Energy density is not a suitable criterion to predict the densification level and defect type of the L-PBF fabricated parts because it only involves a limited number of process parameters, while several other factors can alter the quality of printed parts during the process. It was shown that two parts can have different qualities with the same energy density and even can contain various types of defects under such conditions. Therefore, an on-line investigation and control of the process features are required to result in a high-quality part.
2. Temperature ranges corresponding to each type of porosity are identified through temperature measurements. This classification helps to identify a temperature range that is free from any defect. By keeping the temperature within this range using manipulation of the laser power, the quality of the part can be significantly enhanced.
3. The control approach utilized in this study is applicable for different initial conditions and at different scanning speeds.

Although the performance of the control approach was examined in this study for elevating the quality of the Inconel 625 parts fabricated by the L-PBF process, the combination of the control approach with on-line corrective actions can be studied for other materials and different geometries in the future. In this case, in addition to changing the process parameters, corrective action is also applied to the system to solve the unexpected failure of the process.

Authors contributions

Hossein Rezaeifar: Investigation, Methodology, Conceptualization, Writing-original draft.

Mohamed Elbestawi: Review and editing, Supervision.

3.5 References

[1] T. DebRoy, H.L. Wei, J.S. Zuback, T. Mukherjee, J.W. Elmer, J.O. Milewski, A.M. Beese, A. Wilson-Heid, A. De, W. Zhang, Additive manufacturing of metallic components – Process, structure and properties, Prog. Mater. Sci. 92 (2018) 112–224. https://doi.org/10.1016/j.pmatsci.2017.10.001.

[2] S. Kumar and S. Kumar, "Laser Powder Bed Fusion," in *Additive Manufacturing Processes*, Springer International Publishing, 2020, pp. 41–63.

[3] I. Gibson, D. W. Rosen, and B. Stucker, *Additive manufacturing technologies: Rapid prototyping to direct digital manufacturing*. Springer US, 2010.

[4] M. Grasso and B. M. Colosimo, "Process defects and in situ monitoring methods in metal powder bed fusion: A review," *Measurement Science and Technology*, vol. 28, no. 4. Institute of Physics Publishing, p. 044005, Apr. 01, 2017, doi: 10.1088/1361-6501/aa5c4f.

[5] Z. Zhang, Y. Huang, A. Rani Kasinathan, S. Imani Shahabad, U. Ali, Y. Mahmoodkhani, E. Toyserkani, "3-Dimensional heat transfer modeling for laser powder-bed fusion additive manufacturing with volumetric heat sources based on varied thermal conductivity and absorptivity," *Opt. Laser Technol.*, vol. 109, pp. 297–312, Jan. 2019, doi: 10.1016/j.optlastec.2018.08.012.

[6] E. Fereiduni, A. Ghasemi, and M. Elbestawi, "Selective laser melting of aluminum and titanium matrix composites: Recent progress and potential applications in the aerospace industry," *Aerospace*, vol. 7, no. 6, 2020, doi: 10.3390/AEROSPACE7060077.

[7] M. Abdelrahman, E. W. Reutzel, A. R. Nassar, and T. L. Starr, "Flaw detection in powder bed fusion using optical imaging," *Addit. Manuf.*, vol. 15, pp. 1–11, May 2017, doi: 10.1016/j.addma.2017.02.001.

[8] A. Sola and A. Nouri, "Microstructural porosity in additive manufacturing: The formation and detection of pores in metal parts fabricated by powder bed fusion," *J. Adv. Manuf. Process.*, vol. 1, no. 3, Jul. 2019, doi: 10.1002/AMP2.10021.

[9] R. Snell, L. Tammas-Williams S, Chechik, A. Lyle, E. Hernández-Nava, C. Boig, G. Panoutsos, I. Todd, "Methods for Rapid Pore Classification in Metal Additive Manufacturing," *JOM*, vol. 72, no. 1, pp. 101–109, Jan. 2020, doi: 10.1007/s11837-019-03761-9.

[10] C. Bruna-Rosso, A. G. Demir, and B. Previtali, "Selective laser melting finite element modeling: Validation with high-speed imaging and lack of fusion defects prediction," *Mater. Des.*, vol. 156, pp. 143–153, Oct. 2018, doi: 10.1016/j.matdes.2018.06.037.

[11] A. Simchi and H. Pohl, "Effects of laser sintering processing parameters on the microstructure and densification of iron powder," *Mater. Sci. Eng. A*, vol.

359, no. 1–2, pp. 119–128, 2003, doi: 10.1016/S0921-5093(03)00341-1.

[12] Y. Li and D. Gu, "Parametric analysis of thermal behavior during selective laser melting additive manufacturing of aluminum alloy powder," *Mater. Des.*, vol. 63, pp. 856–867, 2014, doi: 10.1016/j.matdes.2014.07.006.

[13] S. M. Yusuf, Y. Chen, R. Boardman, S. Yang, and N. Gao, "metals Investigation on Porosity and Microhardness of 316L Stainless Steel Fabricated by Selective Laser Melting," 2017, doi: 10.3390/met7020064.

[14] A. Bauereiß, T. Scharowsky, and C. Körner, "Defect generation and propagation mechanism during additive manufacturing by selective beam melting," *J. Mater. Process. Technol.*, vol. 214, no. 11, pp. 2522–2528, Nov. 2014, doi: 10.1016/J.JMATPROTEC.2014.05.002.

[15] A. du Plessis, "Effects of process parameters on porosity in laser powder bed fusion revealed by X-ray tomography," *Addit. Manuf.*, vol. 30, no. September, p. 100871, 2019, doi: 10.1016/j.addma.2019.100871.

[16] G. Vastola, Q. X. Pei, and Y. W. Zhang, "Predictive model for porosity in powder-bed fusion additive manufacturing at high beam energy regime," *Addit. Manuf.*, vol. 22, pp. 817–822, Aug. 2018, doi: 10.1016/j.addma.2018.05.042.

[17] H. Choo, KL. Sham, J. Bohling, A. Ngo, X. Xiao, Y. Ren, PJ. Depond, MJ. Matthews, E. Garlea, "Effect of laser power on defect, texture, and

microstructure of a laser powder bed fusion processed 316L stainless steel," *Mater. Des.*, vol. 164, p. 107534, Feb. 2019, doi: 10.1016/j.matdes.2018.12.006.

[18] W. Yu, S. Leong Sing, C. Kai Chua, and X. Tian, "Influence of re-melting on surface roughness and porosity of AlSi10Mg parts fabricated by selective laser melting," 2019, doi: 10.1016/j.jallcom.2019.04.017.

[19] A. du Plessis, I. Yadroitsava, and I. Yadroitsev, "Effects of defects on mechanical properties in metal additive manufacturing: A review focusing on X-ray tomography insights," *Mater. Des.*, vol. 187, p. 108385, 2020, doi: 10.1016/j.matdes.2019.108385.

[20] Q. C. Liu, J. Elambasseril, S. J. Sun, M. Leary, M. Brandt, and P. K. Sharp, "The effect of manufacturing defects on the fatigue behaviour of Ti-6Al-4V specimens fabricated using selective laser melting," *Adv. Mater. Res.*, vol. 891–892, pp. 1519–1524, 2014, doi: 10.4028/www.scientific.net/AMR.891-892.1519.

[21] A. du Plessis and E. Macdonald, "Hot isostatic pressing in metal additive manufacturing: X-ray tomography reveals details of pore closure," *Addit. Manuf.*, vol. 34, no. March, p. 101191, 2020, doi: 10.1016/j.addma.2020.101191.

[22] M. Yakout, M. A. Elbestawi, and S. C. Veldhuis, "Density and mechanical properties in selective laser melting of Invar 36 and stainless steel 316L," *J.*

Mater. Process. Technol., vol. 266, pp. 397–420, Apr. 2019, doi: 10.1016/j.jmatprotec.2018.11.006.

[23] F. Caiazzo, V. Alfieri, and G. Casalino, "On the Relevance of volumetric energy density in the investigation of inconel 718 laser powder bed fusion," *Materials (Basel).*, vol. 13, no. 3, Feb. 2020, doi: 10.3390/ma13030538.

[24] T. Peng and C. Chen, "Influence of Energy Density on Energy Demand and Porosity of 316L Stainless Steel Fabricated by Selective Laser Melting," *Int. J. Precis. Eng. Manuf. Technol.*, vol. 5, no. 1, p. 55, 2018, doi: 10.1007/s40684-018-0006-9.

[25] M. Narvan, K. S. Al-Rubaie, and M. Elbestawi, "Process-structure-property relationships of AISI H13 tool steel processed with selective laser melting," *Materials (Basel).*, vol. 12, no. 14, pp. 1–20, 2019, doi: 10.3390/ma12142284.

[26] E. Malekipour and H. El-Mounayri, "Common defects and contributing parameters in powder bed fusion AM process and their classification for online monitoring and control: a review," *Int. J. Adv. Manuf. Technol.*, vol. 95, no. 1–4, pp. 527–550, 2018, doi: 10.1007/s00170-017-1172-6.

[27] S. Giganto, P. Zapico, M. Á. Castro-Sastre, S. Martínez-Pellitero, P. Leo, and P. Perulli, "Influence of the scanning strategy parameters upon the quality of the SLM parts," in *Procedia Manufacturing*, Jan. 2019, vol. 41, pp. 698–705, doi: 10.1016/j.promfg.2019.09.060.

[28] M. C. Sow, T. De Terris, O. Castelnau, Z. Hamouche, F. Coste, R. Fabbro, P. Peyre, "Influence of beam diameter on Laser Powder Bed Fusion (L-PBF) process," *Addit. Manuf.*, vol. 36, no. July, 2020, doi: 10.1016/j.addma.2020.101532.

[29] A. Ladewig, G. Schlick, M. Fisser, V. Schulze, and U. Glatzel, "Influence of the shielding gas flow on the removal of process by-products in the selective laser melting process," *Addit. Manuf.*, vol. 10, pp. 1–9, Apr. 2016, doi: 10.1016/j.addma.2016.01.004.

[30] J. L. Bartlett, F. M. Heim, Y. V. Murty, and X. Li, "In situ defect detection in selective laser melting via full-field infrared thermography," *Addit. Manuf.*, vol. 24, pp. 595–605, 2018, doi: 10.1016/j.addma.2018.10.045.

[31] S. Coeck, M. Bisht, J. Plas, and F. Verbist, "Prediction of lack of fusion porosity in selective laser melting based on melt pool monitoring data," *Addit. Manuf.*, vol. 25, no. October 2018, pp. 347–356, 2019, doi: 10.1016/j.addma.2018.11.015.

[32] J.-B. Forien, N. P. Calta, P. J. DePond, G. M. Guss, T. T. Roehling, and M. J. Matthews, "Detecting keyhole pore defects and monitoring process signatures during laser powder bed fusion: a correlation between in situ pyrometry and ex situ X-ray radiography," *Addit. Manuf.*, no. April, p. 101336, 2020, doi: 10.1016/j.addma.2020.101336.

[33] P. Mercelis, J. P. Kruth, and J. Van Vaerenbergh, "Feedback control of

selective laser melting," *Proc. 15th Int. Symp. Electromachining, ISEM 2007*, pp. 421–426, 2007.

[34] H. Rezaeifar and M. A. Elbestawi, "On-line melt pool temperature control in L-PBF additive manufacturing," *Int. J. Adv. Manuf. Technol.*, vol. 112, no. 9–10, pp. 2789–2804, Feb. 2021, doi: 10.1007/s00170-020-06441-0.

[35] H. Qin, V. Fallah, Q. Dong, M. Brochu, M. R. Daymond, and M. Gallerneault, "Solidification pattern, microstructure and texture development in Laser Powder Bed Fusion (LPBF) of Al10SiMg alloy," *Mater. Charact.*, vol. 145, pp. 29–38, Nov. 2018, doi: 10.1016/j.matchar.2018.08.025.

[36] S. Moylan, E. Whitenton, B. Lane, and J. Slotwinski, "Infrared thermography for laser-based powder bed fusion additive manufacturing processes," in *AIP Conference Proceedings*, Feb. 2014, vol. 1581 33, no. 1, pp. 1191–1196, doi: 10.1063/1.4864956.

[37] H. Krauss, C. Eschey, and M. F. Zaeh, "Thermography for Monitoring the Selective Laser Melting Process." Accessed: May 16, 2021. [Online]. Available: http://utw10945.utweb.utexas.edu/Manuscripts/2012/2012-76-Krauss.pdf.

[38] J. Reijonen, A. Revuelta, T. Riipinen, K. Ruusuvuori, and P. Puukko, "On the effect of shielding gas flow on porosity and melt pool geometry in laser powder bed fusion additive manufacturing," *Addit. Manuf.*, vol. 32, p.

101030, Mar. 2020, doi: 10.1016/j.addma.2019.101030.

[39] S. W. Strauss, "Nuclear Science and Engineering The Temperature Dependence of the Viscosity of Liquid Metals," *Taylor Fr.*, vol. 12, no. 3, pp. 436–439, Mar. 2017, doi: 10.13182/NSE62-A28099.

[40] I. Ferreira, J. de Castro, A. G.-W. and Interfacial, and U. 2019, "Dependence of surface tension and viscosity on temperature in multicomponent alloys," in *Wettability and Interfacial Phenomena-Implications for Material Processing*, 2019.

[41] Y. Chen, SJ. Clark, CLA Leung, L. Sinclair, S. Marussi, MP. Olbinado, E. Boller, A. Rack, I. Todd, PD. Lee, "In-situ Synchrotron imaging of keyhole mode multi-layer laser powder bed fusion additive manufacturing," *Appl. Mater. Today*, vol. 20, p. 100650, Sep. 2020, doi: 10.1016/j.apmt.2020.100650.

Chapter 4

Minimizing the surface roughness in L-PBF additive manufacturing process using a combined feedforward plus feedback control system

Complete Citation:

Rezaeifar, Hossein, and Mohamed Elbestawi. " Minimizing the surface roughness in L-PBF additive manufacturing process using a combined feedforward plus feedback control system." *Journal of Manufacturing Processes*

Abstract

This study aims at minimizing the top surface roughness of the parts manufactured by the laser powder bed fusion (L-PBF) process by deploying a Feedforward plus Feedback control system. The most common factors affecting the surface quality, namely, balling, lack of inter-track overlap, overlapping curvature of laser scan tracks, and spatters, were investigated through a monitoring system consisting of a high-speed camera, a zooming lens, and a short pass filter. The desired melt pool width and the critical value for the level of spatters were determined using the imaging system and subsequent image processing. An experimental model was developed, and the control system was designed accordingly. The performance of the control system was evaluated by simulations and experiments. In all cases, the control system showed an excellent transient performance to reach the desired melt pool width only after printing a few layers. Also, the control system was evaluated at different scanning speeds and with different geometries. The results obtained from this study showed that controlling the geometry of the melt pool can mitigate significant defects occurring during the process and minimize the top surface roughness.

Keywords

Laser powder bed fusion, Monitoring of additive manufacturing, Surface roughness, Defects, Control of additive manufacturing.

Abbreviations

AM	Additive Manufacturing
CAD	Computer-Aided Design
EDM	Electrical Discharge Machining

FB	Feedback
FF	Feedforward
L-PBF	Laser Powder Bed Fusion
MPC	Model Predictive Control
PD	Proportional-Derivative
PID	Proportional-Integral-Derivative
PM	Partially-Melted
SEM	Scanning Electron Microscopy
UM	Un-Melted

4.1 Introduction

Laser powder bed fusion (L-PBF) process is a well-established additive manufacturing (AM) technology in which metal powders are fused layer-by-layer to fabricate near-net-shape parts in two main stages. First, the powder is uniformly deposited on a substrate. Then, a high-power laser selectively melts powder particles based on a computer-aided design (CAD) model. This process continues until the final component is built [1–6]. The development of the L-PBF process has expanded the freedom in design and provided the opportunity to fabricate parts with complex shapes and intricate features without the need for expensive assemblies [7]. However, internal defects and unacceptable surface quality of parts in the as-built condition are major concerns toward fully implementing this unprecedented technology in many industries, especially the aerospace and marine. The high surface roughness adversely impacts the mechanical properties of the final product, especially the fatigue performance, since surface asperities can act as preferential crack nucleation sites during cyclic loading [8,9].

The surface quality of the L-PBF fabricated parts can be categorized into two groups of side-surface and top surface quality. The surface roughness corresponding to the side surface originates mainly from the “stair-stepping effect”[1,10,11] and adhered powder particles. The former correlates to the layer thickness and part orientation, and the latter finds its route in powder attribute [12] (e.g., particle size and size distribution), meaning that both cannot be adjusted during the process. On the other hand, the top surface quality is related to defects (i.e., lack of inter-track overlap and balling), spatters, and the overlapping curvature of laser scan tracks [13–16], as explained in the following:

1. Balling: At extremely high scanning speeds and relatively low laser powers, the elongated melt pools break up into smaller entities of spherical/semi-spherical shape to reduce the significant difference in the surface tension. This effect is known as the balling phenomenon (Figure 4-1(a)) [17–19]. Formation of gouged and humped regions at such conditions results in discontinuous laser scan tracks, which can act as severe impediments to the uniform deposition of the next powder layer and subsequently cause severe top surface roughness.
2. Lack of inter-track overlap: This is referred to a situation in which the amount of energy delivered to the powder bed during the L-PBF process is not sufficient for the complete melting of the powder particles. (Figure 4-1(b)) [20–23]. At extremely low absorbed energy, the gap existing between adjacent tracks contains unmelted/partially melted (UM/PM) powder particles. These openings in each layer make the layer thickness at some local regions larger for the subsequent layer, resulting in surface roughness deterioration or even process failure.
3. Spatter: Spatters are caused by the Marangoni convection combined with the recoil pressure, which acts to eject the molten material from the melt pool to the surrounding [24,25]. Despite the low recoil pressure, which facilitates the melt pool flattening during the L-PBF process, the high recoil pressure caused by the extremely high absorbed energy leads to the material evaporation, melt explosion, and creation of metallic jets [26,27]. When crushed by the metallic vapor, the ejected material is broken into micro-sized molten droplets. The dispersed droplets are called spatters [28–30]. If the spatter droplets solidify on the surface of the layer, they can affect the surface quality. Figure 4-1(c) shows the spatters on the final layer, which can directly affect the surface roughness.

4. Overlapping curvature of laser scan tracks: In cases where there is no gap between the adjacent laser scan tracks, the curvature of the tracks still results in the formation of peaks and valleys on the consolidated surface, leading to top surface roughness. The influence of this factor on the surface roughness alleviates by increasing the level of inter-track overlap [16].

According to the abovementioned discussion, post-processing seems essential to obtain the desired surface quality for many applications. Based on [31], laser polishing, machining, and electropolishing are the most versatile methods for improving the surface roughness of the L-PBF fabricated components. Given that all these techniques are costly and time-consuming, there is a huge interest in limiting them by reducing the surface roughness of L-PBF processed parts in the as-built condition. To address this, one feasible approach is implementing an online method capable of simultaneously preventing defect formation (i.e., defects affecting the surface quality) and improving the surface roughness by real-time adjustment of the process parameters.

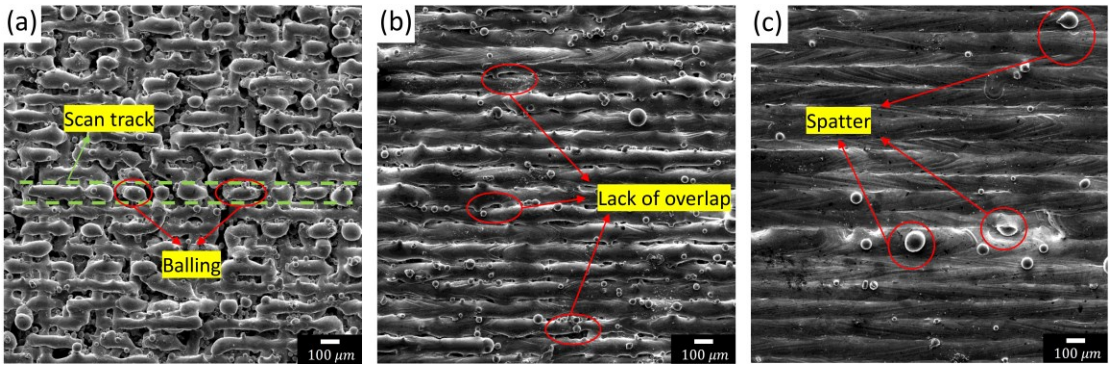

Figure 4-1 Factors that impact the surface quality: (a) Balling effect, (b) Lack of inter-track overlap, and (c) Spatters solidified on the top surface of the sample.

Two of the factors affecting the surface roughness, namely, lack of inter-track overlap and overlapping curvature of scan tracks, are correlated to the width of the melt pool [16,20]. In other words, for a given hatch spacing, the surface roughness will be minimized if the width of the melt pool exceeds a critical value. According to [1], balling also can be correlated to the dimensions of the melt pool. In fact, the melt pool turns into the unstable mode when the ratio of the length to width of the melt pool transcends a certain value resulting in ball-shaped beads. Therefore, the dimensions of the melt pool play a crucial role in forming the defects mentioned above. The dimensions of the melt pool depend on several factors, such as process variables, as well as the height and geometry of the part. For example, variations of scanning surface in building direction result in different melt pool temperatures and consequently melt pool dimensions in complex geometries [32]. In addition, the level of spatters also changes because of the mentioned factors. For instance, Gunenthiram et al. [33] showed that spatters increase by increasing the laser power. Therefore, a control approach that can control the dimensions of the melt pool and keep the level of spatters lower than a critical value solves the defects and consequently improves the surface quality of the part fabricated by the L-PBF process. It is worth noting that remelting of the last layer can significantly improve the surface quality, as suggested by Yasa et al. [34]. However, remelting of the last layer cannot solve the internal defects in previous layers. As noted, these defects can create conditions that result in increased surface roughness or part failure during the process. Layer-by-layer re-melting has also been employed in the literature to improve the surface roughness [34–36]. Although this strategy might solve the internal defects and improve the surface quality, it adversely affects the dimensional accuracy and causes grain coarsening as well as ductility and fatigue life reduction [37,38].

A few attempts have been made recently to control the melt pool dimensions in the L-PBF process. Xi [39] investigated the performance of the proportional-integral-derivative (PID) control and model predictive control (MPC) approaches in controlling the melt pool depth and width via implementing various simulations. Similarly, Hussain et al. [40] implemented a simulation-based control of the melt pool area. However, the simulations fail to provide a precise prediction of the real conditions. Vasileska et al. [41] controlled the melt pool area via a layer-wise feedback control approach in a pulsed-wavelength L-PBF machine by manipulating the duty cycle of the laser power to correct the swelling defect. However, the defects and issues mentioned above have a greater effect on the surface roughness. Therefore, the effect of the control approaches in improving the surface quality requires further investigation.

This research study proposes a Feedforward plus Feedback (FF plus FB) control system to keep the melt pool width of Inconel 625 superalloy close to the desired value and the level of spatters lower than a critical value during the L-PBF process to mitigate the defects and improve the surface quality. For this purpose, first, a monitoring system consisting of a high-speed camera, zooming lens, and low-pass filter capable of capturing the melt pool width and level of spatters was implemented. Then, the camera was calibrated through three steps, and the image processing steps were implemented for capturing the required information. Next, a set of experiments was utilized to determine the desired melt pool width and the suitable range for the level of spatters using the described sensors and microscopy. After that, the process model was obtained utilizing the modified two-innovation stochastic gradient descent approach and the data gathered from the high-speed camera. Some simulations were conducted to evaluate the performance of the control system. Finally, the control system was experimentally implemented on the L-PBF

machine. The performance of the controller was examined for three different scenarios, and the surface quality of the fabricated parts was investigated. The information gained from the surface roughness measurements and SEM observations reinforces the idea that applying an appropriate control system not only improves the surface quality at different scanning speeds but also mitigates defect formation and makes the fabrication of almost defect-free parts with the minimized surface roughness time-and-cost effective.

4.2 Experimental procedure

4.2.1 Fabrication procedure

In this study, an OmniSint-160 L-PBF machine equipped with a Yb-fiber laser with a maximum laser power of 400 W, a wavelength of 1090 nm, and a spot size of 100 μm was utilized to print parts. The laser power can be manipulated layer-by-layer in this machine, making the control approach possible. The process chamber was filled with high-purity Ar gas to protect the melting area. Samples were printed on a small AISI 304 stainless steel disk located on top of the original build plate, the details of which are explained in [42]. The material used in the study was gas atomized Inconel 625 powder with a nominal particle size in the range of 15-45 μm. The scanning strategy was serpentine with 90 degrees rotation between two consecutive layers. The hatch spacing and nominal powder layer thickness in all parts were 100 and 30 μm, respectively.

4.2.2 Melt pool imaging and calibration

Figure 4-2 shows the high-speed imaging system mounted on the process chamber of the L-PBF machine. A FASTCAM MC2.1 high-speed camera (Photron) operating at 2 kHz acquisition frequency fitted with a TOYO OPTICS F1.8 zooming lens was employed to observe melt pool width and the level of spatters during the process. As shown in Figure

4-2, the camera was mounted off-axially at 40 cm from the build surface and a viewing angle of around 60 degrees. The images were taken with 50 μs integration time to capture melt pool characteristics, such as melt pool area (which was not elongated) and spatters. The camera had a spatial resolution of 512 × 512 pixels. A short pass filter with a cut-off wavelength of 1000 nm was located in front of the camera to eliminate the noise induced by the reflected laser beam.

Before performing the measurements, the camera is required to be calibrated. The calibration of the camera was done in three steps. As mentioned above, the camera was installed on the machine with an angle to the building surface, so there will be a perspective distortion in images captured by the camera (Figure 4-3(a)). Therefore, a calibration was necessary to transform the melt pool images from the side view to the top view. In addition, using the lens on the camera caused some distortion which was required to be addressed. A polynomial distortion model [43] was considered to correct both mentioned errors. The calibration was performed via calibration grid in LabView NI Vision Assistant. The details of the calibration procedure have been explained in [44,45]. Figure 4-3 illustrates an image before and after the distortion calibration. Following the distortion calibration, another calibration step was performed to capture the measurements of the true dimensions after solidification. Four single tracks were printed, and at the same time, the widths of the melt pools were measured in pixels via the monitoring system. Finally, the true width of the melt pool was measured using scanning electron microscopy (SEM), and ImageJ was utilized to convert the pixel measurements to the real measurements (Figure 4-4).

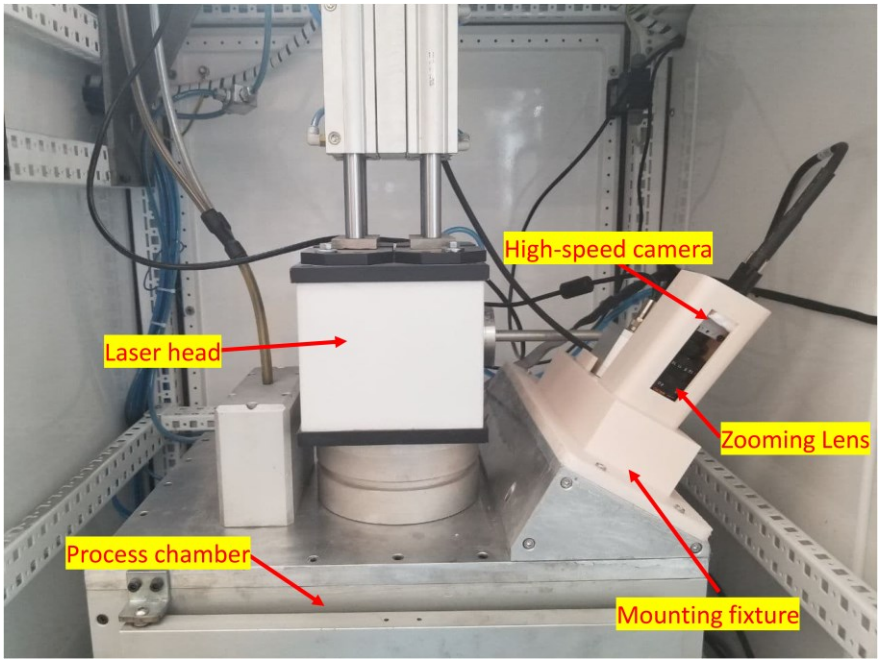

Figure 4-2 Monitoring system: the high-speed camera was mounted with a viewing angle of approximately 60º to the powder bed.

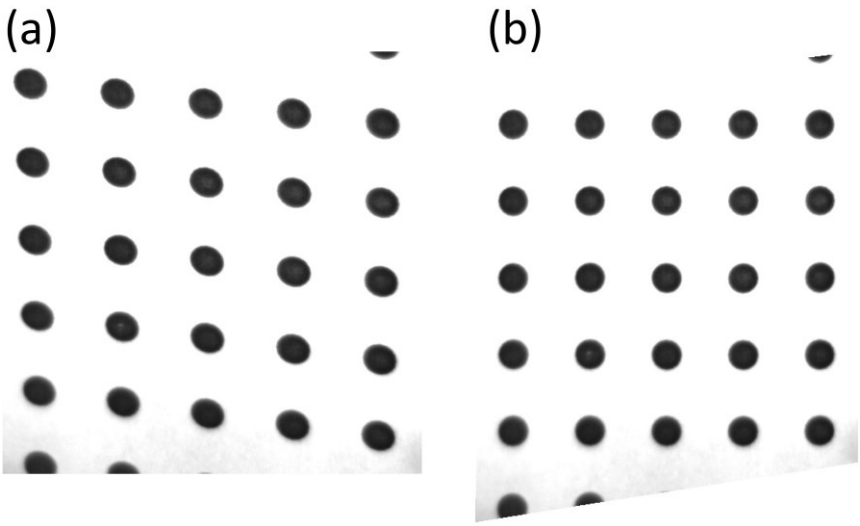

Figure 4-3 Grid calibration method: (a) image before calibration with perspective and lens distortion, and (b) corrected image after calibration.

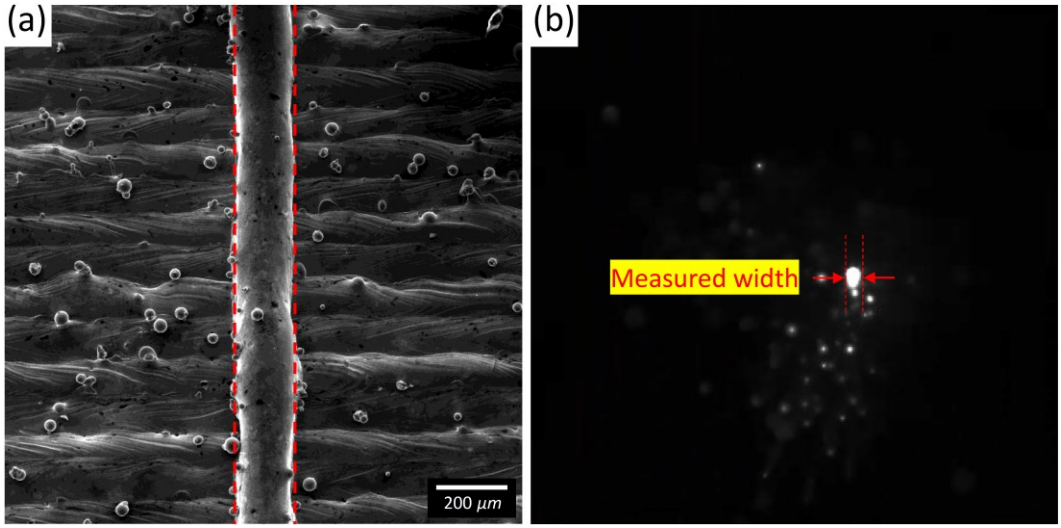

Figure 4-4 (a) Average of true width of the melt pool under SEM, and (b) measured melt pool width in pixel.

The raw images were required to be processed to obtain the dimensions of the melt pool and the level of spatters. For this purpose, the raw image after calibration transformation (Figure 4-5(a)) was converted to a binary image (Figure 4-5(b)), followed by an erosion image processing [46] to separate the spatters from the melt pool. Figure 4-5(c) shows the spatters, and Figure 4-5(d) illustrates the separated melt pool. However, the spatters tend to overlap and expand the melt-pool area because of the off-axial imaging system considered in this study. Therefore, the accuracy of the measurement would be degraded. To resolve this issue, another erosion image processing step was applied to the image to reduce the generated error (Figure 4-5(e)). Thereafter, the maximum feret diameter was considered as the length of the melt pool, and the dimension perpendicular to the maximum feret orientation was considered as the width of the melt pool (Figure 4-5(f)). It is worth mentioning that the mean pixel value of spatters determines the level of spatters in a single frame.

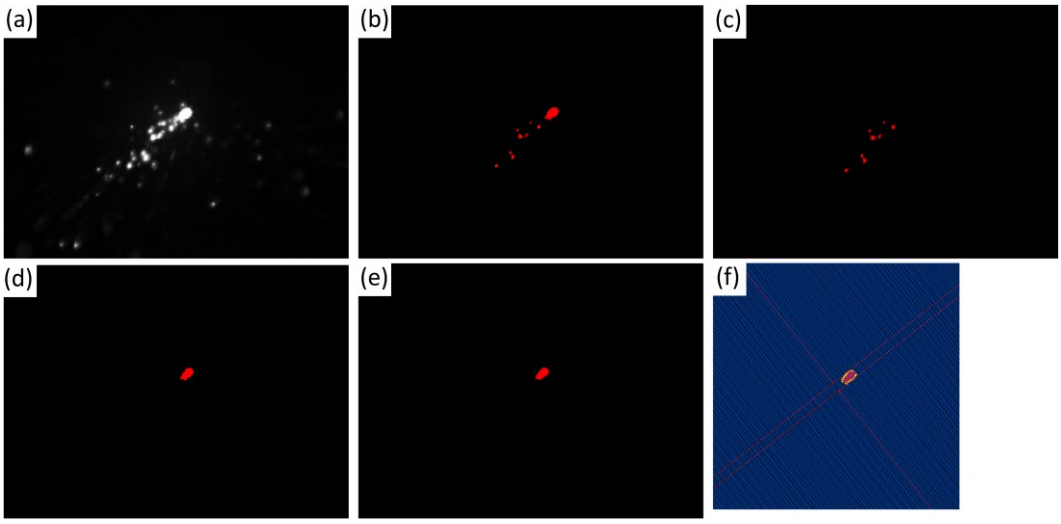

Figure 4-5 (a) Image after calibration, (b) binary image, (c) spatters, (d) melt pool separated from spatters, (e) corrected melt pool with erosion image processing step, and (f) measuring the melt pool dimensions.

4.2.3 Quality investigation procedure

The surfaces of the printed parts were observed using a TESCAN VEGA scanning electron microscopy (SEM) working at an accelerating voltage of 20 kV. The surface roughness of the samples was measured with Alicona "InfiniteFocus" microscope and Mitutoyo SJ-410 stylus profilometer. The surface roughness measurements reported in this study are the arithmetic mean surface roughness value (Sa) and the arithmetic mean deviation (Ra). For measuring the density and investigating the melt pool width, samples were removed from the disks by electrical discharge machining (EDM) and were sectioned along the building direction using a precision cutter. The samples were mounted in phenolic thermosetting resin and then ground with sequentially finer SiC grinding papers. The polishing was performed using 9, 3, and 1 μm diamond suspensions, respectively. Etching was performed by mixed acid etchant with the chemical composition of 75 ml HCl and 25 ml HNO3.

Optical imaging of the sectioned parts was conducted by a Keyence VHX-5000 digital microscope.

4.3 Defects investigation

The experimental investigation was conducted on 18 samples with dimensions of 10 mm× 10 mm× 10 mm printed with a fixed scanning speed of 500 mm/s and various laser powers changing from 60 to 230 W (Part 1 to 18) with an increment of 10 W. The camera captured the width and the level of spatters during the process. However, the measurements of the last layer were used to explain the surface quality.

As shown in Figure 4-6(a), the surface of Part 1 was full of discontinuous scan tracks originating from a severe balling. In Part 3 (Figure 4-6(b)), although the surface still contained discontinuous tracks, the level of balling decreased. Part 7 was the first part having uniform tracks (Figure 4-6(c)). However, the adjacent tracks did not have enough overlap, leading to the presence of UM/PM particles between the tracks. The surface roughness of Parts 3 and 7 were compared in Figure 4-7. The average Sa in Parts 3 and 7 was 25.953 and 20.422 μm, respectively, revealing that the adverse effect of the balling phenomenon on the surface quality is higher than that of the lack of fusion. Nevertheless, keeping the width of the melt pool at a suitable value not only solves the lack of fusion defects but also eliminates the balling phenomenon. In Part 10, tracks had an acceptable overlap (Figure 4-6(d)). However, the surface would be more flattened by increasing the laser power since, at this condition, the melt pool becomes wider, and the overlapping curvature of the laser scan tracks becomes more moderate. Also, the melt pool temperature shows an ascending trend by increasing the laser power, which in turn decreases the viscosity of the molten material and provides a situation for the excellent melt flow and

wetting of adjacent tracks. For example, Part 14, shown in Figure 4-6(e), had a better surface quality than Part 10. The trend of improving the surface roughness with increasing the laser power continued until a high level of spatters adversely affected the surface quality. For instance, a great amount of large spatters was formed on the surface of Part 18, as shown in Figure 4-6(f).

The Sa of Part 9 to Part 18 was measured to investigate the effect of laser power and spatters on the surface quality. As shown in Figure 4-8, Sa reduced from Part 9 to Part 14. Part 15 also had the Sa almost similar to Part 14. Then, in Part 16, 17, and 18 the average Sa increased noticeably. Therefore, it can be interpreted that increasing the laser power

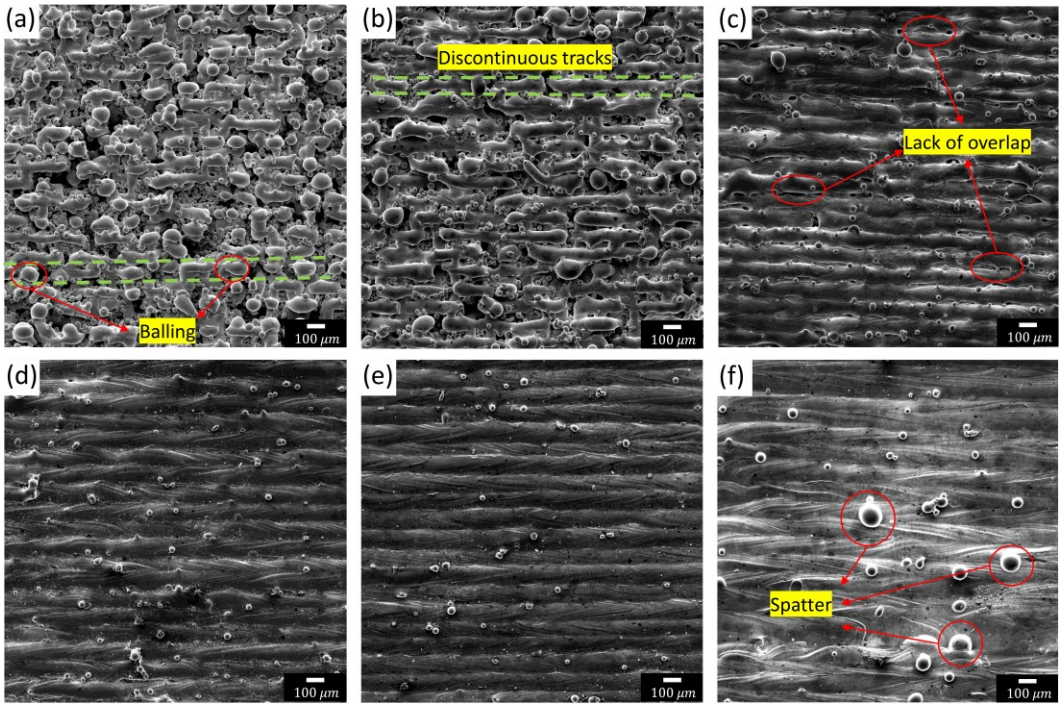

Figure 4-6 SEM images of: (a) Part 1, which had a huge amount of balling, (b) Part 3 in which the amount balling decreased in comparison to Part 1, (c) Part 7 with lack of inter-track overlap, (d) Part 10, (e) Part 14 which had a better surface quality compared to Part 10, and (f) Part 18, the spatters affected the top surface quality.

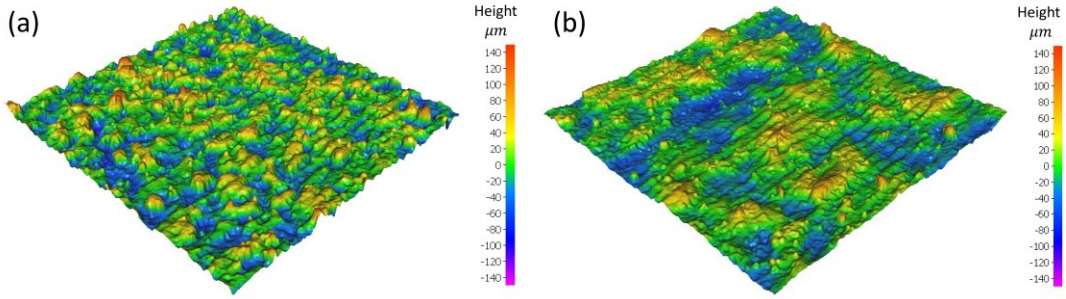

Figure 4-7 Color-3D images showing the top surface topography of parts produced by L-PBF processing of: (a) Part 3 with the laser power of 80 W and the scanning speed of 500 mm/s, and (b) Part 7 with the laser power of 120 W and the scanning speed of 500 mm/s.

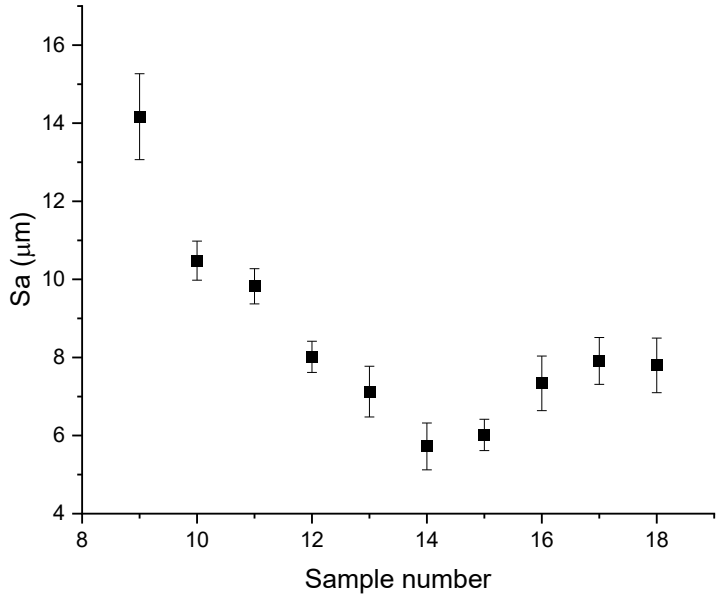

Figure 4-8 Surface roughness of the Parts 9 to 18.

decreased the Sa until Part 15, and then a large amount of spatters adversely affected the surface. Although the focus of this study is on minimizing the surface roughness, the level of porosity was also inspected to see whether increasing the laser power deteriorates the internal quality of the part drastically. The relative density of the parts is listed in Table 4-

1. Samples 15 to 18 had relative densities higher than 99%, which shows that the effect of the laser power on the internal porosity was not extreme in this range. Therefore, the level of spatters can be considered as the only factor determining an upper boundary to improve the surface quality. Table 4-1 also shows the level of spatters for the last layer measured by the high-speed camera, confirming that it has increased by increasing the laser power. As a result, the level of spatters was kept lower than 42.929, corresponding to Part 15, to remove the negative impact of spatters on the surface quality. Moreover, the desired width of the melt pool was obtained from the etched sections of the samples. Figure 4-9 shows that the desired melt pool for having a suitable overlap is 171 μm, which was used in the control system as the reference width.

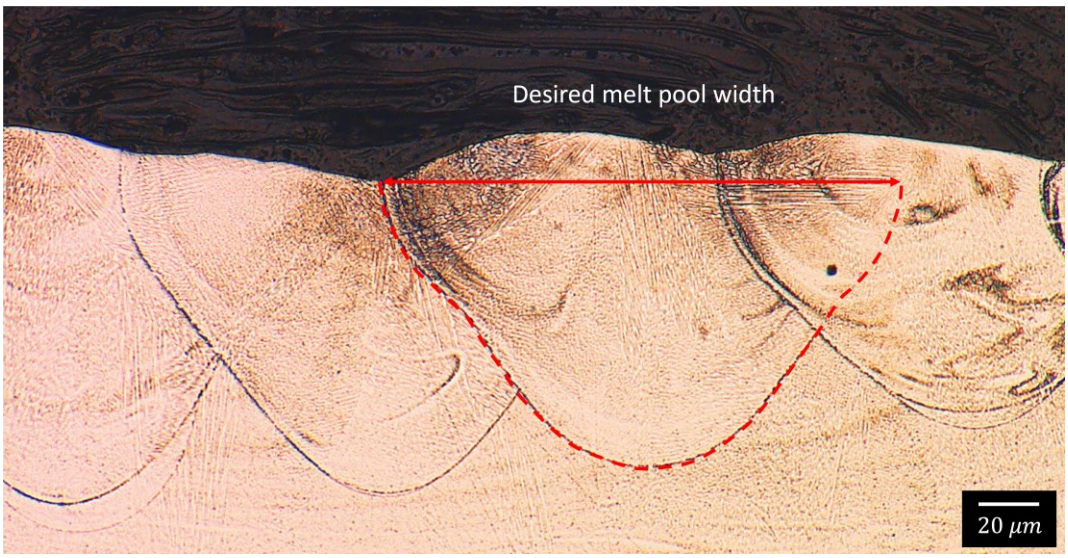

Figure 4-9 Desired melt pool width by assuming approximate symmetry of the melt pool.

Table 4-1 The process parameters, relative densities, and the level of spatters in final layer of the parts fabricated in this study.

Sample number	Laser power (W)	Scanning speed (mm/s)	Average relative density (%)	Level of spatters (pixels)
9	140	500	98.64	9.615
10	150		99.11	12.429
11	160		99.56	17.857
12	170		99.89	39.071
13	180		99.85	37.538
14	190		99.85	39.143
15	200		99.7	42.929
16	210		99.59	50.643
17	220		99.52	59.636
18	230		99.43	52.481

4.4 Modeling and Control

4.4.1 System identification approach

Prior to implementing the control strategy in the real plant, a model is required to be developed to make the evaluation of the control system possible through a simulation method. System identification is the most common method in the literature among different modeling approaches which has been utilized to demonstrate the AM process [47–49] for control purposes. For system identification, a combination of 20 scanning speeds and laser powers was used.

Based on [50,51], the melt pool width increases by increasing the input energy. However, the relation between the melt pool width and input energy is not linear. Given that the layer thickness and hatch spacing were constant in this study, the input energy can be represented by $\frac{P}{V}$. Figure 4-10(a) shows that there is no specific correlation between the average width of the melt pool and its corresponding $\frac{P}{V}$. As a matter of fact, the absorbed energy, rather than the input energy, is the factor determining the melt pool dimensions. The absorbed energy is dictated by the absorptivity of the material at different conditions. Based on [52], the absorptivity of the material depends on the exposure time (T_e) of the laser beam, and for Ni, the absorptivity changes approximately proportional to the square root of the exposure time ($A \propto \sqrt{T_e}$). For continuous wavelength lasers, T_e is proportional to $\frac{1}{V}$. Therefore, the absorbed energy can be represented by $\frac{P}{\sqrt{V}}$. Figure 4-10(b) shows that the average width of the melt pool has approximately a linear relation with its corresponding $\frac{P}{\sqrt{V}}$. Thus, $\frac{P}{\sqrt{V}}$ was considered as the controller output or plant input. However, the situation of the previous layers affects the width of the melt pool in the ongoing layer. A second-order model was considered for the width of the melt pool to include the effect of the plant input and width of previous layers:

$$\frac{W(z)}{U(z)} = \frac{c\, z^{-1}}{1 - az^{-1} + bz^{-2}} \tag{4-1}$$

Eq. (4-1) can be rewritten as follows:

$$w(k) = aw(k-1) + bw(k-2) + cu(k-1) \tag{4-2}$$

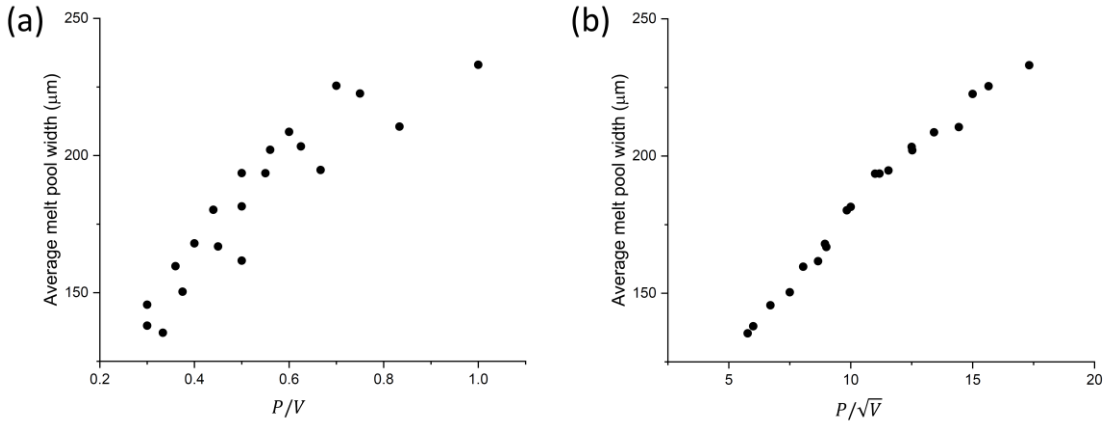

Figure 4-10 (a) There is no specific relationship between the average width of the melt pool and input energy, and (b) the average width of the melt pool has an approximately linear relationship with absorbed energy.

where $w(k)$ is the average width of the melt pool at layer k, and $u(k-1)$ is the output of the controller applied to the next layer (layer k). Coefficients a, b, and c were obtained using the modified two-innovation stochastic gradient descent approach [53]. Eq. (4-2) can be rewritten as:

$$w(k) = \varphi^T(k)\theta \tag{4-3a}$$

$$\theta = [a, b, c] \tag{4-3b}$$

$$\varphi(k) = [w(k-1), w(k-2), u(k-1)] \tag{4-3c}$$

$$\hat{\theta} = [\hat{a}, \hat{b}, \hat{c}] \tag{4-3d}$$

where θ and φ are the true value and the information vectors, respectively. Also, $\hat{\theta}$ is the estimated value during the identification process. In the modified two-innovation stochastic gradient descent, the cost function is:

$$J(\hat{\theta}) = J_1(\hat{\theta}) + J_2(\hat{\theta}) \tag{4-4a}$$

$$J_1(\hat{\theta}) = \frac{1}{2}\left(w(k-1) - \varphi^T(k-1)\hat{\theta}\right)^2 \tag{4-4b}$$

$$J_2(\hat{\theta}) = \frac{1}{2}\left(w(k) - \varphi^T(k)\hat{\theta}\right)^2 \tag{4-4c}$$

By considering the iteration function to find the minimum value of $J(\hat{\theta})$ as:

$$F(\hat{\theta}) = \hat{\theta} + a(p_1 + p_2) \tag{4-5}$$

Where p_1 and p_2 are the negative gradient directions and can be calculated as:

$$p_1 = -\Delta J_1 = \varphi(k-1)\left(w(k-1) - \varphi^T(k-1)\hat{\theta}\right) \tag{4-6a}$$

$$p_2 = -\Delta J_2 = \varphi(k)\left(w(k) - \varphi^T(k)\hat{\theta}\right) \tag{4-6b}$$

When $\hat{\theta}$ converges to the true value:

$$\hat{\theta} = F(\hat{\theta}) = \hat{\theta} + a(p_1 + p_2) \tag{4-7}$$

Then the cost function can be rewritten as:

$$J(a) = \sum_{i=0}^{1} \frac{1}{2}\left(w(k-i) - \varphi^T(k-i)\left(\hat{\theta} + a(p_1 + p_2)\right)\right)^2 \tag{4-8}$$

In order to obtain the minimum value of $J(a)$, $\frac{\partial J}{\partial a} = 0$ is required to be solved:

$$\frac{\partial J}{\partial a} = \sum_{i=0}^{1} \left(w(k-i) - \varphi^T(k-i) \left(\hat{\theta}_{t-1} + a(p_1 + p_2) \right) \right) . \left(-\varphi^T(k-i)(p_1 + p_2) \right) \tag{4-9a}$$

$$= 0$$

$$a = \frac{(p_1+p_2)^T(p_1+p_2)}{\sum_{i=0}^{1} \left(\varphi^T(k-i)(p_1+p_2) \right)^2} \tag{4-9b}$$

Therefore, each iteration can be implemented by Eq. (4-3), (4-6a), (4-6b), (4-7), and (4-9b).

4.4.2 Control strategy

As mentioned, the quality of the previous layers can affect the surface roughness of the next layers. Therefore, the proper situation should be provided for the process as quickly as possible. In other words, the response time of the controller requires to be short. An inverse model-based feedforward controller can provide a suitable control output to achieve the reference point in a short period [54,55]. However, in practice, a feedback controller is needed to compensate for the model inaccuracies. According to [56], using a feedforward-only controller in the presence of modeling error results in a steady-state error. In addition, due to the nature of the AM process, measurement errors are unavoidable, making it essential to deploy a feedback controller. In this study, an inverse model-based feedforward controller [55] was developed based on the model presented in section 4.4.1 and was used with a proportional-derivative (PD) controller in the parallel form to keep the width of the melt pool constant at the desired width (determined in section 3). The control system block diagram is shown in Figure 4-11. The Max spatters block uses the spatter level and laser power of the previous layer to prevent the controller from increasing the laser power when the level of spatters reaches the critical value. According to section 4.4.1,

u is $\frac{P}{\sqrt{V}}$ and can be achieved by $u_{ff} + u_{fb}$. u_{ff} is the controller output of the feedforward controller and can be formulated as:

$$\frac{U_{ff}(z)}{W_d(z)} = \frac{1 - az^{-1} + bz^{-2}}{cz^{-1}} \tag{4-10a}$$

$$u_{ff}(k-1) = \frac{w_d(k) - aw_d(k-1) + bw_d(k-2)}{c} \tag{4-10b}$$

where $w_d(k)$ is the desired width of the melt pool at layer k. u_{fb} is the output of the feedback controller and can be formulated as:

$$u_{fb}(k-1) = u_{fb}(k-2) + K_p e(k-1) + K_d\big(e(k-1) - e(k-2)\big) \tag{4-11}$$

4.4.3 Simulation Results

Three different simulation scenarios were carried out by means of MATLAB programming software to evaluate the performance of the proposed control system in preserving the width of the melt pool at the desired value. Figure 4-12(a) shows the variation of the melt pool width during the process without noises and modeling errors (perfect model). It can be seen that the desired melt pool width (mentioned in section 4.3) was achieved only after 6 layers. Although preparations were considered to avoid noises in the setup of the monitoring system, in an environment such as the L-PBF process chamber, a level of noise can happen during the measurements. Figure 4-12(b) illustrates the simulation results in the presence of some noises, which can produce errors up to 10 μm. The maximum error after reaching the desired width was 2.33 μm which shows that the controller performed well even in the presence of the noises. In addition, since all models fail to provide a perfect prediction in real conditions, a percent of error should be considered in the simulation. 20% modeling error was considered in this study. Accordingly, the real model would be:

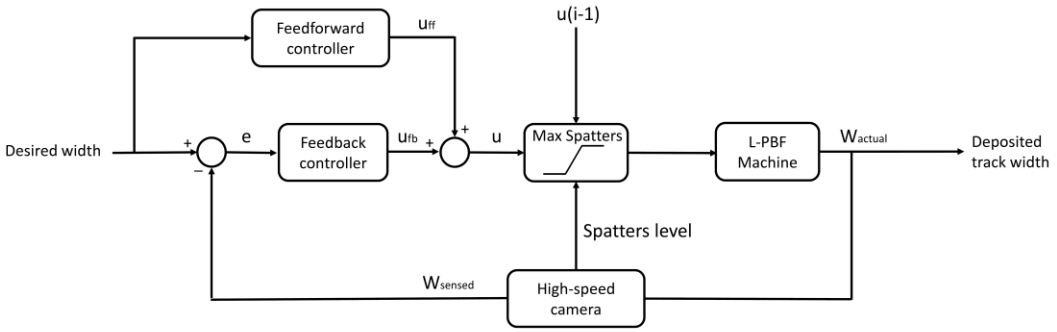

Figure 4-11 The block diagram of the control approach. u_{ff} is the controller output of the feedforward controller, and u_{fb} is the output of the feedback controller.

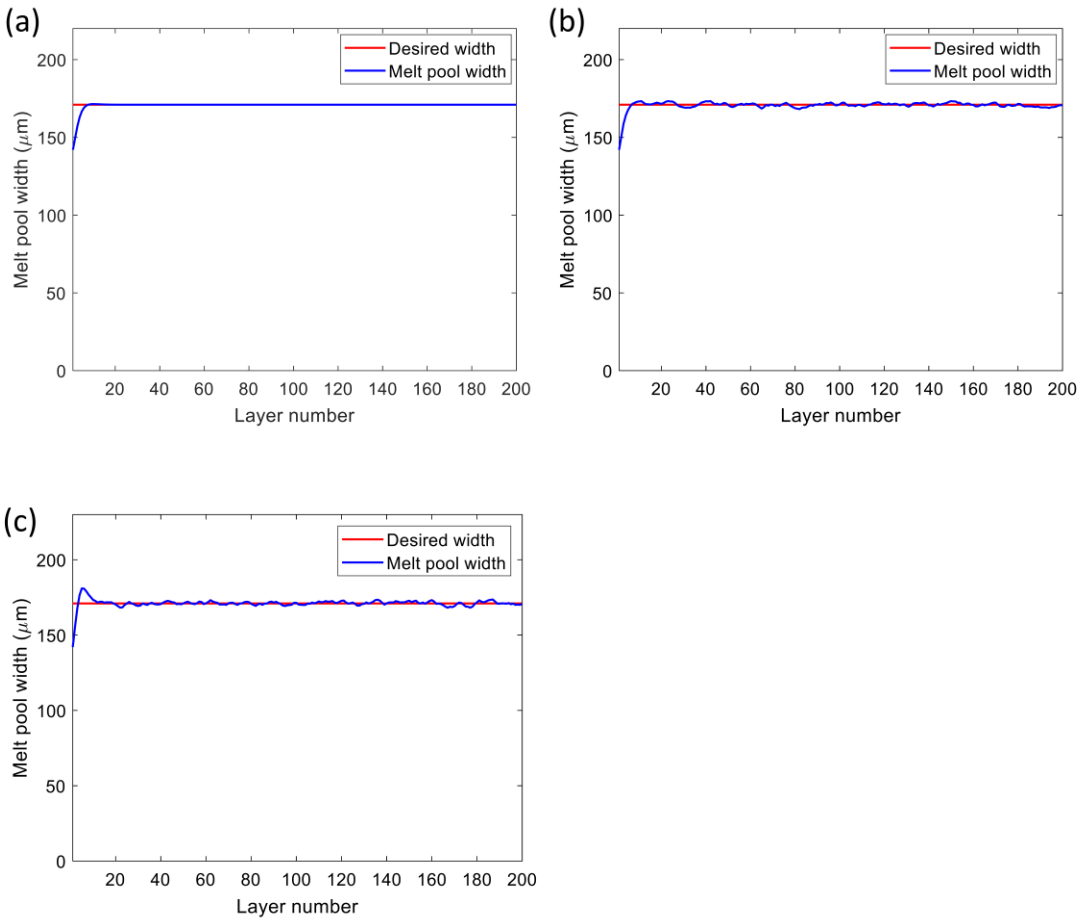

Figure 4-12 Simulation results for: (a) perfect model, (b) with noise, and (c) with noise and modeling error.

$$w(k) = aw(k-1) + bw(k-2) + (1.2c)u(k-1) \quad (4\text{-}12)$$

Figure 4-12(c) shows the result of the simulation when 20% modeling error and noises were taken into account. Although the response has 5.7% overshoot, the width of the melt pool reached the desired width after 11 layers, indicating that the FF plus FB controller can control the melt pool width even in the presence of modeling errors.

4.5 Experimental results and discussion

As mentioned in section 4.4.2, the FF plus FB controller was employed to track the desired width of the melt pool and avoid a high level of spatters during the process. In this section, three sets of experiments were carried out with different scenarios to examine the performance of the controller.

4.5.1 Controller performance at the scanning speed of 500 mm/s

In the first set of experiments, the performance of the control system was evaluated at the scanning speed that the defect investigation was performed (section 4.3). The initial laser power was 150 W, in which the density of the produced part would be higher than 99%. Then, the controller adjusted the laser power for the following 300 layers. Figure 4-13 shows the laser power and width of the melt pool versus the layer number during the process. The melt pool width and the laser power for the first 50 layers of the process are also presented in Figure 4-13 (c) and (d), respectively. The results indicate that the controller kept the melt pool width close to the desired value. In addition, the followings can be understood from this set of experiments:

1. Similar to the simulation, the response of the system (melt pool width) exceeded the desired width in the beginning of the process and then reached close to it. The

output of the feedforward controller is responsible for the observed deviation in the beginning of the process, though it caused the control system to perform faster.

2. As shown in Figure 4-13(c), at some layers, such as layer 36 (green circle), the response can have a high error because of fluctuations inside the process chamber. Nevertheless, it did not result in the instability of the process.
3. At layer 3 (red circle in Figure 4-13(d)), the average spatter level was 43.94 pixels, preventing the controller from increasing the laser power, though the measurements of the melt pool width were lower than the desired one.

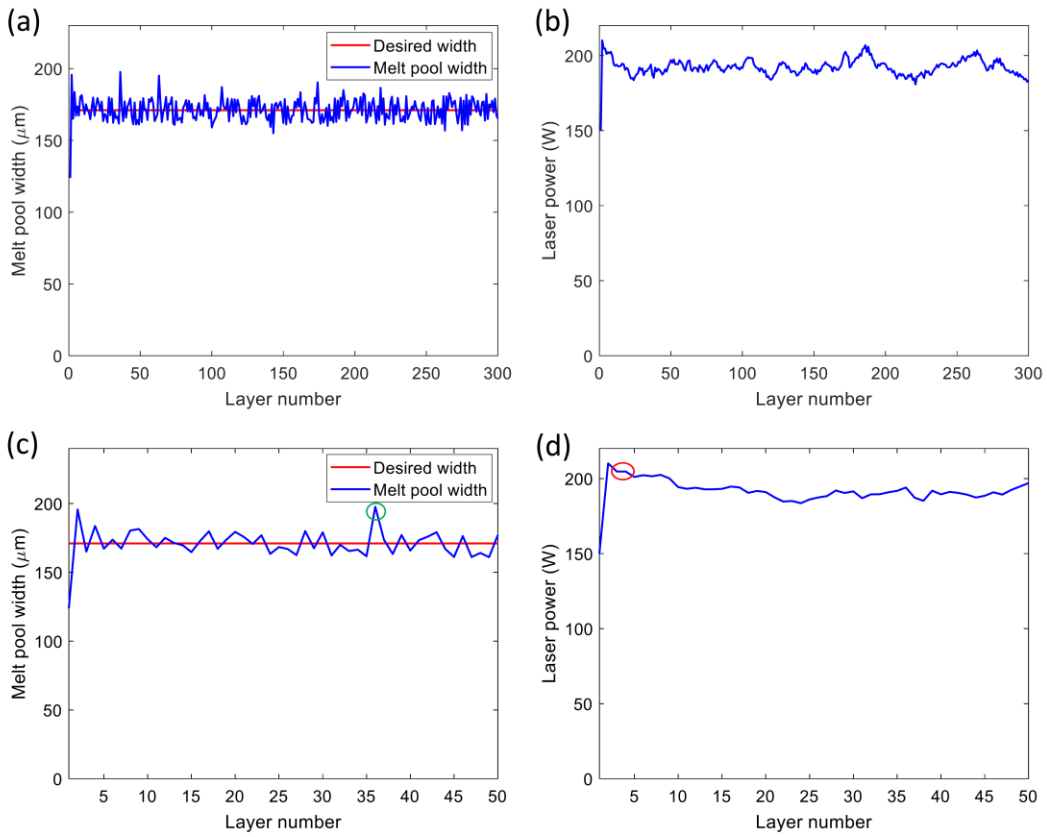

Figure 4-13 (a) The melt pool width during the control process at 500 mm/s, (b) the laser power during the control process at 500 mm/s, (c) the melt pool width during the control process for the initial 50 layers, and (d) the laser power during the control process for the initial 50 layers.

Besides, the surface roughness of the parts fabricated with and without the controller was compared in Figure 4-14. It is obvious that the quality of the top surface was better when the control system came into action. While the average Sa of the part manufactured by laser power of 150 W was 10.48 μm, that of the controlled part was 5.91 μm, indicating that the controller has remarkably improved the surface roughness.

The roughness measurements perpendicular to the scanning direction were also compared in Figure 4-15, representing the lower range of roughness in part fabricated by the control system. The average Ra of the controlled and uncontrolled parts from 6 measurements were 4.95 and 9.62 μm, respectively.

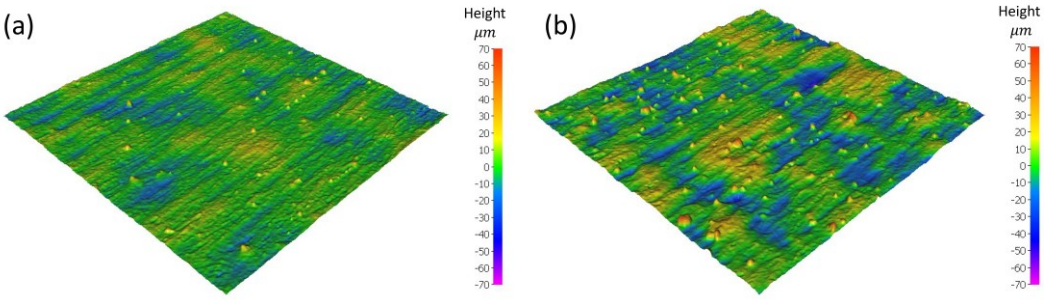

Figure 4-14 Color-3D images showing the top surface topography of parts produced by L-PBF processing of: (a) the part fabricated by control process at the scanning speed of 500 mm/s, and (b) Part 10 with the laser power of 150 W and the scanning speed of 500 mm/s.

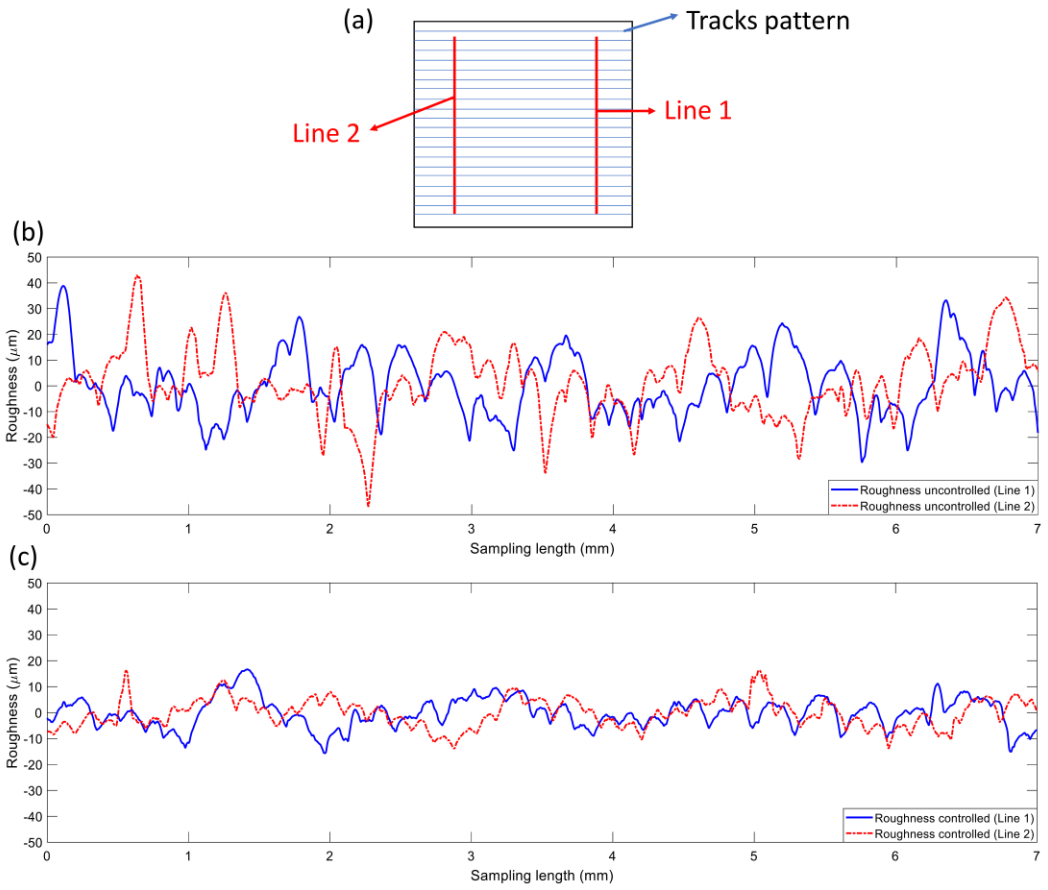

Figure 4-15 (a) the lines of roughness measurements, (b) roughness measurements perpendicular to the scanning track for the uncontrolled part fabricated at 500 mm/s, and (c) roughness measurements perpendicular to the scanning track for the controlled part manufactured at 500 mm/s.

4.5.2 Controller performance at the scanning speed of 400 mm/s

The second set of experiments was carried out at the scanning speed of 400 mm/s to examine the performance of the controller at different scanning speeds. A sample with the fixed laser power of 140 W (uncontrolled condition) was also fabricated and compared with the controlled sample at the scanning speed of 400 mm/s. Since the scanning speeds of the first and second scenarios were close to each other, it was expected that the part with

the fixed process parameter has a relative density over 99%. The initial laser power of the controlled scenario was also 140 W. Referring to the results of the control system shown in Figure 4-16, the melt pool width quickly reached close to the desired value, confirming the discussion provided in section 4.5.1. The surface quality of the controlled and uncontrolled cases were compared in Figure 4-17. The average Sa values for the controlled and the uncontrolled samples were 6.64 and 9.61 μm, respectively. Also, Figure 4-18 shows the roughness measurements. The average Ra of the controlled part was 5.93 μm while this value was 9.02 μm for the uncontrolled part. Therefore, it can be inferred that the proposed FF plus FB controller was effective for various scanning speeds and was capable of enhancing the surface quality at different initial conditions.

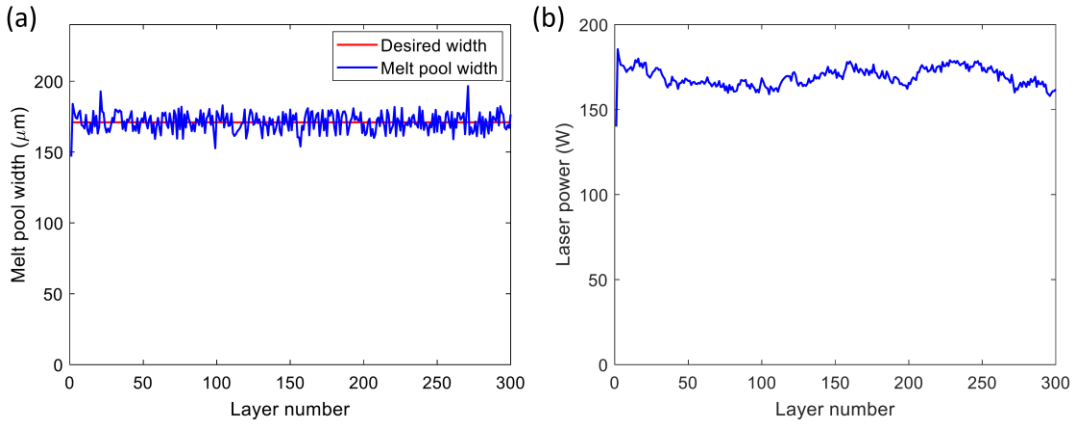

Figure 4-16 (a) The melt pool width during the control process at 400 mm/s, (b) the laser power during the control process at 400 mm/s.

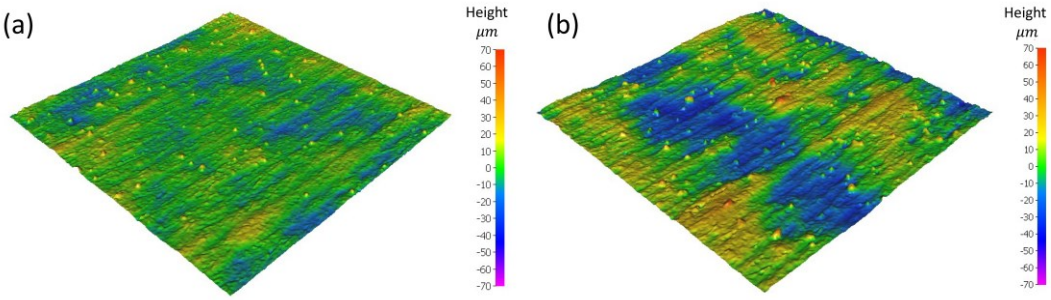

Figure 4-17 Color-3D images showing the top surface topography of parts produced by L-PBF processing of: (a) the part fabricated by control process at the scanning speed of 400 mm/s, and (b) the sample with the laser power of 140 W and the scanning speed of 400 mm/s.

4.5.3 Bridge geometry

The third set of experiments was designed to fabricate a benchmark geometry (bridge) to evaluate the performance of the controller when printing an unsupported surface. Figure 4-19 shows the geometry of the bridge used in this study to simulate the printing of such a surface. The bridge had a total height of 132 layers, with a deck starting from layer 67. Sections (I) and (II) were evaluated separately because of the absence of support structure in the latter. Each section had an area of $10\,mm \times 10\,mm$. The experiment was implemented at the scanning speed of 500 mm/s. A sample with a fixed laser power of 150 W was also fabricated for the sake of comparison.

When the laser printed the first layers of section (II), the melt pool size increased drastically due to the lower heat dissipation from the underlying powder bed. This consequently increased the average melt pool width of the whole layer (including sections (I) and (II)), which will be used as a feedback signal for adjusting the laser power of the next layer. Figure 4-20(a) and (b) demonstrate that the melt pool width in sections (I) and (II) at layer 67 with the laser power of 150 W is 147 and 233 μm, respectively.

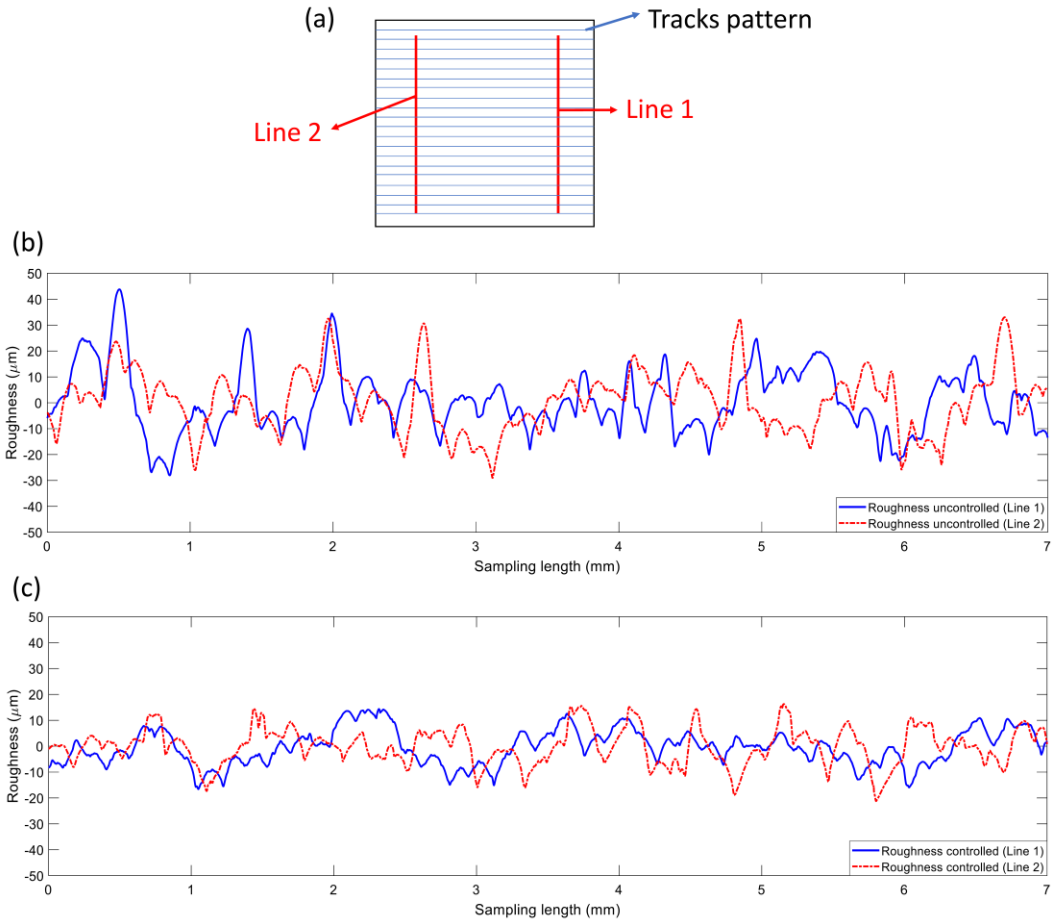

Figure 4-18 (a) the lines of roughness measurements, (b) roughness measurements perpendicular to the scanning track for the uncontrolled part fabricated at 400 mm/s, and (c) roughness measurements perpendicular to the scanning track for the controlled part manufactured at 400 mm/s.

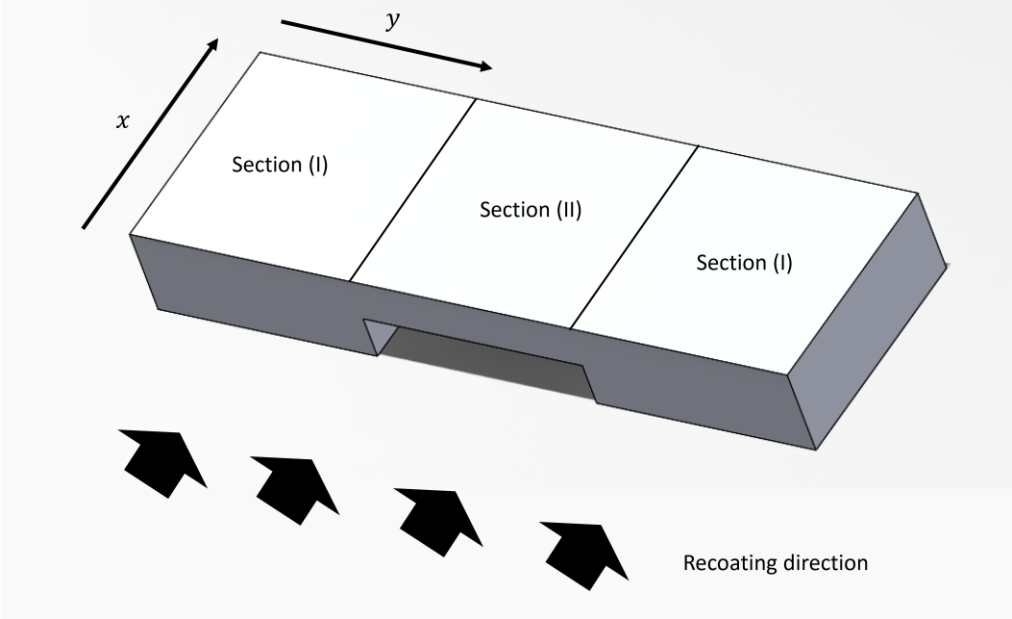

Figure 4-19 The bridge geometry and the recoating direction.

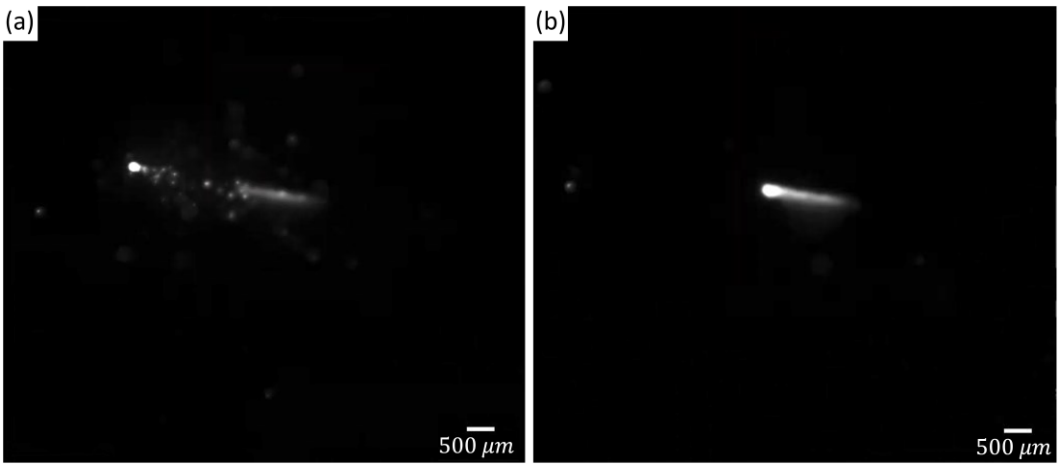

Figure 4-20 (a) The melt pool in section (I) at layer 67 and (b) the melt pool in section (II) at layer 67.

The melt pool enlargement in section (II) of the bridge can cause different types of defects such as warpage and distortion. Such defects provide an unfavorable condition for the part in the uncontrolled case. First, the severe warpage results in an uneven powder deposition. Second, the warpage can act as an obstacle to the recoater movement and cause damage to

it, which affects the powder spreading for the rest of the process. Figure 4-21(a) and (b) show the damage due to the warpage in the uncontrolled case along the x and y directions, respectively. Both these damages deteriorate the surface quality of the final part. Therefore, the presence of corrective action is vital in such situations to minimize the surface roughness.

Figure 4-22 shows the results of the control system for the same geometry in the controlled condition. At layer 67, the melt pool width increased, and the control system reduced the laser power to decrease the average melt pool width of the next layer. After a few layers, the base of the deck reached the situation close to the normal printing condition, and the melt pool width dropped at layer 74. Finally, the building condition completely returned to its desired situation from layer 82 by increasing the laser power.

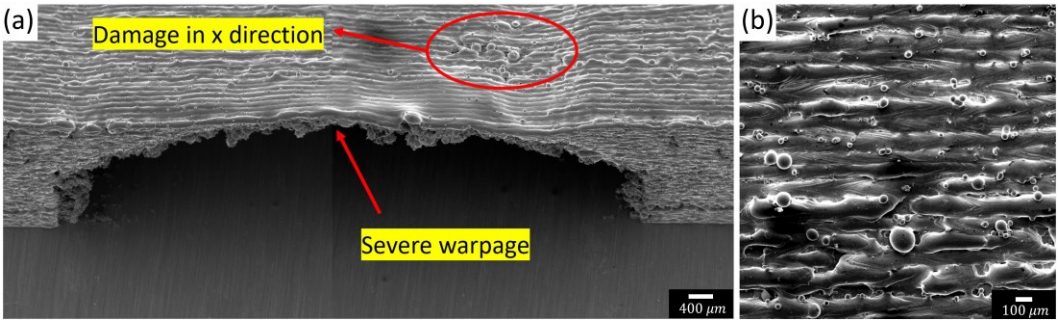

Figure 4-21 (a) Part with fixed process parameters (consisting of two pictures from the left and right sides of the part connected to each other), the severe warpage resulted in defects along x direction, and (b) the effect of poor powder deposition due to the warpage.

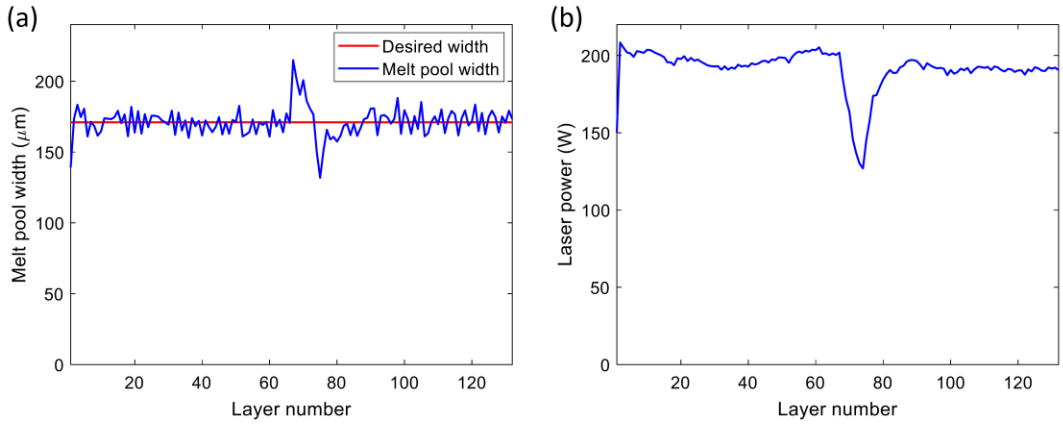

Figure 4-22 (a) The melt pool width during the control process of the bridge geometry, (b) the laser power during the control process of the bridge geometry.

By comparing Figure 4-21(a) and Figure 4-23, it can be inferred that the implementation of the control system could effectively mitigate the warpage at the deck of the bridge. As a result, the control system has resolved the issues caused by the uneven powder deposition in both x and y directions, leading to the enhanced quality of the top surface. The quality of the controlled and uncontrolled parts at sections (I) and (II) were compared in Figure 4-24. In section (I), the average Sa for the uncontrolled sample was 11.58 μm which was higher than that of Part 10 (simple cubic geometry) mentioned in section 4.3. The average Sa in section (I) for the controlled sample was 6.96 μm which shows that although it is not as high quality as the controlled part showed in 4.5.1, the control system enhanced the part quality and prevented the sample from failure.

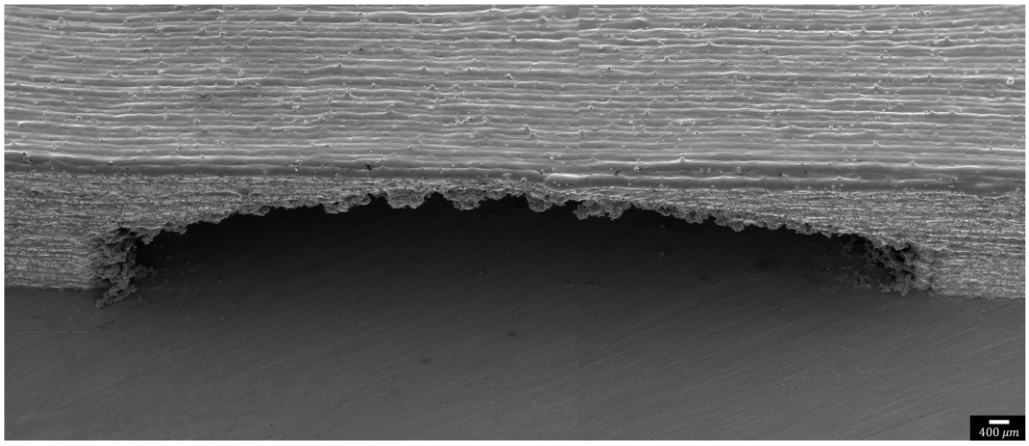

Figure 4-23 The controlled bridge sample (consisting of two pictures from the left and right sides of the part connected to each other). The issues in the uncontrolled sample were resolved.

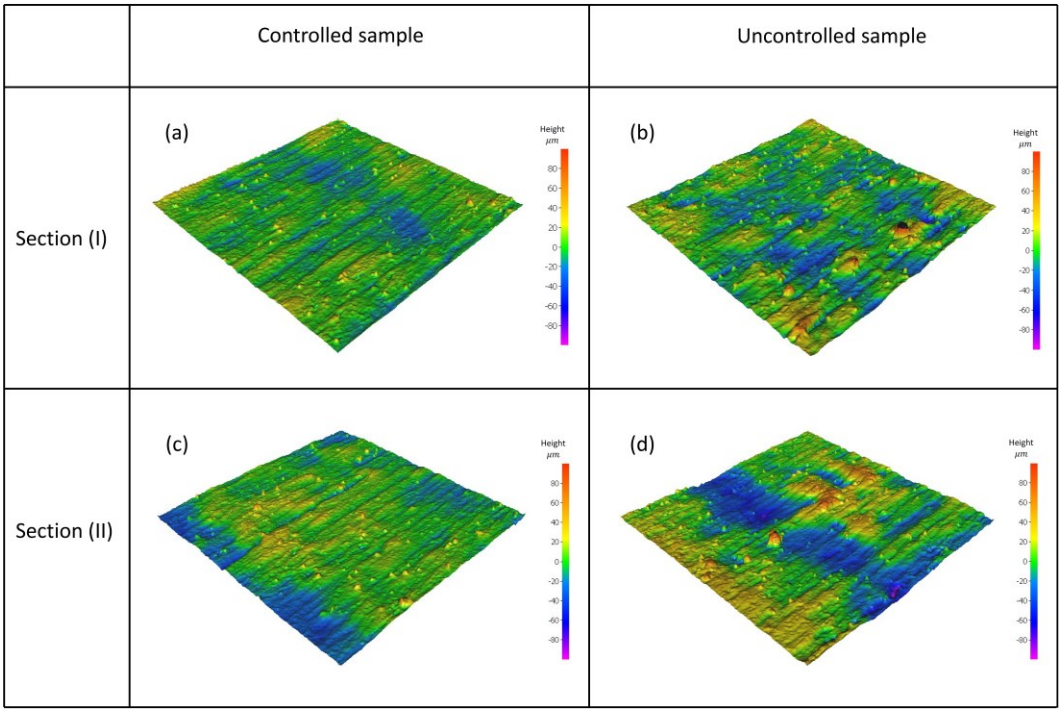

Figure 4-24 The comparison of surface quality between the controlled sample and uncontrolled sample: (a) the surface quality of section (I) fabricated with the control system, (b) the surface quality of section (I) manufactured with fixed process parameters, (c) the surface quality of section (II) for the controlled sample, and (d) the surface quality of section (II) for the uncontrolled sample.

Regarding section (II), the average Sa for the uncontrolled sample was 15.25 μm while it was 7.63 μm for the controlled part, confirming that the control system improved the surface quality. The higher Sa in section (II) of the controlled part compared to the Sa in section (I) can be explained by the absence of support under the deck of the bridge. Moreover, the average Ra in section (I) for the uncontrolled and controlled samples were 10.81 and 6.77 μm, respectively, while the average Ra in section (II) for the uncontrolled and controlled samples were 13.60 and 7.11 μm, respectively. Both measurements confirm that the controller improved the surface quality of the bridge.

Figure 4-25 shows the primary profile of the parts fabricated under controlled and uncontrolled conditions across the three different scanning tracks (y direction). The scanning tracks were located at the right, middle, and left of the parts. According to Figure 4-25(a)-(c), there were two main concave sections indicating a geometry inaccuracy perpendicular to the scanning tracks. The distance between these two sinking sections was 9.39 mm which is almost equal to the length of the deck. In other words, the sinking sections were located close to the edges of the deck. It occurred mainly because of the absence of support structure and the inadequate deposition of powder in these regions during the powder spreading stage. The negative height area in Figure 4-24(c) also can be explained by the absence of support at section (II). However, the inaccuracy at the edges of the deck drastically decreased in the controlled part (Figure 4-25(d)-(f)).

In general, the results showed that controlling the melt pool width using the FF plus FB control approach is a cost-effective real-time approach that can minimize the surface roughness and mitigate the formation of internal defects during the process. Besides, this

technique enhances the quality of the part regardless of the initially employed process parameters.

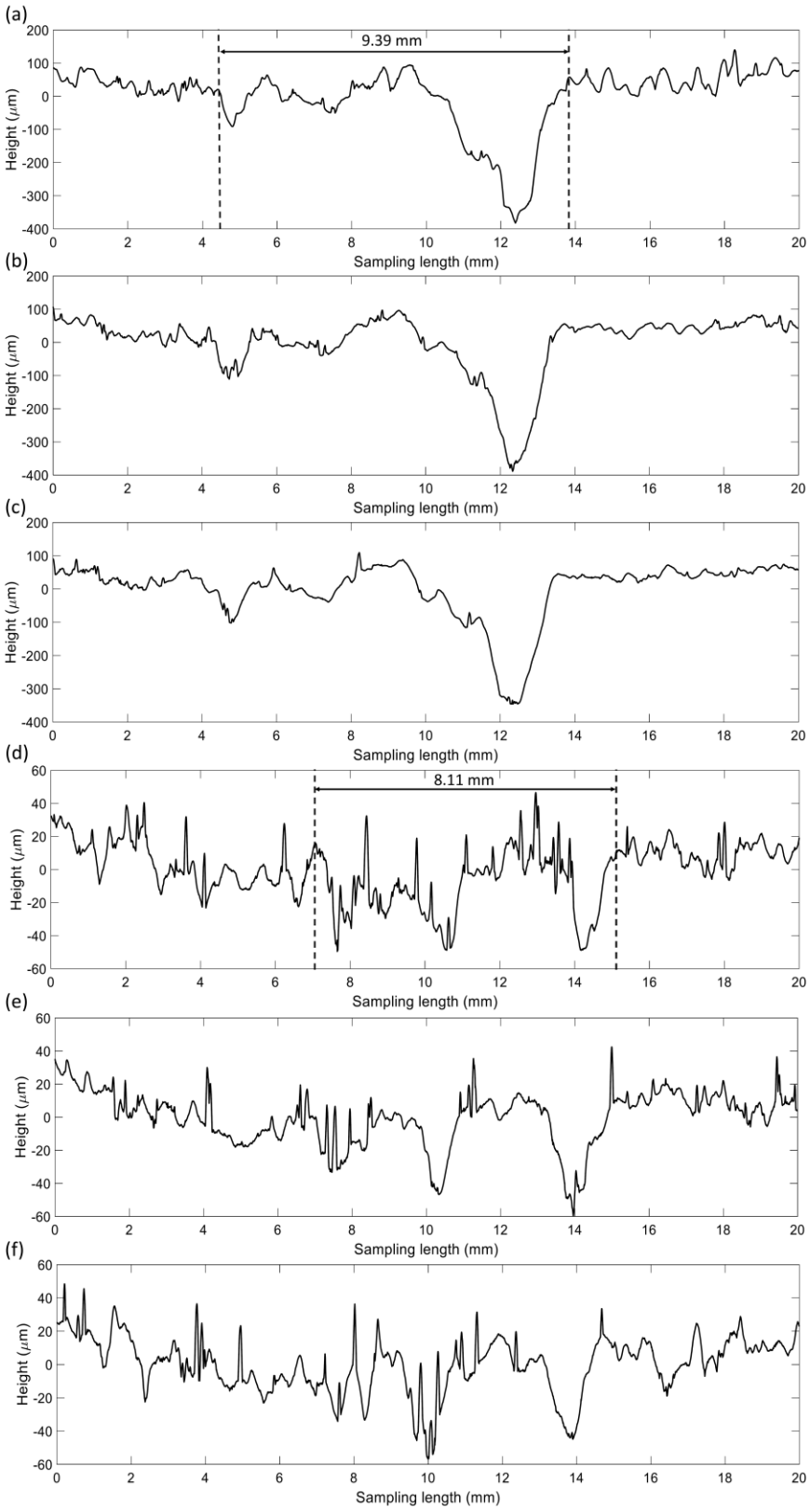
(a)
9.39 mm
Height (μm)
Sampling length (mm)
(b)
Height (μm)
Sampling length (mm)
(c)
Height (μm)
Sampling length (mm)
(d)
8.11 mm
Height (μm)
Sampling length (mm)
(e)
Height (μm)
Sampling length (mm)
(f)
Height (μm)
Sampling length (mm)

Figure 4-25 Primary profile of a line in y direction located at: (a) the right side of the uncontrolled part, (b) the middle of the uncontrolled part, (c) the left side of the uncontrolled part, (d) the right side of the controlled part, (e) the middle of the controlled part, (f) the left side of the uncontrolled part.

4.6 Conclusions

In this study, a monitoring system consisting of a high-speed camera, zooming lens, short pass filter, and image processing approach was developed to measure the dimensions of the melt pool and the level of spatters during the process. In addition, the effect of some defects originating from balling phenomenon and lack of inter-track overlap was investigated on the top surface quality of the fabricated parts. The modified two-innovation stochastic gradient descent approach was utilized to model the width of the melt pool based on the absorbed energy. Also, an FF plus FB control system was developed to keep the melt pool width close to the desired value to eliminate two of the top surface roughness sources, namely; balling and lack of inter-track overlap, and to ensure smooth and flat overlapping curvature between adjacent laser scan tracks, while avoiding the high level of spatters. Some simulations were implemented to evaluate the control system performance before the main experiment. Thereafter, the performance of the controller was evaluated in three different scenarios. Regardless of the initial condition, scanning speed, and geometry of the part, when the control system was deployed, the surface roughness was minimized since not only the desired melt pool width was obtained but also a negligible amount of spatters was perceptible on the top surface. In summary, the following conclusions can be drawn from this study:

1. By increasing the laser power at a constant scanning speed and hatch spacing, first, the balling phenomenon and then the lack of inter-track overlap can be eliminated.

This is because as the laser power increases, the narrow and discontinuous laser scan tracks turn into continuous and wide tracks with reasonable inter-track overlap. Therefore, controlling the melt pool width not only solves the lack of overlap issue but also can eliminate the balling phenomenon, both helping to improve the top surface quality.

2. The surface roughness is improved by increasing the laser power until the high level of spatters adversely affects the surface roughness. Therefore, in the control approach, it is required to avoid too much increase in the laser power with the purpose of enhancing the inter-track overlap since, at such conditions, the excessive level of spatters offset the improvements achieved by the former and even make the surface quality worse.
3. The desired melt pool width for the hatch spacing of 100 μm and layer thickness of 30 μm was determined to be 171 μm based on two criteria of reasonable inter-track overlap and a negligible level of spatters.
4. The FF plus FB control system utilized in this study is applicable for different initial conditions and at different scanning speeds.
5. The controller proposed in this study can even mitigate unexpected issues during the process, such as warpage of the unsupported sections of a bridge geometry via manipulation of the laser power. This results in improvement of surface quality and prevention from process failure, which is of utmost importance for complex geometries.

Authors contributions:

Hossein Rezaeifar: Investigation, Methodology, Conceptualization, Writing-original draft.

Mohamed Elbestawi: Review and editing, Supervision.

4.7 References

[1] T. DebRoy, H.L. Wei, J.S. Zuback, T. Mukherjee, J.W. Elmer, J.O. Milewski, A.M. Beese, A. Wilson-Heid, A. De, W. Zhang, Additive manufacturing of metallic components – Process, structure and properties, Prog. Mater. Sci. 92 (2018) 112–224. https://doi.org/10.1016/j.pmatsci.2017.10.001.

[2] N. Nadammal, T. Mishurova, T. Fritsch, I. Serrano-Munoz, A. Kromm, C. Haberland, P.D. Portella, G. Bruno, Critical role of scan strategies on the development of microstructure, texture, and residual stresses during laser powder bed fusion additive manufacturing, Addit. Manuf. 38 (2021) 101792. https://doi.org/10.1016/J.ADDMA.2020.101792.

[3] M.H. Ghoncheh, M. Sanjari, A.S. Zoeram, E. Cyr, B.S. Amirkhiz, A. Lloyd, M. Haghshenas, M. Mohammadi, On the microstructure and solidification behavior of new generation additively manufactured Al-Cu-Mg-Ag-Ti-B alloys, Addit. Manuf. 37 (2021) 101724. https://doi.org/10.1016/J.ADDMA.2020.101724.

[4] E. Fereiduni, A. Ghasemi, M. Elbestawi, Selective laser melting of aluminum and titanium matrix composites: Recent progress and potential applications in the aerospace industry, Aerospace. 7 (2020). https://doi.org/10.3390/AEROSPACE7060077.

[5] W.E. King, A.T. Anderson, R.M. Ferencz, N.E. Hodge, C. Kamath, S.A. Khairallah, A.M. Rubenchik, Laser powder bed fusion additive manufacturing of metals; physics, computational, and materials challenges, Appl. Phys. Rev. 2 (2015) 041304. https://doi.org/10.1063/1.4937809.

[6] S. Sanchez, P. Smith, Z. Xu, G. Gaspard, C.J. Hyde, W.W. Wits, I.A. Ashcroft, H. Chen, A.T. Clare, Powder Bed Fusion of nickel-based superalloys: A review, Int. J. Mach. Tools Manuf. 165 (2021) 103729. https://doi.org/10.1016/J.IJMACHTOOLS.2021.103729.

[7] M. Narvan, K.S. Al-Rubaie, M. Elbestawi, Process-structure-property relationships of AISI H13 tool steel processed with selective laser melting, Materials (Basel). 12 (2019) 2284.

[8] F. Froes, R. Boyer, Additive manufacturing for the aerospace industry, 2019. https://books.google.com/books?hl=en&lr=&id=IlSIDwAAQBAJ&oi=fnd&pg=PP1&dq=Additive+manufacturing+for+the+aerospace+industry&ots=BBCf9CDqXn&sig=0t8xb-yvqN1Z1NHWXcRyfNCsLxU (accessed October 14, 2021).

[9] A. Uriondo, M. Esperon-Miguez, S. Perinpanayagam, The present and future of additive manufacturing in the aerospace sector: A review of important aspects:, Http://Dx.Doi.Org/10.1177/0954410014568797. 229 (2015) 2132–2147. https://doi.org/10.1177/0954410014568797.

[10] L. Dowling, J. Kennedy, S. O'Shaughnessy, D. Trimble, A review of critical repeatability and reproducibility issues in powder bed fusion, Mater. Des. 186 (2020) 108346. https://doi.org/10.1016/J.MATDES.2019.108346.

[11] I. Echeta, X. Feng, B. Dutton, R. Leach, S. Piano, Review of defects in lattice structures manufactured by powder bed fusion, Int. J. Adv. Manuf. Technol. 2019 1065. 106 (2019) 2649–2668. https://doi.org/10.1007/S00170-019-04753-4.

[12] M.A. Balbaa, A. Ghasemi, E. Fereiduni, M.A. Elbestawi, S.D. Jadhav, J.-P. Kruth,

Role of powder particle size on laser powder bed fusion processability of AlSi10mg alloy, Addit. Manuf. 37 (2021) 101630.

[13] M. Khorasani, A. Ghasemi, U.S. Awan, E. Hadavi, M. Leary, M. Brandt, G. Littlefair, W. O'Neil, I. Gibson, A study on surface morphology and tension in laser powder bed fusion of Ti-6Al-4V, Int. J. Adv. Manuf. Technol. 2020 1119. 111 (2020) 2891–2909. https://doi.org/10.1007/S00170-020-06221-W.

[14] J. Snyder, K.T.-J. of Manufacturing, undefined 2020, Understanding laser powder bed fusion surface roughness, J. Manuf. Sci. Eng. 142 (2020) 071003. https://asmedigitalcollection.asme.org/manufacturingscience/article-abstract/142/7/071003/1074958?casa_token=uW8Zv5PtNy4AAAAA:gW4LJ5YFU671VJryAnm2RAFbuSumFjHwIyKzkGBOTY-FbkuaydXAJk7Fi9w5bsUXlr8WSw (accessed October 27, 2021).

[15] R. Esmaeilizadeh, U. Ali, A. Keshavarzkermani, Y. Mahmoodkhani, E. Marzbanrad, E. Toyserkani, On the effect of spatter particles distribution on the quality of Hastelloy X parts made by laser powder-bed fusion additive manufacturing, J. Manuf. Process. 37 (2019) 11–20. https://doi.org/10.1016/J.JMAPRO.2018.11.012.

[16] D. Tanigawa, N. Abe, M. Tsukamoto, Y. Hayashi, H. Yamazaki, Y. Tatsumi, M. Yoneyama, Effect of laser path overlap on surface roughness and hardness of layer in laser cladding, Sci. Technol. Weld. Join. 20 (2015) 601–606.

[17] M. Grasso, B.M. Colosimo, Process defects and in situ monitoring methods in metal powder bed fusion: a review, Meas. Sci. Technol. 28 (2017) 044005. https://doi.org/10.1088/1361-6501/AA5C4F.

[18] D. Bourell, J.P. Kruth, M. Leu, G. Levy, D. Rosen, A.M. Beese, A. Clare, Materials for additive manufacturing, CIRP Ann. 66 (2017) 659–681. https://doi.org/10.1016/J.CIRP.2017.05.009.

[19] L. Li, J.Q. Li, T.H. Fan, Phase-field modeling of wetting and balling dynamics in powder bed fusion process, Phys. Fluids. 33 (2021) 042116. https://doi.org/10.1063/5.0046771.

[20] A. Sola, A. Nouri, Microstructural porosity in additive manufacturing: The formation and detection of pores in metal parts fabricated by powder bed fusion, J. Adv. Manuf. Process. 1 (2019). https://doi.org/10.1002/AMP2.10021.

[21] R. Snell, S. Tammas-Williams, L. Chechik, A. Lyle, E. Hernández-Nava, C. Boig, G. Panoutsos, I. Todd, Methods for Rapid Pore Classification in Metal Additive Manufacturing, Jom. 72 (2020) 101–109. https://doi.org/10.1007/s11837-019-03761-9.

[22] M. Abdelrahman, E.W. Reutzel, A.R. Nassar, T.L. Starr, Flaw detection in powder bed fusion using optical imaging, Addit. Manuf. 15 (2017) 1–11. https://doi.org/10.1016/j.addma.2017.02.001.

[23] H. Rezaeifar, M. Elbestawi, Porosity formation mitigation in laser powder bed fusion process using a control approach, Opt. Laser Technol. 147 (2022) 107611. https://doi.org/10.1016/J.OPTLASTEC.2021.107611.

[24] R. Fabbro, M. Hamadou, F. Coste, Metallic vapor ejection effect on melt pool dynamics in deep penetration laser welding, J. Laser Appl. 16 (2004) 16–19.

[25] H. Nakamura, Y. Kawahito, K. Nishimoto, S. Katayama, Elucidation of melt flows

and spatter formation mechanisms during high power laser welding of pure titanium, J. Laser Appl. 27 (2015) 32012.

[26] A. Matsunawa, J.-D. Kim, N. Seto, M. Mizutani, S. Katayama, Dynamics of keyhole and molten pool in laser welding, J. Laser Appl. 10 (1998) 247–254.

[27] R. Fabbro, S. Slimani, I. Doudet, F. Coste, F. Briand, Experimental study of the dynamical coupling between the induced vapour plume and the melt pool for Nd–Yag CW laser welding, J. Phys. D. Appl. Phys. 39 (2006) 394.

[28] H. Zheng, H. Li, L. Lang, S. Gong, Y. Ge, Effects of scan speed on vapor plume behavior and spatter generation in laser powder bed fusion additive manufacturing, J. Manuf. Process. 36 (2018) 60–67. https://doi.org/10.1016/J.JMAPRO.2018.09.011.

[29] X. Zhang, B. Cheng, C. Tuffile, Simulation study of the spatter removal process and optimization design of gas flow system in laser powder bed fusion, Addit. Manuf. 32 (2020) 101049. https://doi.org/10.1016/J.ADDMA.2020.101049.

[30] L.E. Criales, Y.M. Arısoy, B. Lane, S. Moylan, A. Donmez, T. Özel, Laser powder bed fusion of nickel alloy 625: Experimental investigations of effects of process parameters on melt pool size and shape with spatter analysis, Int. J. Mach. Tools Manuf. 121 (2017) 22–36. https://doi.org/10.1016/J.IJMACHTOOLS.2017.03.004.

[31] H. Hassanin, A. Elshaer, R. Benhadj-Djilali, F. Modica, I. Fassi, Surface Finish Improvement of Additive Manufactured Metal Parts, (2018) 145–164. https://doi.org/10.1007/978-3-319-68801-5_7.

[32] R. Yavari, A. Riensche, E. Tekerek, L. Jacquemetton, H. Halliday, M. Vandever, A. Tenequer, V. Perumal, A. Kontsos, Z. Smoqi, K. Cole, P. Rao, Digitally twinned additive manufacturing: Detecting flaws in laser powder bed fusion by combining thermal simulations with in-situ meltpool sensor data, Mater. Des. 211 (2021) 110167. https://doi.org/10.1016/J.MATDES.2021.110167.

[33] V. Gunenthiram, P. Peyre, M. Schneider, M. Dal, F. Coste, I. Koutiri, R. Fabbro, Experimental analysis of spatter generation and melt-pool behavior during the powder bed laser beam melting process, J. Mater. Process. Technol. 251 (2018) 376–386. https://doi.org/10.1016/J.JMATPROTEC.2017.08.012.

[34] E. Yasa, J.P. Kruth, J. Deckers, Manufacturing by combining Selective Laser Melting and Selective Laser Erosion/laser re-melting, CIRP Ann. - Manuf. Technol. 60 (2011) 263–266. https://doi.org/10.1016/j.cirp.2011.03.063.

[35] J. Zhou, X. Han, H. Li, S. Liu, J. Yi, Materials & Design Investigation of layer-by-layer laser remelting to improve surface quality , microstructure , and mechanical properties of laser powder bed fused AlSi10Mg alloy, Mater. Des. 210 (2021) 110092. https://doi.org/10.1016/j.matdes.2021.110092.

[36] P. Stief, J. Dantan, A. Etienne, A. Siadat, ScienceDirect ScienceDirect Improving the quality of up-facing inclined surfaces in laser powder bed Improving the quality of inclined surfaces in laser powder bed fusion of metals using a dual laser setup fusion of metals using a a dual laser setup new m, Procedia CIRP. 94 (2020) 266–269. https://doi.org/10.1016/j.procir.2020.09.050.

[37] A.G. Demir, B. Previtali, Investigation of remelting and preheating in SLM of 18Ni300 maraging steel as corrective and preventive measures for porosity

reduction, Int. J. Adv. Manuf. Technol. 93 (2017) 2697–2709. https://doi.org/10.1007/s00170-017-0697-z.

[38] E.G. Brodie, J. Richter, T. Wegener, T. Niendorf, A. Molotnikov, Low-cycle fatigue performance of remelted laser powder bed fusion (L-PBF) biomedical Ti25Ta, Mater. Sci. Eng. A. 798 (2020) 140228. https://doi.org/10.1016/j.msea.2020.140228.

[39] Z. Xi, Model Predictive Control of Melt Pool Size for the Laser Powder Bed Fusion Process Under Process Uncertainty, ASCE-ASME J Risk Uncert Engrg Sys Part B Mech Engrg. 8 (2022). https://doi.org/10.1115/1.4051746.

[40] S.Z. Hussain, Z. Kausar, Z.U. Koreshi, S.R. Sheikh, H.Z.U. Rehman, H. Yaqoob, M.F. Shah, A. Abdullah, F. Sher, Feedback control of melt pool area in selective laser melting additive manufacturing process, Processes. 9 (2021). https://doi.org/10.3390/pr9091547.

[41] E. Vasileska, A.G. Demir, B.M. Colosimo, B. Previtali, Layer-wise control of selective laser melting by means of inline melt pool area measurements, J. Laser Appl. 32 (2020) 022057. https://doi.org/10.2351/7.0000108.

[42] H. Rezaeifar, M.A. Elbestawi, On-line melt pool temperature control in L-PBF additive manufacturing, Int. J. Adv. Manuf. Technol. 112 (2021) 2789–2804. https://doi.org/10.1007/s00170-020-06441-0.

[43] BROWN DC, Close- range camera calibration, Photogramm Eng. 37 (1971) 855–866.

[44] Xiuqin-Li, Xianyang-Du, Yawei-Li, The Technology Research of Camera

Calibration Based On LabVIEW, Int. J. Res. Eng. Sci. ISSN. 3 (2015) 8–17. www.ijres.org (accessed November 11, 2021).

[45] C. Relf, Image acquisition and processing with LabVIEW, 2003. https://books.google.com/books?hl=en&lr=&id=w38eAPw8FBcC&oi=fnd&pg=PP1&dq=image+acquisition+and+processing+&ots=vxJWQfWUSk&sig=LPzaDfxJthKU3xQuzxq5BmfiIps (accessed November 11, 2021).

[46] M. Jankowski, Erosion, dilation and related operators, Dep. Electr. Eng. South. Maine Portland, Maine, USA. (2006).

[47] A. Fathi, A. Khajepour, E. Toyserkani, M. Durali, Clad height control in laser solid freeform fabrication using a feedforward PID controller, Int. J. Adv. Manuf. Technol. 35 (2007) 280–292.

[48] J. Xiong, Z. Yin, W. Zhang, Closed-loop control of variable layer width for thin-walled parts in wire and arc additive manufacturing, J. Mater. Process. Technol. 233 (2016) 100–106.

[49] T. Craeghs, F. Bechmann, S. Berumen, J.P. Kruth, Feedback control of Layerwise Laser Melting using optical sensors, in: Phys. Procedia, 2010. https://doi.org/10.1016/j.phpro.2010.08.078.

[50] J. Metelkova, Y. Kinds, K. Kempen, C. de Formanoir, A. Witvrouw, B. Van Hooreweder, On the influence of laser defocusing in Selective Laser Melting of 316L, Addit. Manuf. 23 (2018) 161–169. https://doi.org/10.1016/j.addma.2018.08.006.

[51] J.K. Chaurasia, A.N. Jinoop, P. P, C.P. Paul, K.S. Bindra, S. Bontha, Study of melt

pool geometry and solidification microstructure during laser surface melting of Inconel 625 alloy, Optik (Stuttg). 246 (2021) 167766. https://doi.org/10.1016/j.ijleo.2021.167766.

[52] C. Sainte-Catherine, M. Jeandin, D. Kechemair, J.-P. Ricaud, L. Sabatier, Study of Dynamic Absorptivity at 10.6 μm (CO2) and 1.06 μm (Nd-YAG) Wavelengths as a Function of Temperature, Le J. Phys. IV. 1 (1991) C7-151.

[53] Q. Tu, Y. Rong, J. Chen, Parameter identification of ARX models based on modified momentum gradient descent algorithm, Complexity. 2020 (2020).

[54] J.L. Guzmán, T. Hägglund, A. Visioli, Feedforward compensation for PID control loops, in: PID Control Third Millenn., Springer, 2012: pp. 207–234.

[55] D. Jin, S. Lin, Advances in electronic commerce, web application and communication, Springer, 2012.

[56] T.E. Marlin, Process Control, Designing Processes and Control Systems for Dynamic Performance, (n.d.).

Chapter 5

Summary and Conclusions

5.1 Summary and conclusive remarks

Inconel 625 is a nickel-chromium-based superalloy with a hardening mechanism of niobium and molybdenum. With a melting point of about 1300 ℃, it is considered a high-temperature strength material. It is also well-known for corrosion and fatigue resistance. These mechanical properties make this material highly favorable in aerospace, marine, and nuclear industries. However, they are considered hard-to-cut alloys in conventional manufacturing. Therefore, additive manufacturing can play an important role in producing Inconel 625 parts. As mentioned, Inconel 625 has a huge role in sensitive industries, so the quality of the part manufactured for such industries is required to be guaranteed.

The L-PBF processing of Inconel 625 parts has been studied in the past decade. Most of the studies concentrated on the printability of the material and the properties of the part fabricated by the L-PBF process. However, as mentioned, the quality of the part needs to be monitored and controlled to have parts with uniform features (i.e., make the process

more repeatable). This thesis focuses on monitoring and control for the L-PBF additive manufacturing of Inconel 625 to improve different quality aspects of the final product.

The microstructure properties of the final part, specifically the primary dendrite arm spacing of the Inconel parts fabricated by the L-PBF process was investigated. A two-color pyrometer, which was calibrated previously, was utilized to measure the melt pool temperature during the process. The melt pool temperature was controlled layer-wise using three different controllers, namely, simple P controller, model-based adaptive P, and quasi sliding mode controllers. The results revealed that the thermal dynamics of the melt pool, specifically the temperature, has a great impact on the microstructural and mechanical properties uniformity of the final products. The fast response of the controller and the knowledge about the initial temperature can be helpful for making the microstructure of the part more uniform along the building direction, leading to more uniform mechanical properties. Also, higher melt pool temperatures result in higher larger primary dendrite arm spacing, leading to higher microhardness in Inconel 625 parts.

Moreover, different types of porosity which can deteriorate the quality of the part during the process were investigated in this thesis. The applicability of the energy density in predicting the densification level and defect type of the L-PBF fabricated parts was called into question. It was shown that parts with the same energy density can have different qualities and even have different types of porosities. Therefore, energy density cannot be used generally to predict the level and type of porosity. Three types of porosities (lack of fusion, lack of penetration, and keyhole) were investigated. A monitoring system consisting of a thermal camera and an IR-transmissive window was utilized to find the correlation between each type of porosity and thermal measurements and find a safe zone for mitigating the porosity formation. Based on the results, the PID controller used to keep

the temperature inside the safe zone performed well for different initial conditions and at different scanning speeds, leading to improving the quality of the final part significantly.

Finally, the surface roughness of the part fabricated by the L-PBF process as another element of the quality was targeted in this study. Different factors that can affect the top surface quality, such as balling, lack of inter-track overlap, spatters, and overlapping curvature, were investigated using a monitoring system consisting of a high-speed camera, zooming lens, short pass filter, and image processing approach. The modified two-innovation stochastic gradient descent approach was utilized to model the width of the melt pool based on the absorbed energy, and a feedforward plus feedback control system was developed accordingly to keep the melt pool width close to the desired value and keep the level of spatters lower than the critical value. Simulation results showed that the controller was applicable even with the presence of modeling error. Experimental results indicated that by increasing the laser power at a constant scanning speed and hatch spacing, first, the balling phenomenon and then the lack of inter-track overlap can be eliminated. Therefore, controlling the melt pool width eliminates two sources of top surface roughness simultaneously. The desired melt pool width for the hatch spacing of 100 μm and layer thickness of 30 μm was determined to be 171 μm based on two criteria of reasonable inter-track overlap and a negligible level of spatters. It was shown that regardless of the initial condition, scanning speed, and geometry of the part, when the FF plus FB control system was deployed, the surface roughness was minimized since not only the desired melt pool width was obtained but also a negligible amount of spatters was perceptible on the top surface. The controller proposed in this thesis can even mitigate unexpected issues during the process, such as warpage of the unsupported sections of a bridge geometry via manipulation of the laser power.

5.2 Strength, limitations, and future work

The effect of control systems on the quality of the parts during the L-PBF processing of Inconel 625 investigated in the current thesis helps to guarantee the reliable and repeatable fabrication of the final products that can be used in sensitive industries, which in turn, make the production line of parts feasible. The control of temperature not only proves to be a cost-effective and general solution for producing parts with optimum densification level (as opposed to the energy density method) but also makes the microstructure and consequently the mechanical properties of parts more uniform along the building direction. The width control system used in this thesis not only reduces the cost and time of the post-processing by minimizing the surface roughness but also prevents failure of the process because of some unexpected issues during the manufacturing of complex parts. Overall, the methods utilized in this thesis enhance productivity in highly sensitive industrial applications.

The main section of the work that can be improved in future studies is using sensors with higher sampling rates and resolution. It would help the effect of each controller on the quality of the parts more accurately. In other words, more precise and fast measurement provides more accurate feedback signals that can be used inside the control system.

In addition, as mentioned in chapter 2, it is possible to manipulate the microstructure by manipulating the temperature results in manufacturing the FGMs. However, the primary dendrite arm spacing was tried to be near uniform condition by controlling the melt pool temperature in this thesis, which would act as proof of concept. Therefore, the idea of the fabrication of FGMs using a control system requires further investigation. Additionally, the effect of controlling the melt pool temperature on other mechanical properties of the part manufactured by the L-PBF process can be investigated in the future.

The approach used for porosity mitigation improves the quality of the part in a few layers regardless of the initially employed process parameters. However, it should be emphasized that to correct the occurred porosity and the process parameters for the following layers simultaneously, the combination of this approach with suitable on-line corrective actions (such as remelting for a specific case) is worth further investigation.

Also, parts fabricated in porosity mitigation are simple cubic samples that would prove that the controller keeps the temperature inside the safe zone. Therefore, although it is expected that the approach presented in this study can also be applied to complex geometries, it should also be investigated in the future.

Furthermore, another approach for healing the porosity is the prediction of the porosity before occurrence using previous knowledge with machine learning approaches. In other words, machine learning can predict the quality of the part in some future layers, and the control approach can adjust the process parameters to avoid such predicted defects. The proposed approach also can be investigated in the future.

For minimization of the surface roughness, the level of spatters is considered as the metric for the level of damage with this phenomenon. However, the speed and direction of spatters also can be considered in the controller system to make the control approach more accurate.

Finally, the effect of control systems on other sources of quality degradation such as residual stress, cracks, and different sources of geometry inaccuracy is a topic that is worth investigating in the future.

5.3 Contribution

According to the literature, several factors change the quality of the final part during the L-PBF additive manufacturing process. Therefore, it is of utmost importance to maintain the part quality during the process. This thesis serves as an important step in dealing with

improving the quality of the part fabricated with the L-PBF process and making the process more reliable and repeatable. The main contributions of this study could be refined into the followings:

1) The findings of this study have contributed to making the microstructure of the parts during the L-PBF process near-uniform for the first time, which results in more uniform mechanical properties. Also, manipulation of the microstructure using the control of melt pool temperature was investigated.
2) Based on the correlation between the temperature of the melt pool and different types of porosity, this thesis determined a safe zone for the fabrication of the parts. Consequently, it replaced the energy density criterion, which can be used locally, with a general approach of controlling the temperature to reach the optimum final part.
3) The mechanism of surface roughness variations during the process was investigated. A control system was designed accordingly with considering the influence of the spatters for the first time. The results indicated that the control system designed in this thesis minimizes the top surface roughness, reducing the time and cost of post-processing of the final part.

Thus, this thesis paves the way for repeatability of the process and consequently mass production using AM technology.